A METHOD TO SIGNIFICANTLY IMPROVE FINITE ELEMENT STRESS PREDICTIONS

by

DANIEL JOSE PAYEN
M.Eng., University of Oxford, 2005

Submitted to the Department of Mechanical Engineering
in Partial Fulfilment of the Requirements for the Degree of

DOCTOR OF PHILOSOPHY IN MECHANICAL ENGINEERING

at the

MASSACHUSETTS INSTITUTE OF TECHNOLOGY

June 2012

Author .....
Daniel Jose Payen
Department of Mechanical Engineering
May 8, 2012

Certified by .....
Klaus-Jürgen Bathe
Professor of Mechanical Engineering
Thesis Supervisor

Accepted by .....
David Edgar Hardt
Professor of Mechanical Engineering
Chairman, Departmental Committee on Graduate Students

A METHOD TO SIGNIFICANTLY IMPROVE FINITE ELEMENT STRESS PREDICTIONS

by

Daniel Jose Payen

Submitted to the Department of Mechanical Engineering
on May 8, 2012 in Partial Fulfilment of the
Requirements for the Degree of Doctor of Philosophy in
Mechanical Engineering

Abstract

In this thesis, we present a novel method to improve the finite element stress predictions in static, dynamic and nonlinear analyses of solids. We focus on the use of low-order displacement-based finite elements, 3-node and 4-node elements in two-dimensional (2D) solutions, and 4-node and 8-node elements in 3D solutions -- because these elements can be computationally efficient, provided good stress predictions are obtained. We give a variational basis of the new method and compare the procedure, and its performance, with other effective previously proposed stress improvement techniques. We observe that the stresses of the new method converge quadratically in 1D and 2D solutions, i.e. with the same order as the displacements, and conclude that the new stress improvement method shows much promise for the analysis of solids, structures and multiphysics problems, to calculate improved stress predictions and to establish error measures.

Highlights

► Novel stress improvement method is given for static, dynamic and nonlinear analysis of solids. ► Focus is on the use of low-order elements. ► Quadratic convergence is observed for the improved stresses. ► Method is compared with existing techniques.

Thesis Supervisor: Klaus-Jürgen Bathe

Title: Professor of Mechanical Engineering

Acknowledgements

I would like to express sincere gratitude to my thesis supervisor, Professor Klaus-Jürgen Bathe, for his extraordinary guidance, support and kindness. Professor Bathe has been a true *Doktorvater*; not only is he a brilliant researcher and teacher, he is also a magnificent person and a constant source of inspiration.

I wish to thank my other thesis committee members, Professors Tomasz Wierzbicki and Nicolas Hadjiconstantinou, for their valuable suggestions, enthusiasm and insights on the work presented herein, and for their encouragement during my time at M.I.T.

I also thank my former University of Oxford tutors, Dr Stuart Turnbull and Dr Rimas Juškaitis, whom taught me much and equipped me with the essential tools needed to obtain a doctoral degree; my former colleagues at Renault Formula One Team, in particular Steve Diamond and Carlo Boldetti, for teaching me the practical aspects of finite element analysis in engineering design; the members of the Finite Element Research Group and Zafer Kazancı, of the Turkish Air Force Academy, for their help and friendly advice. In addition, I am thankful to the staff of ADINA R&D, Inc. for their support with the use of ADINA.

I wish to express unbounded thanks to my wife, Fatemeh Kadivar, and to my whole family (both the Payens and the Kadivars) for their support in all my work

endeavours, including the writing of this thesis, and for their kindness, affection and companionship. They have brought me great happiness, much laughter, and have made life beautiful.

Finally, I give *my most valuable thanks and heartfelt appreciation to my parents*, Alan and Josefina Payen, for their unconditional support throughout my studies. If not for their tireless efforts when I was younger, I would have very little today. I am forever grateful, and I proudly dedicate this thesis to them.

Contents

Introduction

In finite element analysis, a continuum is idealised as an assemblage of discrete elements. The analysis is then performed using displacement-based and mixed methods, see refs. [1], [2]. In each case, nodal displacements are solved for and the element stress is determined from the assumptions used in establishing the element stiffness matrices. In the displacement-based method, the derivatives of the displacements are used to establish the strains and hence the stresses, while in mixed methods additional strain or stress assumptions are employed (with additional equations) to establish the stresses. We refer to these calculated stresses as the "directly-calculated finite element stresses".

It is well known that the accuracy of the directly-calculated finite element stresses is poor, as compared with the accuracy of the calculated displacements, and the reasons are well understood. The stresses are obtained from the derivatives of the displacements; hence, they involve a lower degree of interpolation and converge at a lower rate. Furthermore, differential equilibrium is, in general, not satisfied at every point in the finite element model, which results in stress discontinuities at the element boundaries and non-equilibrium with the externally applied surface tractions [1]. The lack of accuracy can be seen using stress band plots of unsmoothed stresses [1], [3], [4].

During the last decades, many different stress improvement methods have been explored [3] to [37]. The aim is to reach enhanced stress predictions, as part of the solution of the mathematical models, and to establish solution error estimates [7], [8]. If an effective scheme to enhance the stress predictions was available, the finite element method could be used with coarser meshes, reducing the expense of analysis; and an effective scheme to assess the error would be valuable to assure an adequate solution. Early procedures were based either on stress smoothing [11], [12] or L_2 projection techniques [13]; however, these approaches are not particularly effective, and they have hardly been used in practice.

Considering inexpensive solution error indicators, the stress band plots proposed by Sussman and Bathe [1], [4], [14] have been used extensively, both for linear and nonlinear analyses, but of course these only give an indication of the solution accuracy -- they do not improve the stress predictions.

The calculation of improved stress predictions is particularly important if low-order elements are to be used. For example, considering three-dimensional (3D) solutions, the use of 4-node constant strain tetrahedral elements would frequently be computationally efficient if the stresses could be predicted to a higher accuracy than given directly by the displacements. That is, the constant stress assumption, implied by the assumed linear displacements, is not good in many analyses.

A widely-recognised contribution towards a stress improvement method was published by Zienkiewicz and Zhu, when they proposed the ‘superconvergent patch recovery’ method [15]. This technique is based on the existence of superconvergent points, also referred to as Barlow points [16], where the stresses are of one order higher accuracy than at any other point in the element domain. Appropriate order polynomials approximating the stresses are smoothly fitted

through these points, sometimes in a least squares sense. Later, variants of the original method were developed to further enhance its performance [17] to [21].

Although the superconvergent patch recovery methods seemed to work relatively well for certain elements, superconvergent points do not always exist -- e.g. in triangular elements, distorted isoparametric elements, and in elements with varying material properties (hence nonlinear analyses) -- see the discussion by Hiller and Bathe [22]. Three widely used procedures that do not require the knowledge of superconvergent points are the 'posterior equilibrium method' (PEM), the 'recovery by equilibrium in patches' (REP) method, and the 'recovery by compatibility in patches' (RCP) method.

The PEM was proposed by Stein and Ohnimus [23] and is based on the work published earlier by Stein and Ahmad [24], [25]. This method uses the principle of virtual work to calculate improved interelement tractions for the purposes of local error estimation [23], [26]. The REP method was proposed by Boroomand and Zienkiewicz [27], [28]. This method uses the principle of virtual work to calculate improved stresses within the finite element domain. The RCP method was proposed by Ubertini [29] and further developed by Benedetti et al. [30]. This method uses the principle of minimum complementary energy to calculate improved stresses that satisfy point-wise equilibrium. Later, Castellazzi et al. established a solution error estimate based on the RCP method to guide adaptive meshing [31].

All three stress calculation procedures yield impressive results that exceed the performance of the superconvergent patch recovery method. However, to ensure a well-posed problem for the solution of the unknown stress coefficients, several assumptions are employed, and these assumptions limit the accuracy of the results.

Specifically, the PEM assumes that the improved interelement tractions are approximately equal (by a difference minimization) to the tractions directly-calculated from the displacement solution [23]; the REP method uses element nodal point forces that correspond to individual stress components [28]; and the RCP method imposes differential equilibrium for all points in the element [30], a constraint which is too severe, and as a result the RCP solution is not reliable for all classes of problems.

Recently, we proposed the NPF-based method; see refs. [35], [36] and appendix A. This procedure also employs the principle of virtual work, but without the assumptions used in the earlier methods. While the numerical results in refs. [35], [36] are encouraging, the method still requires to consider specific element stress domains and some stress averaging. We concluded, see refs. [35], [36], that a variational basis was necessary to obtain further insight and possibly improve the schemes.

For various problems in engineering and the sciences -- like in the analysis of (almost) incompressible media, thin structures, and multiphysics phenomena -- optimal finite element discretisations can only be obtained if mixed variational formulations are used [1], [38] to [47]. Indeed, in ref. [48], Mota and Abel show that the stress smoothing, L_2 projection and superconvergent patch recovery techniques are based on the use of the Hu-Washizu principle.

Our objective in this thesis is to show that the PEM and the REP, RCP, and NPF-based methods are also all based, with certain assumptions, on the Hu-Washizu variational principle, and then present a novel and significantly improved method for stress predictions. Throughout we focus on the use of low-order displacement-based finite element discretisations of solids, that is, 2-node elements in 1D

solutions, 3-node triangular and 4-node quadrilateral elements in 2D solutions, and 4-node tetrahedral and 8-node brick elements in 3D solutions. These elements are computationally efficient provided good stress convergence is obtained.

We analyse the new stress improvement method in detail for 1D problems with arbitrary loading and material properties, but constant cross-sectional area (using 2-node elements), and prove that the procedure is reliable, giving stresses that are, in fact, optimal stress predictions (in the norm used), with the order of convergence being quadratic, i.e. with the same order as the displacements. This order of stress convergence is also seen numerically in 1D and 2D solutions. In a study, we compare the performance of the new method with the performance of the other above-mentioned procedures. It is important to note that we consider static, dynamic and nonlinear solutions.

Throughout the thesis we use the notation of ref. [1]. We note that most of the material presented herein is close -- sometimes even verbatim -- to that published in our papers; see refs. [35] to [37].

Chapter 1

Fundamental equations

Consider the equilibrium of a body of volume V and surface area S, subjected to externally applied surface tractions $\underline{f}^S$ on the area S_f and body forces $\underline{f}^B$. The body is supported on the area S_u with prescribed displacements $\underline{u}_p$, and, for now, linear analysis conditions are assumed; see *Fig. 1.1*. We seek to calculate the unknown displacements, strains and stresses.

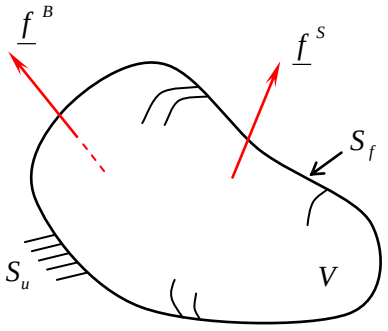

Fig. 1.1: *General 3D body, in linear static conditions, of volume V and surface area S, where $S_u \cup S_f = S$ and $S_u \cap S_f = 0$*

In the differential formulation of the problem, the unknown response is calculated by solving the governing differential equations of equilibrium and compatibility,

with the constitutive relationships, subject to the applied boundary conditions. That is, we solve

$$\begin{aligned} div\left[\underline{\tau}_{ex}\right] + \underline{f}^{B} &= \underline{0} \\ \underline{\varepsilon}_{ex} &= \underline{\partial}_{\varepsilon}\, \underline{u}_{ex} \\ \underline{\tau}_{ex} &= \underline{\underline{C}}\, \underline{\varepsilon}_{ex} \end{aligned}$$

subject to

$$\begin{aligned} \underline{u}_{ex} &= \underline{u}_{p} \quad on\ S_u \\ \underline{f}^{S} &= \underline{\tau}_{ex}\, \underline{n} \quad on\ S_f \end{aligned}$$

where $\underline{u}_{ex}$, $\underline{\varepsilon}_{ex}$ and $\underline{\tau}_{ex}$ are the exact displacements, strains and stresses, respectively, $\underline{\partial}_{\varepsilon}$ is the differential operator on $\underline{u}_{ex}$ to obtain the strain components $\underline{\varepsilon}_{ex}$, $\underline{\underline{C}}$ is the stress-strain matrix, and $\underline{n}$ is the unit outward normal vector on the surface S_f.

A second (but entirely equivalent) approach to the solution of the problem is given by minimising the total potential energy $\Pi(\underline{u})$,

$$\Pi(\underline{u}) = \int_V \frac{1}{2} \underline{\varepsilon}^T\, \underline{\tau}\, dV - \int_{S_f} \underline{u}^T\, \underline{f}^S\, dS - \int_V \underline{u}^T\, \underline{f}^B\, dV \qquad (1.1)$$

with the constraints

$$\begin{aligned} \underline{\varepsilon} &= \underline{\partial}_{\varepsilon}\, \underline{u} \\ \underline{\tau} &= \underline{\underline{C}}\, \underline{\varepsilon} \\ \underline{u} &= \underline{u}_{p} \quad on\ S_u \end{aligned} \qquad (1.2)$$

where $\underline{u}$ is any displacement field satisfying the boundary condition on S_u, and $\underline{\varepsilon}$ and $\underline{\tau}$ are the strains and stresses corresponding to $\underline{u}$.

For approximate solutions, a larger class of trial functions can be employed when we operate on the total potential energy rather than on the differential formulation of the problem; see refs. [1], [14]. This has important consequences, and much of the success of the finite element method hinges on this fact.

Chapter 2

Finite element methods for stress predictions

In this chapter, we first review the displacement-based finite element method; then we present a mixed formulation based on the Hu-Washizu principle. Thereafter, we specialise this mixed formulation to arrive at the basic equations of the PEM and the REP, RCP, and NPF-based methods. Finally, we use this mixed formulation -- and its properties -- to present our new stress improvement scheme.

2.1 Displacement-based finite element method

In the displacement-based finite element method, we assume a displacement pattern within each element m, that is, $\underline{u}^{(m)} = \underline{H}^{(m)} \underline{\hat{U}}$, where $\underline{H}^{(m)}$ is the displacement interpolation matrix, and $\underline{\hat{U}}$ lists the nodal point displacements of the assemblage (including those at the supports).

With this assumption, the strains $\underline{\varepsilon}^{(m)}$ and stresses $\underline{\tau}_h^{(m)}$ of element m follow directly from Eq. (1.2),

$$\underline{\varepsilon}^{(m)} = \underline{\partial}_\varepsilon \, \underline{u}^{(m)} = \underline{B}^{(m)} \underline{\hat{U}} \qquad (2.1)$$

$$\underline{\tau}_h^{(m)} = \underline{C}^{(m)} \, \underline{\varepsilon}^{(m)} = \underline{C}^{(m)} \, \underline{B}^{(m)} \underline{\hat{U}} \qquad (2.2)$$

Then, minimising Π of Eq. (1.1) yields

$$\left[\sum_{m=1}^{N} \left(\int_{V^{(m)}} \underline{B}^{(m)T} \, \underline{C}^{(m)} \, \underline{B}^{(m)} \, dV \right) \right] \underline{\hat{U}} = \left\{ \sum_{m=1}^{N} \left(\int_{S_f^{(m)}} \underline{H}^{(m)T} \, \underline{f}^{S} \, dS + \int_{V^{(m)}} \underline{H}^{(m)T} \, \underline{f}^{B} \, dV \right) \right\} \qquad (2.3)$$

where $\underline{B}^{(m)}$, $\underline{C}^{(m)}$, $V^{(m)}$, and $S_f^{(m)}$ are the strain-displacement matrix, the stress-strain matrix, the volume, and the surface area with externally applied tractions of element m, respectively. We sum over all elements N in the mesh and use Eq. (2.3) to obtain $\underline{\hat{U}}$; see for example ref. [1]. Finally, $\underline{\tau}_h^{(m)}$ is calculated using Eq. (2.2).

In the following, we focus on the use of low-order finite element discretisations (the 2-node element in 1D solutions, the 3-node and 4-node elements in 2D solutions, etc.). It is well known that the accuracy of $\underline{\tau}_h^{(m)}$ is then poor, as compared with the accuracy of the calculated displacements, and this deficiency can be seen using stress band plots of unsmoothed stresses [1], [3] to [14]. We refer to these stresses as the “directly-calculated finite element stresses”.

2.2 Mixed formulation

To arrive at accurate stress predictions, a mixed interpolation approach -- which can be thought of as a special use of the Hu-Washizu principle -- can be more effective. In this formulation, rather than applying the stress-strain relationship point-wise, we relax this relationship and apply it over the element volumes using Lagrange multipliers. The primary solution variables are then the unknown displacements, Lagrange multipliers and stresses. Hence, the equivalent of the minimisation of Π in Eq. (1.1) is

$$\Pi^* \left(\underline{u}^{(m)}, \underline{\lambda}^{(m)}, \underline{\tau}^{(m)} \right) = \sum_{m=1}^{N} \left(\int_{V^{(m)}} \frac{1}{2} \underline{\varepsilon}^{(m)T} \underline{\tau}^{(m)} \, dV - \int_{S_f^{(m)}} \underline{u}^{(m)T} \underline{f}^{S} \, dS - \int_{V^{(m)}} \underline{u}^{(m)T} \underline{f}^{B} \, dV \right.$$
$$\left. - \int_{V^{(m)}} \underline{\lambda}^{(m)T} \left\{ \underline{\tau}^{(m)} - \underline{C}^{(m)} \underline{\varepsilon}^{(m)} \right\} dV \right) \qquad (2.4)$$
$$= \textit{stationary}$$

with the constraints

$$\underline{\varepsilon}^{(m)} = \underline{\partial}_{\varepsilon} \underline{u}^{(m)} \qquad (2.5)$$
$$\underline{u}^{(m)} = \underline{u}_p \quad \textit{on } S_u$$

As in the displacement-based finite element method, the displacements $\underline{u}^{(m)}$ of element m are defined by nodal point variables that pertain to adjacent elements in the assemblage, $\underline{u}^{(m)} = \underline{H}^{(m)} \underline{\hat{U}}$, and the strains $\underline{\varepsilon}^{(m)}$ follow directly from Eq. (2.5), $\underline{\varepsilon}^{(m)} = \underline{B}^{(m)} \underline{\hat{U}}$. However, the Lagrange multipliers $\underline{\lambda}^{(m)}$ and the stresses $\underline{\tau}^{(m)}$ of element m are defined by internal degrees of freedom that pertain only to the specific element *m* considered.

In order to furnish improved stress predictions, we must assume a richer space for $\underline{\tau}^{(m)}$ than that implicitly assumed for $\underline{\tau}_h^{(m)}$. Also, we want to enhance the fulfilment of equilibrium. Hence, we now assume

$$dim(\ \underline{\tau}^{(m)}) \geq dim(\ \underline{\lambda}^{(m)}) \geq dim(\ \underline{\varepsilon}^{(m)}) \qquad (2.6)$$

and

$$\int_{V^{(m)}} \delta \underline{\zeta}^{(m)T} \left\{ div\left[\underline{\tau}^{(m)}\right] + \underline{f}^{B} \right\} dV = 0 \qquad (2.7)$$

where *dim (.)* denotes the dimension of the space of the variable considered, δ denotes, as usual, "variation of", $\underline{\zeta}^{(m)}$ is defined by degrees of freedom, and the square parentheses indicate that the stress vector has been arranged into matrix form.

With this assumption, invoking the stationarity of Π^* with respect to $\underline{u}^{(m)}$, $\underline{\lambda}^{(m)}$ and $\underline{\tau}^{(m)}$ yields

$$\sum_{m=1}^{N} \left(\int_{V^{(m)}} \delta \underline{\varepsilon}^{(m)T} \left\{ \frac{1}{2} \underline{\tau}^{(m)} + \underline{C}^{(m)} \underline{\lambda}^{(m)} \right\} dV \right) - \int_{S_f^{(m)}} \delta \underline{u}^{(m)T} \underline{f}^{S} \, dS \qquad (2.8)$$
$$- \int_{V^{(m)}} \delta \underline{u}^{(m)T} \underline{f}^{B} \, dV = 0$$

$$\int_{V^{(m)}} \delta \underline{\lambda}^{(m)T} \left\{ \ \underline{\tau}^{(m)} - \underline{C}^{(m)} \underline{\varepsilon}^{(m)} \right\} dV = 0 \qquad \forall \quad m \qquad (2.9)$$

$$\underline{\lambda}^{(m)} = \frac{1}{2} \underline{\varepsilon}^{(m)} \qquad \forall \quad m \qquad (2.10)$$

Since Eq. (2.9) holds for all variations of $\underline{\lambda}^{(m)}$, including when $\delta\underline{\lambda}^{(m)} = \frac{1}{2}\delta\underline{\varepsilon}^{(m)}$, Eq. (2.8) contains as a special case

$$\sum_{m=1}^{N}\left(\int_{V^{(m)}} \delta\underline{\varepsilon}^{(m)T}\left\{\frac{1}{2}\underline{C}^{(m)}\underline{\varepsilon}^{(m)} + \underline{C}^{(m)}\underline{\lambda}^{(m)}\right\} dV - \int_{S_f^{(m)}} \delta\underline{u}^{(m)T}\,\underline{f}^{S}\, dS - \int_{V^{(m)}} \delta\underline{u}^{(m)T}\,\underline{f}^{B}\, dV\right) = 0$$

Then, using the solution $\underline{\lambda}^{(m)} = \frac{1}{2}\underline{\varepsilon}^{(m)}$ from Eq. (2.10) we obtain

$$\sum_{m=1}^{N}\left(\int_{V^{(m)}} \delta\underline{\varepsilon}^{(m)T}\,\underline{C}^{(m)}\,\underline{\varepsilon}^{(m)}\, dV - \int_{S_f^{(m)}} \delta\underline{u}^{(m)T}\,\underline{f}^{S}\, dS - \int_{V^{(m)}} \delta\underline{u}^{(m)T}\,\underline{f}^{B}\, dV\right) = 0 \quad (2.11)$$

Of course, when inserting the element interpolations, Eq. (2.11) gives Eq. (2.3). Here Eq. (2.11) (and hence Eq. (2.3)) would give -- at this stage -- a specific solution of the stresses in the stress space of $\underline{\tau}^{(m)}$, namely $\underline{\tau}_h^{(m)}$. However, to complete the calculation of the improved stresses we also use Eqs. (2.7) and (2.9).

An important practical feature of this 'mixed formulation' is that the displacement problem in Eq. (2.11) is decoupled from the additional calculations of the stresses. Therefore, in a general analysis, we first solve for $\underline{u}^{(m)}$ as is standard, and then -- rather than applying the stress-strain relationship -- we obtain $\underline{\tau}^{(m)}$ from $\underline{u}^{(m)}$ by applying Eqs. (2.7) and (2.9) to *each* element m in the assemblage.

This element-based approach works well in 1D solutions; however, in 2D and 3D solutions, better results are obtained when the stresses are defined over a predetermined patch of N_P elements, known as the stress calculation domain. In this case, $\underline{\tau}^{(m)}$ is obtained from $\underline{u}^{(m)}$ by applying Eqs. (2.7) and (2.9) either to

each element m in the stress calculation domain, or to the *entire* stress calculation domain,

$$\sum_{m=1}^{N_P}\left(\int_{V^{(m)}} \delta \underline{\lambda}^{(m)T} \left\{ \underline{\tau}^{(m)} - \underline{C}^{(m)} \underline{\varepsilon}^{(m)} \right\} dV \right) = 0 \qquad (2.12)$$

$$\sum_{m=1}^{N_P}\left(\int_{V^{(m)}} \delta \underline{\zeta}^{(m)T} \left\{ div\left[\underline{\tau}^{(m)}\right] + \underline{f}^{B} \right\} dV \right) = 0 \qquad (2.13)$$

Since $\underline{\tau}^{(m)}$ is obtained from $\underline{u}^{(m)}$, the accuracy of $\underline{\tau}^{(m)}$ is limited by that of $\underline{u}^{(m)}$; hence, the highest order of convergence of the stresses that we can expect is $O\left(h^2\right)$ -- one order higher than that observed for $\underline{\tau}_h^{(m)}$. To obtain $O\left(h^2\right)$ convergence, we must interpolate $\underline{\tau}^{(m)}$ with complete polynomials of at least degree 1.

The key question for the formulation is now: What interpolations should be used for $\underline{\lambda}^{(m)}$ and $\underline{\zeta}^{(m)}$ to ensure a well-posed problem with stresses that converge at order $O\left(h^2\right)$? Indeed, the choice of interpolation determines the number of equations available and the accuracy of the results. Examples are given below.

2.3 The PEM and the REP method

In the PEM and the REP method, $\underline{\lambda}^{(m)}$ is interpolated in the same way as the strains $\underline{\varepsilon}^{(m)}$, and $\underline{\zeta}^{(m)}$ is interpolated in the same way as the displacements $\underline{u}^{(m)}$. With this assumption, we obtain from Eqs. (2.12) and (2.13)

$$\sum_{m=1}^{N_P}\left(\int_{V^{(m)}}\ \delta\underline{\varepsilon}^{(m)T}\ \underline{\tau}^{(m)}\ dV\right)=\sum_{m=1}^{N_P}\left(\ \delta\underline{\hat{U}}^{\ T}\ \underline{F}^{(m)}\ \right)\qquad(2.14)$$

$$\sum_{m=1}^{N_P}\left(\int_{V^{(m)}}\ \delta\underline{u}^{(m)T}\left\{div\left[\underline{\tau}^{(m)}\right]+\underline{f}^{\ B}\right\}dV\right)=0\qquad(2.15)$$

where $\delta\underline{\hat{U}}$ are the virtual nodal point displacements that correspond to $\delta\underline{\varepsilon}^{(m)}$, and $\underline{F}^{(m)}$ are the element nodal point forces, in fact already used in Eq. (2.3),

$$\underline{F}^{(m)}=\int_{V^{(m)}}\ \underline{B}^{(m)T}\ \underline{\tau}_h^{(m)}\ dV=\left[\int_{V^{(m)}}\ \underline{B}^{(m)T}\ \underline{C}^{(m)}\ \underline{B}^{(m)}\ dV\right]\underline{\hat{U}}\qquad(2.16)$$

Using the mathematical identity,

$$\delta\underline{u}^{(m)T}\ div\left[\underline{\tau}^{(m)}\right]=div\left(\delta\underline{u}^{(m)T}\left[\underline{\tau}^{(m)}\right]\right)-\delta\underline{\varepsilon}^{(m)T}\ \underline{\tau}^{(m)}$$

the Gauss divergence theorem and Eq. (2.14), we can write Eq. (2.15) as

$$\sum_{m=1}^{N_P}\left(\int_{S_f^{(m)}}\ \delta\underline{u}^{(m)T}\left[\underline{\tau}^{(m)}\right]\underline{n}^{(m)}\ dS+\int_{V^{(m)}}\ \delta\underline{u}^{(m)T}\ \underline{f}^{\ B}\ dV\right)=\sum_{m=1}^{N_P}\left(\ \delta\underline{\hat{U}}^{\ T}\ \underline{F}^{(m)}\ \right)\qquad(2.17)$$

where $\underline{n}^{(m)}$ is the unit normal to the boundary surface $S_f^{(m)}$ of element m.

Eq. (2.17) is the basic equation of the PEM, and Eq. (2.14) is the basic equation of the REP method. That is, for any virtual displacement pattern contained in the interpolation functions, the PEM balances the virtual work of the boundary tractions (adjusted for body force effects) with the virtual work of the nodal point forces; whereas, the REP method balances the internal virtual work of the stresses with the virtual work of the nodal point forces.

Since each method uses only one principle of virtual work statement (of the two possible statements given by the mixed formulation), the governing matrices corresponding to the basic equations of the PEM and the REP method may be singular; hence, several assumptions are employed to add extra constraints (and these assumptions limit the accuracy of the results) -- see refs. [23], [28].

2.4 The RCP method

Let $\mathbf{V}^{\tau}$ be the assumed stress space for $\underline{\tau}^{(m)}$, and let $\overline{\mathbf{V}}^{\tau}$ be the subspace of the self-equilibrated stresses in $\mathbf{V}^{\tau}$. Then, let $\underline{\bar{\tau}}^{(m)}$ be any element in that subspace

$$\overline{\mathbf{V}}^{\tau} = \left\{ \underline{\bar{\tau}}^{(m)} \,\middle|\, \underline{\bar{\tau}}^{(m)} \in \mathbf{V}^{\tau};\ \ div\left[\underline{\bar{\tau}}^{(m)}\right] = \underline{0} \right\} \qquad (2.18)$$

In the RCP method, $\underline{\lambda}^{(m)}$ is interpolated in the same way as $\underline{\underline{C}}^{(m)-1}\ \underline{\bar{\tau}}^{(m)}$, and $\underline{\zeta}^{(m)}$ is any element in $L^2\left(V_p\right)$, where $L^2\left(V_p\right)$ is the space of square integrable functions in the volume, V_p, of the stress calculation domain. With this assumption, we obtain from Eqs. (2.12) and (2.13)

$$\sum_{m=1}^{N_P} \left(\int_{V^{(m)}} \delta \underline{\bar{\tau}}^{(m)T} \left\{ \underline{\underline{C}}^{(m)-1}\ \underline{\tau}^{(m)} - \underline{\varepsilon}^{(m)} \right\} dV \right) = 0 \qquad (2.19)$$

$$div\left[\underline{\tau}^{(m)}\right] + \underline{f}^{B} = 0 \qquad (2.20)$$

Eqs. (2.19) and (2.20) are basic equations of the RCP method. To satisfy Eq. (2.20), an *a priori* particular solution $\underline{\tau}_{p.s.}^{(m)}$ to the differential equations of equilibrium is embedded in $\underline{\tau}^{(m)}$ [29], [30]. However, establishing $\underline{\tau}_{p.s.}^{(m)}$ for distorted isoparametric elements in dynamic analysis is difficult and an outstanding issue to be solved. Moreover, the differential equilibrium constraint in Eq. (2.20) is too severe, and as a result the RCP solution is not reliable for all classes of problems; see chapter 4.

Considering nonlinear analysis, a complication with the RCP method is that the basic equations involve the use of the constitutive relationships; hence, in problems with path-dependent nonlinear material conditions, an incremental solution procedure may have to be used to solve for the unknown stress coefficients in Eq. (2.19).

2.5 The NPF-based method

In the NPF-based method, $\underline{\lambda}^{(m)}$ is interpolated in the same way as the strains $\underline{\varepsilon}^{(m)}$, and $\underline{\zeta}^{(m)}$ is interpolated in the same way as the displacements $\underline{u}^{(m)}$. With this assumption we obtain from Eqs. (2.9) and (2.7)

$$\int_{V^{(m)}} \delta \underline{\varepsilon}^{(m)T} \underline{\tau}^{(m)} \, dV = \delta \underline{\hat{U}}^{T} \underline{F}^{(m)} \qquad (2.21)$$

$$\int_{V^{(m)}} \delta \underline{u}^{(m)T} \left\{ div\left[\underline{\tau}^{(m)}\right] + \underline{f}^{B} \right\} dV = 0 \qquad (2.22)$$

where $\underline{F}^{(m)}$ is defined in Eq. (2.16), and we can write Eq. (2.22) as

$$\int_{S_f^{(m)}} \delta \underline{u}^{(m)T} \left[\underline{\tau}^{(m)}\right] \underline{n}^{(m)} \, dS + \int_{V^{(m)}} \delta \underline{u}^{(m)T} \, \underline{f}^{B} \, dV = \delta \hat{\underline{U}}^{T} \underline{F}^{(m)} \qquad (2.23)$$

using similar steps as those used to obtain Eq. (2.17).

Eqs. (2.21) and (2.23) are the basic equations of the NPF-based method. In contrast to the PEM and the REP method, the NPF-based method uses both principle of virtual work statements, Eqs. (2.21) and (2.23), and applies them to each element m in the stress calculation domain. Consequently, the problem solution for the unknown NPF-based stress coefficients is well-posed, without the (limiting) assumptions used in the earlier methods.

However, a drawback of the NPF-based method is that the number of equations available -- and hence the dimension of the interpolation functions assumed in $\mathbf{v}^{\tau}$ -- is dependent on the number (and type) of elements in the stress calculation domain. Therefore, to get close to $O\left(h^2\right)$ convergence for the stresses, a large stress domain is needed, and a domain stress averaging procedure has been employed; see refs. [35], [36] and appendix A.

2.6 The new stress improvement method

In this section, we present a novel and significantly improved method for stress predictions. We first develop the method for linear static and dynamic analysis; then, we extend the method to nonlinear solutions; finally, we consider the computational cost of the technique.

2.6.1 Linear static and dynamic analysis

The new stress improvement method assumes $\underline{\lambda}^{(m)}$ is interpolated in the same way as the self-equilibrated stresses $\underline{\bar{\tau}}^{(m)}$, and $\underline{\zeta}^{(m)}$ is any element in $P_1\left(V_p\right)$, where $P_k\ \left(\ V_p\ \right)$ is the space of complete polynomials of degree *k* in the volume of the stress calculation domain V_p. With this assumption, we obtain from Eqs. (2.12) and (2.13)

$$\sum_{m=1}^{N_P}\left(\int_{V^{(m)}}\delta\underline{\bar{\tau}}^{(m)T}\left\{\ \underline{\tau}^{(m)}-\underline{\tau}_h^{(m)}\ \right\}dV\right)=0 \qquad (\ 2.24\ )$$

$$\sum_{m=1}^{N_P}\left(\int_{V^{(m)}}\delta\underline{\zeta}^{(m)T}\left\{div\left[\underline{\tau}^{(m)}\right]+\underline{f}^{\,B}\ \right\}dV\right)=0 \qquad (\ 2.25\ )$$

where the stresses $\underline{\tau}^{(m)}$ are assumed to be continuous and quadratically interpolated across the stress calculation domain, $\underline{\tau}^{(m)}\in P_2\left(V_p\ \right)$, and the subspace of self-equilibrated stresses, $\overline{\nabla}^{\tau}$, is given by

$$\overline{\nabla}^{\tau}=\left\{\ \underline{\bar{\tau}}^{(m)}\ \middle|\ \underline{\bar{\tau}}^{(m)}\in P_2\left(V_p\ \right);\ \ div\left[\underline{\bar{\tau}}^{(m)}\right]=\underline{0}\ \right\} \qquad (\ 2.26\ )$$

Eqs. (2.24) and (2.25) are the basic equations used. These correspond to projecting the differences in the assumed and directly-calculated stresses onto the space $\overline{\nabla}^{\tau}$, and to projecting the divergence of the error between the assumed and exact stresses onto P_1.

To obtain the corresponding finite element equations, we introduce the interpolations

$$\underline{\tau}^{(m)} = \underline{E}_\tau \, \underline{\hat{\tau}}, \qquad \underline{\bar{\tau}}^{(m)} = \underline{\bar{E}}_\tau \, \underline{\hat{\bar{\tau}}}, \qquad \underline{\zeta}^{(m)} = \underline{E}_\zeta \, \underline{\hat{\zeta}} \tag{2.27}$$

where the interpolation matrices $\underline{E}_\tau$, $\underline{\bar{E}}_\tau$, and $\underline{E}_\zeta$ are given in Eq. (3.1) for 1D analysis, and in Eqs. (4.1) to (4.3), respectively, for 2D analysis. Note that in these matrices, locally based coordinate origins are used to avoid ill-conditioning, and $div\left[\underline{\bar{E}}_\tau\right] = \underline{0}$, as is required by Eq. (2.26).

Substituting from Eq. (2.27) into Eqs. (2.24) and (2.25) we arrive at

$$\left[\sum_{m=1}^{N_P}\begin{pmatrix} \int_{V^{(m)}} \underline{\bar{E}}_\tau^T \, \underline{E}_\tau \, dV \\ \int_{V^{(m)}} \underline{E}_\zeta^T \, \underline{\partial}_\tau \underline{E}_\tau \, dV \end{pmatrix}\right] \underline{\hat{\tau}} = \left\{\sum_{m=1}^{N_P}\begin{pmatrix} \int_{V^{(m)}} \underline{\bar{E}}_\tau^T \, \underline{\tau}_h^{(m)} \, dV \\ -\int_{V^{(m)}} \underline{E}_\zeta^T \, \underline{f}^B \, dV \end{pmatrix}\right\} \tag{2.28}$$

where $\underline{\partial}_\tau$ is the differential operator on $\underline{\tau}^{(m)}$ to obtain the divergence of the stress field (see Eqs. (3.2) and (4.4)), $\underline{\hat{\tau}}$ lists the unknown stress coefficients to be found, and, in dynamic analysis, we must include the d'Alembert inertia forces in $\underline{f}^B$; see chapter 4.5.

Since $\underline{\tau}^{(m)} \in P_2\left(V_p\right)$, and $\underline{\bar{\tau}}^{(m)} \in \overline{\mathbf{V}}^\tau$, $\underline{\zeta}^{(m)} \in P_1\left(V_p\right)$, it follows that Eq. (2.28) represents a determined system of equations in terms of $\underline{\hat{\tau}}$ -- *irrespective* of the number (and type) of elements used in the stress calculation domain -- such that a unique solution for $\underline{\hat{\tau}}$ always exists, even if only one element is used in the stress calculation domain.

To summarise, the important attributes of the new method are:

1. The assumed stresses $\underline{\tau}^{(m)}$ are interpolated with complete polynomials of degree 2; hence, the order of convergence of $\underline{\tau}^{(m)}$ is expected to be $O\left(h^2\right)$.
2. The number of equations available is independent of the number (and type) of elements used in the stress calculation domain.
3. The system of equations is always determined.
4. The equations do not involve the use of the constitutive relationships (other than in the calculation of $\underline{\tau}_h^{(m)}$).
5. The stress calculations can be performed for the entire assemblage, or just in localised regions of concern.
6. The fulfilment of differential equilibrium is enhanced, and differential equilibrium is fulfilled at every point in the element if $\underline{f}^B \in P_1$.
7. The method does not use an *a priori* particular solution (like used in the RCP method).
8. The solution will not be afflicted with a spurious checkerboard mode of constant element stresses.

Spurious checkerboard modes of constant element stresses can be found in some displacement-stress solutions -- see *Fig. 2.1* and ref. [1]. To prove that the improved stresses $\underline{\tau}^{(m)}$ are not afflicted we use that

$$\sum_{m=1}^{N_P}\left(\int_{V^{(m)}} \underline{\tau}^{(m)}\, dV\right) = \sum_{m=1}^{N_P}\left(\int_{V^{(m)}} \underline{\tau}_h^{(m)}\, dV\right) \qquad (2.29)$$

which follows directly from Eq. (2.24), and note that the directly-calculated stresses $\underline{\tau}_h^{(m)}$ are not afflicted.

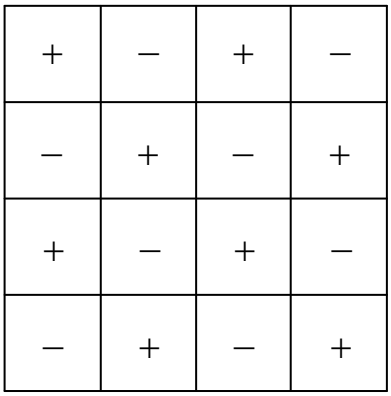

Fig. 2.1: *Checkerboard mode of constant element stress. Here* $+$ *and* $-$ *mean* $+\Delta\tau_{ij}^{(m)}$ *and* $-\Delta\tau_{ij}^{(m)}$*, where* $\Delta\tau_{ij}^{(m)}$ *is an arbitrary value [1]*

Also, because the exact stresses satisfy the differential equations of equilibrium, we can write Eq. (2.25) as

$$\sum_{m=1}^{N_P}\left(\int_{V^{(m)}} \delta\underline{\zeta}^{(m)T} div\left[\underline{\tau}^{(m)}\right]dV\right)=\sum_{m=1}^{N_P}\left(\int_{V^{(m)}} \delta\underline{\zeta}^{(m)T} div\left[\underline{\tau}_{ex}\right]dV\right) \quad (2.30)$$

such that

$$\sum_{m=1}^{N_P}\left(\int_{V^{(m)}} div\left[\underline{\tau}^{(m)}\right]dV\right)=\sum_{m=1}^{N_P}\left(\int_{V^{(m)}} div\left[\underline{\tau}_{ex}\right]dV\right) \quad (2.31)$$

Eqs. (2.30) and (2.31) are important since they relate the calculated and exact stresses in the volume of the stress calculation domain. Indeed, we shall use these relationships when we consider an error bound on the calculated stresses.

Finally, we note that the PEM, and the REP and NPF-based methods satisfy the condition on $\underline{\lambda}^{(m)}$ given in Eq. (2.6), irrespective of N_P. However, the RCP method and the new method only satisfy this condition when $N_P=1$ (because

these two methods assume $\underline{\lambda}^{(m)}$ to be continuous across element boundaries whereas $\underline{\varepsilon}^{(m)}$ does not show that continuity).

2.6.2 Nonlinear analysis

In nonlinear analyses, all theory presented is applicable, but of course the current volumes and current Cauchy stresses must be used; see ref. [1]. That is, if t denotes "in the current configuration", the stress coefficients ${}^{t}\underline{\hat{\tau}}$ are obtained using

$$\left[\sum_{m=1}^{N_P}\begin{pmatrix}\int_{{}^{t}V^{(m)}} \underline{\overline{E}}_{\tau}^{T}\,\underline{E}_{\tau}\,dV \\ \int_{{}^{t}V^{(m)}} \underline{E}_{\zeta}^{T}\,\underline{\partial}_{\tau}\underline{E}_{\tau}\,dV\end{pmatrix}\right]{}^{t}\underline{\hat{\tau}} = \left\{\sum_{m=1}^{N_P}\begin{pmatrix}\int_{{}^{t}V^{(m)}} \underline{\overline{E}}_{\tau}^{T}\,{}^{t}\underline{\tau}_{h}^{(m)}\,dV \\ -\int_{{}^{t}V^{(m)}} \underline{E}_{\zeta}^{T}\,{}^{t}\underline{f}^{B}\,dV\end{pmatrix}\right\} \qquad (2.32)$$

where ${}^{t}V^{(m)}$ is the current volume of element m (obtained using the displacement solution ${}^{t}\underline{\hat{U}}$), ${}^{t}\underline{\tau}_{h}^{(m)}$ lists the directly-calculated Cauchy stresses at time t, and ${}^{t}\underline{\hat{U}}$ is established using a step-by-step incremental solution procedure [1].

Therefore, once ${}^{t}\underline{\hat{U}}$ has been established, the enhanced stress predictions are obtained using Eq. (2.32), as in linear analysis.

2.6.3 Computational expense

The computational expense to furnish improved stress predictions is given by the numerical effort involved in solving for 18 unknown stress coefficients in 2D solutions (and the 60 unknown stress coefficients in 3D solutions), for each element m where stresses are to be improved.

This expense is small, as compared with factorising the global stiffness matrix. Indeed, in a typical 2D linear static analysis problem (with 10^5 degrees of freedom, meshed using 4-node elements), the expense to enhance the stresses for the *entire* assemblage is about 1% of the total solution cost; see *Table 2.1*. In nonlinear analyses the expense is, relatively, even lower, because a step-by-step solution procedure is needed to obtain ${}^t\underline{\hat{U}}$.

4-node quadrilateral 2D elements

No. of degrees of freedom	*No. of elements*	*Half-bandwidth of $\underline{K}$*	*Cost of enhancing the stresses*
1.0E+05	5.0E+04	454	1.4%
1.0E+06	5.0E+05	1,418	0.14%
1.0E+07	5.0E+06	4,532	0.014%

8-node hexahedral (brick) 3D elements

No. of degrees of freedom	*No. of elements*	*Half-bandwidth of $\underline{K}$*	*Cost of enhancing the stresses*
1.0E+05	3.3E+04	3,372	0.63%
1.0E+06	3.3E+05	14,916	0.032%
1.0E+07	3.3E+06	67,956	0.0015%

Table 2.1: *Estimate of the computational cost to establish the enhanced stresses for the entire assemblage, as compared with the total solution cost, for typical: (a) 2D and (b) 3D linear static analysis problems. The estimate does not include the cost of the element computations, and this would make the comparison more favourable*

Of course, in practice, the stress calculations need not be performed for the entire assemblage, but instead might be performed only for those elements where stresses should be improved.

Chapter 3

Insight into the new method in 1D solutions

In this chapter, we first present the solution procedure of the new stress improvement method in 1D settings, then we analyse the method in detail. Thereafter, we compare the performance of the new method with that of the PEM and the REP method.

3.1 Matrices used in 1D solutions

In the following, we consider the 1D case with only one stress component, for arbitrary loading and material properties, and assume that the cross-sectional area of the 1D structure is constant. In this case, an element-based approach is adopted. Hence, to solve for the unknown stress coefficients $\underline{\hat{\tau}}$ for a general element m, we apply Eq. (2.28) with $N_P = 1$,

$$\underline{E}_\tau = \begin{bmatrix} 1 & x & x^2 \end{bmatrix}, \qquad \overline{\underline{E}}_\tau = \begin{bmatrix} 1 \end{bmatrix}, \qquad \underline{E}_\zeta = \begin{bmatrix} 1 & x \end{bmatrix} \tag{3.1}$$

and

$$\underline{\partial}_\tau = \begin{bmatrix} \dfrac{d}{dx} \end{bmatrix} \tag{3.2}$$

where $\underline{\hat{\tau}} = \begin{Bmatrix} \alpha_1 & \alpha_2 & \alpha_3 \end{Bmatrix}^T$, and x is the element *m* local coordinate system.

3.2 Reliability and improvement in stress prediction

The fundamental objective of the new procedure is to enhance the accuracy of the stresses. Mathematically, therefore, our goal is to find stresses $\underline{\tau}^{(m)}$ such that

$$\sum_{m=1}^{N} \left\| \underline{\tau}_{ex} - \underline{\tau}^{(m)} \right\|_{V^{(m)}} \leq c \sum_{m=1}^{N} \left\| \underline{\tau}_{ex} - \underline{\tau}_h^{(m)} \right\|_{V^{(m)}} \tag{3.3}$$

with a constant $c < 1$, dependent on the problem, and ideally $c << 1$.

Here we use the H^1 semi-norm $\|\cdot\|_{V^{(m)}}$, which, when the function in the norm is zero on some part of the boundary, is equivalent to the H^1 norm (by the Poincaré-Friedrichs inequality [1], [2]). The semi-norm is appropriate for the stresses because of Eq. (2.29). We analyse the 1D case considered in chapter 3.1.

In this case, the distance between the calculated and the exact solution is

$$\left\| \tau_{ex} - \tau^{(m)} \right\|^2_{V^{(m)}} = \left\| \tau_{ex} \right\|^2_{V^{(m)}} + \left\| \tau^{(m)} \right\|^2_{V^{(m)}} - 2\left(\int_{V^{(m)}} \left(\frac{d\tau^{(m)}}{dx} \right)\left(\frac{d\tau_{ex}}{dx} \right) dV \right) \quad (3.4)$$

Because $N_P = 1$, Eq. (2.30) gives

$$\int_{V^{(m)}} \delta\zeta^{(m)} \left(\frac{d\tau_{ex}}{dx} \right) dV = \int_{V^{(m)}} \delta\zeta^{(m)} \left(\frac{d\tau^{(m)}}{dx} \right) dV$$

for all variations of $\zeta^{(m)} \in P_1$, including when $\delta\zeta^{(m)} = \left(\frac{d\tau^{(m)}}{dx} \right)$. Therefore

$$\int_{V^{(m)}} \left(\frac{d\tau^{(m)}}{dx} \right)\left(\frac{d\tau_{ex}}{dx} \right) dV = \left\| \tau^{(m)} \right\|^2_{V^{(m)}}$$

and hence we obtain from Eq. (3.4) the result

$$\left\| \tau_{ex} - \tau^{(m)} \right\|^2_{V^{(m)}} = \left\| \tau_{ex} \right\|^2_{V^{(m)}} - \left\| \tau^{(m)} \right\|^2_{V^{(m)}} \quad (3.5)$$

Using the Cauchy-Schwarz inequality [1], [2]

$$\left\| \tau^{(m)} \right\|^2_{V^{(m)}} \geq \frac{1}{V^{(m)}} \left(\int_{V^{(m)}} \left(\frac{d\tau^{(m)}}{dx} \right) dV \right)^2$$

and the property $\int_{V^{(m)}} \left(\frac{d\tau^{(m)}}{dx} \right) dV = \int_{V^{(m)}} \left(\frac{d\tau_{ex}}{dx} \right) dV$, which follows from Eq. (2.31), we have

$$\left\| \tau^{(m)} \right\|^2_{V^{(m)}} \geq \frac{1}{V^{(m)}} \left(\int_{V^{(m)}} \left(\frac{d\tau_{ex}}{dx} \right) dV \right)^2$$

$$= \frac{1}{V^{(m)}} \frac{\left(\int_{V^{(m)}} \left(\frac{d\tau_{ex}}{dx} \right) dV \right)^2}{\int_{V^{(m)}} \left(\frac{d\tau_{ex}}{dx} \right)^2 dV} \left\| \tau_{ex} \right\|^2_{V^{(m)}} \qquad (3.6)$$

In light of Eqs. (3.5) and (3.6), we obtain

$$\left\| \tau_{ex} - \tau^{(m)} \right\|^2_{V^{(m)}} \leq \left(1 - \frac{1}{V^{(m)}} \frac{\left(\int_{V^{(m)}} \left(\frac{d\tau_{ex}}{dx} \right) dV \right)^2}{\int_{V^{(m)}} \left(\frac{d\tau_{ex}}{dx} \right)^2 dV} \right) \left\| \tau_{ex} \right\|^2_{V^{(m)}} \qquad (3.7)$$

Finally, because the displacements vary linearly

$$\left\| \tau_{ex} - \tau_h^{(m)} \right\|^2_{V^{(m)}} = \left\| \tau_{ex} \right\|^2_{V^{(m)}}$$

and hence we obtain from Eq. (3.7) the required result

$$\left\| \tau_{ex} - \tau^{(m)} \right\|_{V^{(m)}} \leq c \left\| \tau_{ex} - \tau_h^{(m)} \right\|_{V^{(m)}} \qquad (3.8)$$

with

$$c = \left(1 - \frac{1}{V^{(m)}} \frac{\left(\int_{V^{(m)}} \left(\frac{d\tau_{ex}}{dx} \right) dV \right)^2}{\int_{V^{(m)}} \left(\frac{d\tau_{ex}}{dx} \right)^2 dV} \right)^{\frac{1}{2}}$$

where $c<1$. It is interesting to note that if $\tau_{ex} \in P_1$, we have $c=0$, such that the calculated stresses are exact (when measured in the H^1 semi-norm), *irrespective* of the coarseness of mesh used.

Eq. (3.8) proves the new method satisfies the fundamental requirement in Eq. (3.3) for each element, as well as for the entire domain. Also, because $\tau_h^{(m)}$ is stable and converging in the norm [1], [14], Eq. (3.8) proves the method is reliable in 1D solutions and the stresses (within each element) are always more accurate than $\tau_h^{(m)}$ when measured in the norm used.

3.3 Optimality of stress prediction

Let $e^{(m)}$ be the point-wise error between the calculated and the exact solution,

$$e^{(m)} = \tau_{ex} - \tau^{(m)}$$

Hence, we have from Eq. (2.30)

$$\int_{V^{(m)}} \delta\zeta^{(m)} \left(\frac{de^{(m)}}{dx} \right) dV = 0 \qquad (3.9)$$

for all variations of $\zeta^{(m)} \in P_1$.

Next consider

$$\left\| e^{(m)} + w^{(m)} \right\|^2_{V^{(m)}} = \left\| e^{(m)} \right\|^2_{V^{(m)}} + \left\| w^{(m)} \right\|^2_{V^{(m)}} + 2\left(\int_{V^{(m)}} \left(\frac{dw^{(m)}}{dx} \right) \left(\frac{de^{(m)}}{dx} \right) dV \right) \qquad (3.10)$$

where $\left(\frac{dw^{(m)}}{dx} \right)$ is any element in P_1.

Using the orthogonality condition given in Eq. (3.9), we find

$$\left\| e^{(m)} + w^{(m)} \right\|^2_{V^{(m)}} = \left\| e^{(m)} \right\|^2_{V^{(m)}} + \left\| w^{(m)} \right\|^2_{V^{(m)}}$$

such that

$$\left\| e^{(m)} \right\|^2_{V^{(m)}} \leq \left\| e^{(m)} + w^{(m)} \right\|^2_{V^{(m)}}$$

Therefore, using $w^{(m)} = \tau^{(m)} - \tilde{\tau}^{(m)}$, we obtain the result

$$\left\| \tau_{ex} - \tau^{(m)} \right\|_{V^{(m)}} \leq \left\| \tau_{ex} - \tilde{\tau}^{(m)} \right\|_{V^{(m)}} \quad \forall \ \tilde{\tau}^{(m)} \in P_2 \qquad (3.11)$$

This gives valuable insight into how the method chooses the stress from the possible patterns contained in the interpolation functions. Indeed, Eq. (3.11) tells that $\tau^{(m)}$ is chosen so as to minimise the error within the volume of *each* element m, i.e. the stress is, in fact, the optimal stress prediction.

3.4 Convergence of stress prediction

An important result of interpolation theory is that there exists an interpolation function $\tau_I^{(m)} \in P_2$ such that

$$\left\| \tau_{ex} - \tau_I^{(m)} \right\|_1 \leq \hat{c} h^2 \left\| \tau_{ex} \right\|_3 \qquad (3.12)$$

where h is the mesh size parameter, $\hat{c}$ is a constant independent of h, and $\left\| \cdot \right\|_k$ is the Sobolev norm of order k in the volume, V, of the body being considered [1], [2].

Using Eq. (3.11) with the case $\tilde{\tau}^{(m)} = \tau_I^{(m)}$, we have

$$\sum_{m=1}^{N} \left\| \tau_{ex} - \tau^{(m)} \right\|_{V^{(m)}} \leq \sum_{m=1}^{N} \left\| \tau_{ex} - \tau_I^{(m)} \right\|_{V^{(m)}} \qquad (3.13)$$

Since $\sum_{m=1}^{N} \left\| \tau_{ex} - \tau_I^{(m)} \right\|_{V^{(m)}} \leq \left\| \tau_{ex} - \tau_I^{(m)} \right\|_1$, we can write Eq. (3.13) as

$$\sum_{m=1}^{N} \left\| \tau_{ex} - \tau^{(m)} \right\|_{V^{(m)}} \leq \left\| \tau_{ex} - \tau_I^{(m)} \right\|_1 \qquad (3.14)$$

and hence we obtain from Eqs. (3.12) and (3.14) the final result

$$\sum_{m=1}^{N} \left\| \tau_{ex} - \tau^{(m)} \right\|_{V^{(m)}} \leq c h^2 \qquad (3.15)$$

where the constant c used here is independent of h but depends on the exact solution τ_{ex}.

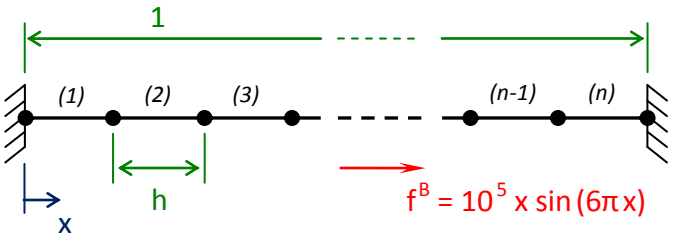

(a)

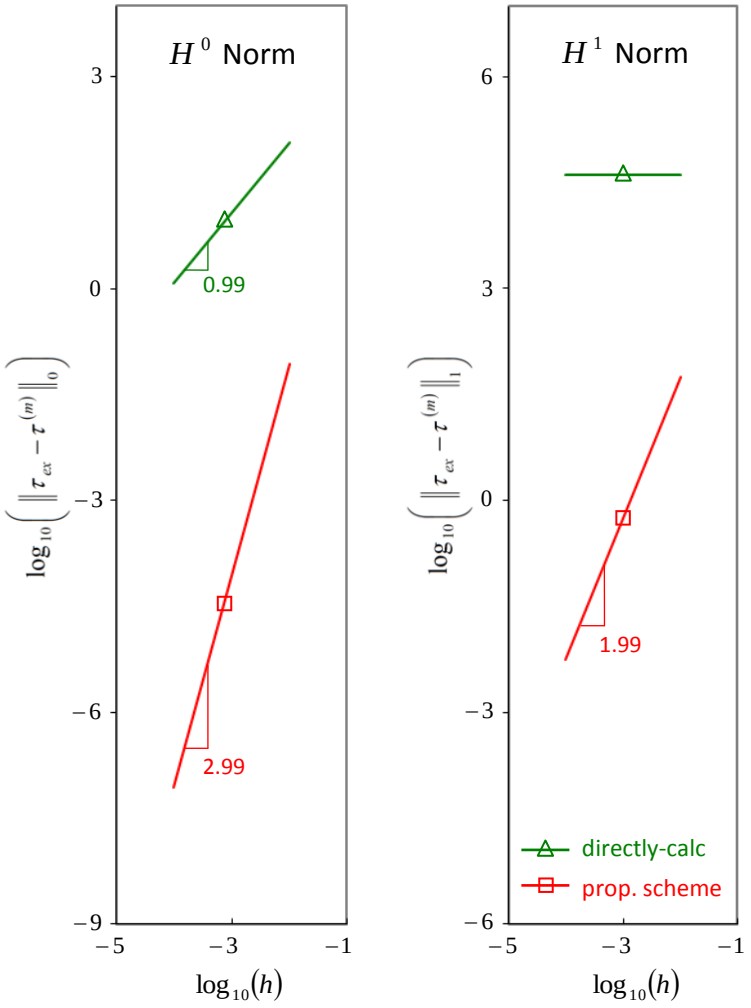

(b)

Fig. 3.1: *Ad-hoc test problem to assess the performance of the proposed scheme in 1D solutions ($E=110\times10^9$, $A=1\times10^{-4}$): (a) the test problem and (b) stress convergence curves measured in the Sobolev norm $\|\cdot\|_k$ of order k*

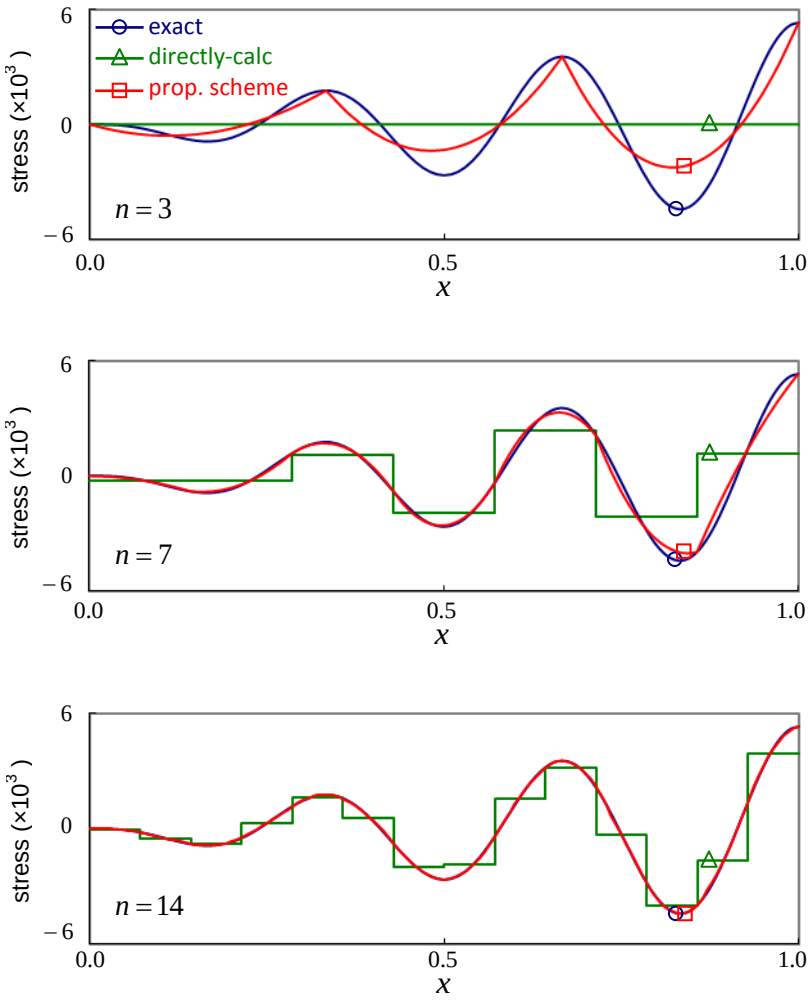

Fig. 3.2: *Stress solutions to the 1D problem defined in Fig. 3.1a for various different densities of mesh, where* n *denotes the number of elements used*

Therefore, $\tau^{(m)}$ converges to the exact theory of elasticity solution with order $O\left(h^2\right)$ in the H^1 norm. In problems where the nodal point displacements are the exact displacements, it follows from Eq. (3.15) that $\tau^{(m)}$ converges at $O\left(h^3\right)$ in the H^0 norm. However, if the nodal point displacements are not the exact displacements, the accuracy of $\tau^{(m)}$ is limited by that of $u^{(m)}$; hence, the highest

order of convergence of $\tau^{(m)}$ that we can expect is $O\left(h^2\right)$ when measured in the H^0 norm.

Of course, these derivations represent theoretical results; however, experience shows this indeed closely represents the actual behaviour of the discretisations. *Fig. 3.1* and *Fig. 3.2* shows the results of an application in which the nodal point displacements are the exact displacements; see ref. [1]. In *Fig. 3.1*, we see that the order of convergence of the enhanced stress is 2.99 in the H^0 norm and 1.99 in the H^1 norm, which compares well with the theoretical result. We further observe in *Fig. 3.2* that when $n=3$, the directly-calculated stress is zero at every point in the domain (as discussed by Grätsch and Bathe [8] and Hiller and Bathe [22]), but the enhanced stress is still quite reasonable.

Fig. 3.3 shows the results of an application in which the nodal point displacements are not the exact displacements. As expected, in this case, $\tau^{(m)}$ converges at $O\left(h^2\right)$ in the H^0 norm, the same as for $u^{(m)}$, but one order higher than that observed for $\tau_h^{(m)}$.

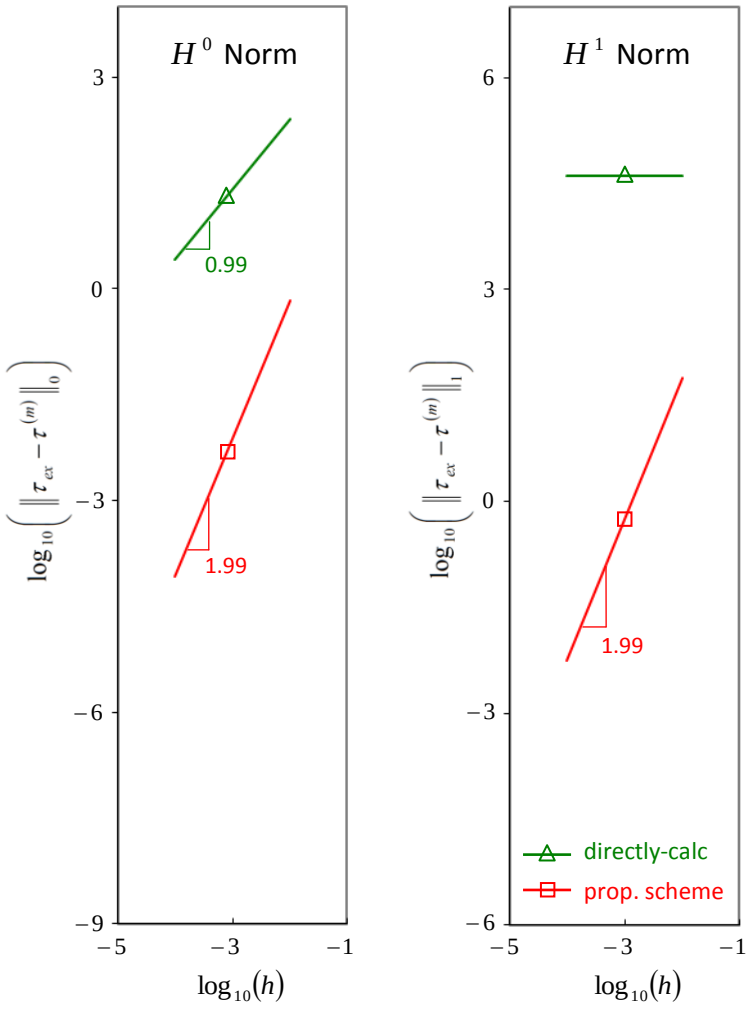

Fig. 3.3: *Stress convergence curves measured in the Sobolev norm* $\|\cdot\|_k$ *of order* k *to the 1D problem defined in Fig. 3.1a, where, in this case, the Young's modulus varies as* $E = 110\left(1+0.64\sin\left(20\pi x\right)\right)\times 10^9$

3.5 Numerical example: a rotor blade problem

To illustrate the effectiveness of the new method, the response of a rotor blade is studied. *Fig. 3.4* defines the problem. The inboard end of the rotor blade is driven at a constant angular velocity ω; the outboard end is either left free or is welded to

a rigid hoop. The rotor blade is idealised as an assemblage of two 2-node truss elements, and the problem is solved using both the usual displacement-based method and the proposed scheme.

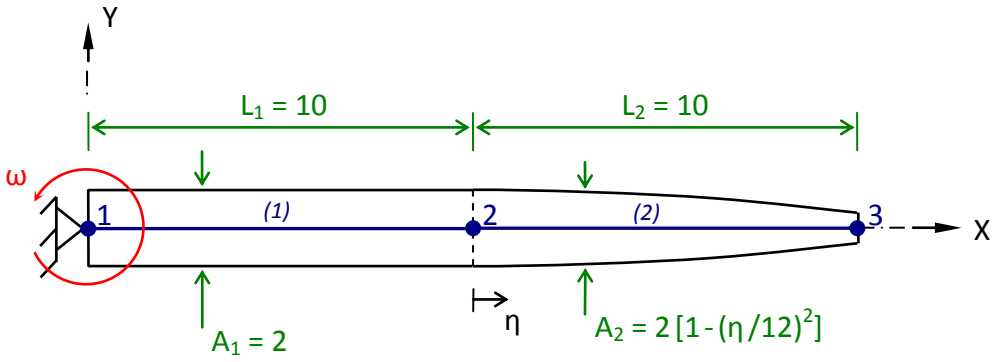

Fig. 3.4: *Rotor blade problem ($E = 110 \times 10^9$, $\rho = 4400$, and $\omega = 10$). The rotor blade spins at a sufficiently high rate that gravitational forces are negligible as compared with the centrifugal forces which act on the blade. The blade is either pinned at node 1 and is free at node 3 ($\hat{U}_1 = 0$ and $\hat{U}_3 \neq 0$), or is pinned at node 1 and is welded to a rigid hoop at node 3 ($\hat{U}_1 = \hat{U}_3 = 0$)*

In this problem, one element has a constant cross-sectional area and the other element has a varying area, as shown in *Fig. 3.4*. We note that the varying area enters in the equilibrium equation, so that Eq. (2.13) becomes

$$\int_{L^{(m)}} \delta\zeta^{(m)T} \left\{ \frac{d}{dx}\left(A(x)\,\tau^{(m)} \right) + A(x)\, f_x^B \right\} dx = 0$$

where $L^{(m)}$ is the length and $A(x)$ is the cross-sectional area of element m, of which the latter is a function of x.

Fig. 3.5 shows the stress results. In *Fig. 3.5* (and all other figures), "exact" refers to the exact analytical (or a very accurate numerical) solution of the mathematical

model, "directly-calc" refers to the directly-calculated finite element stresses, and "prop. scheme" refers to the finite element stresses predicted using the proposed stress improvement scheme.

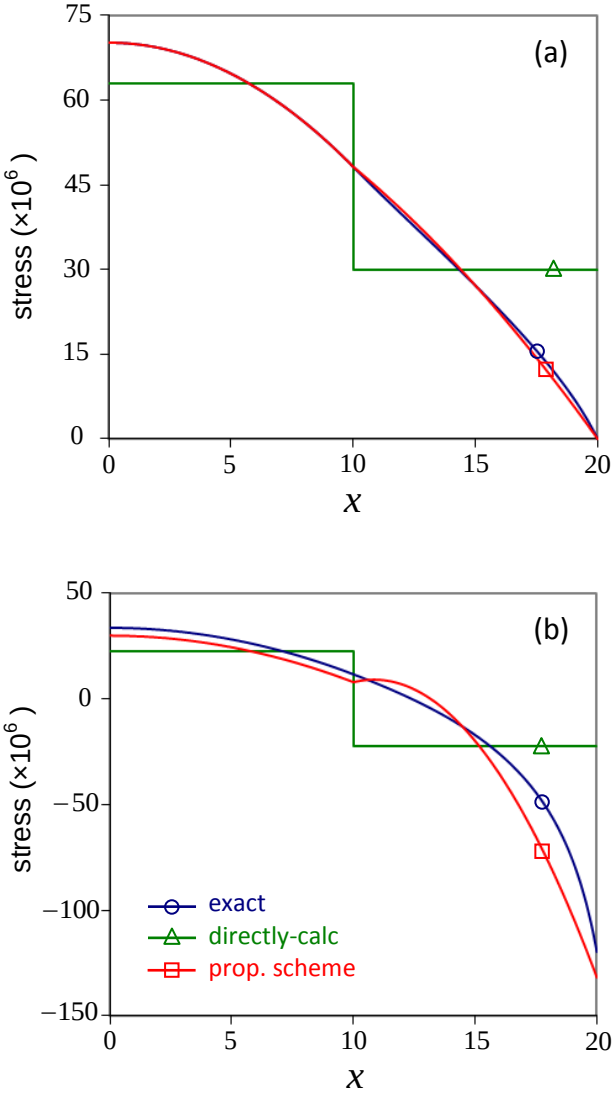

Fig. 3.5: *Stress results for the rotor blade problem defined in Fig. 3.4: (a) the statically determinate pinned-free case ($\hat{U}_1 = 0$ and $\hat{U}_3 \neq 0$), and (b) the statically indeterminate pinned-pinned case ($\hat{U}_1 = \hat{U}_3 = 0$)*

Considering the results, we see that the enhanced solution for the stress is significantly more accurate than given directly by the displacements. We further observe that the gradient of the enhanced stress is exact at every point in element 1. Indeed, this will always be the case when the exact stress varies quadratically across the element domain; see Eq. (3.11).

Next, the rotor blade problem is solved using the PEM [23] and the improved REP method [28]. Typically, the PEM is used to calculate improved interelement tractions for the purposes of error estimation; however, in our comparison the governing equations of the PEM are used to calculate improved stresses.

Fig. 3.6 shows the stress results, where, for consistency, all methods use only one element in the stress calculation domain. We see that the new procedure performs best. This is expected because the new procedure uses a stress with a higher degree of interpolation than can be used with the other methods, and (most importantly) the solution of the new procedure satisfies the properties discussed in section 2.6.1. Also, the assumptions employed in the PEM and the REP method limits the accuracy of the results; see refs. [23], [28] and the earlier discussion in the introduction of the thesis.

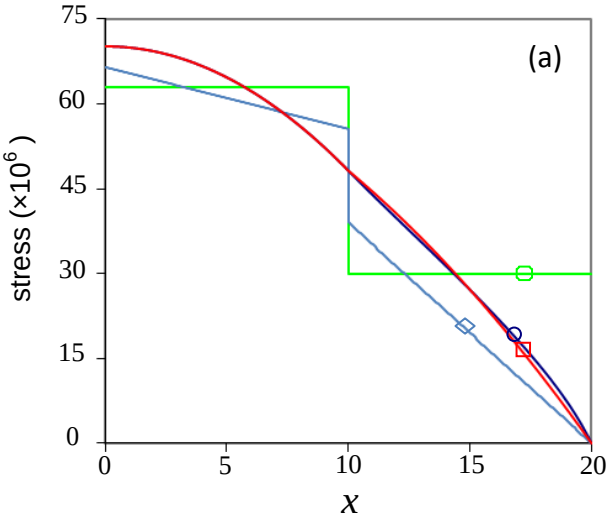

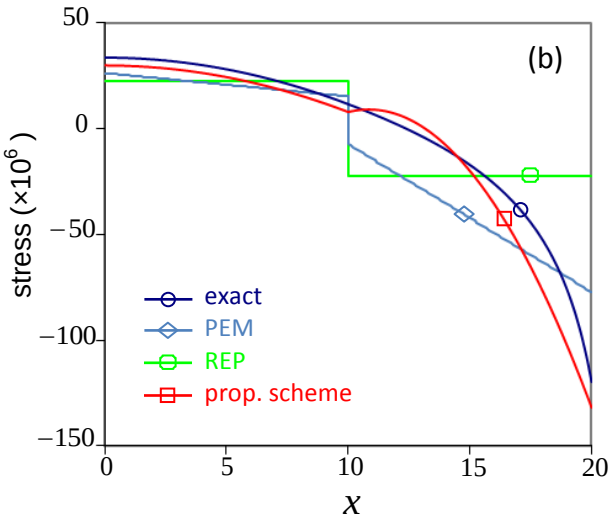

Fig. 3.6: *Stress results for the rotor blade problem defined in Fig. 3.4: (a) the statically determinate pinned-free case ($\hat{U}_1 = 0$ and $\hat{U}_3 \neq 0$), and (b) the statically indeterminate pinned-pinned case ($\hat{U}_1 = \hat{U}_3 = 0$). The PEM assumes a linear stress, the REP method assumes a constant stress, and the proposed scheme assumes a quadratic stress in each element domain*

Lastly, we note that when $\underline{f}^B \in P_1(V)$, the solution obtained using the RCP method is similar to that obtained using the new method (see section 4.4.1); hence, for clarity, we do not consider the RCP results here.

Chapter 4

Insight into the new method in 2D solutions

In this chapter, we first present the solution procedure of the new stress improvement method in 2D settings for a general element m. Then, we discuss how to establish enhanced stresses at a specific node i, and how to deal with discontinuous solutions. Thereafter, we assess the performance of the method in static, dynamic and nonlinear solutions.

Since the performance of the RCP methods exceeds that of the REP method (by a considerable margin) [29], we only compare the stresses of the new procedure with the RCP stresses here.

4.1 Matrices used in 2D solutions

In 2D (and 3D) problems, better results are obtained when multiple elements are used in the stress calculation domain. Hence, to solve for the unknown stress coefficients $\underline{\hat{t}}$ for a general element m, we use the union of elements that

surrounds (and includes) element m as the stress calculation domain; see *Fig. 4.1*. Then, we apply Eq. (2.28) with

$$\underline{\underline{E}}_{\tau} = \left[\begin{array}{cccccc:cccccc:cccccc} 1 & y & z & yz & y^2 & z^2 & 0 & 0 & 0 & 0 & 0 & 0 & 0 & 0 & 0 & 0 & 0 & 0 \\ 0 & 0 & 0 & 0 & 0 & 0 & 1 & y & z & yz & y^2 & z^2 & 0 & 0 & 0 & 0 & 0 & 0 \\ 0 & 0 & 0 & 0 & 0 & 0 & 0 & 0 & 0 & 0 & 0 & 0 & 1 & y & z & yz & y^2 & z^2 \end{array}\right] \quad (4.1)$$

$$\overline{\underline{\underline{E}}}_{\tau} = \left[\begin{array}{ccc:ccc:ccc:ccc} 1 & 0 & 0 & y & z & 2yz & 0 & 0 & 0 & z^2 & 0 & y^2 \\ 0 & 1 & 0 & 0 & 0 & 0 & y & z & 2yz & 0 & y^2 & z^2 \\ 0 & 0 & 1 & -z & 0 & -z^2 & 0 & -y & -y^2 & 0 & 0 & -2yz \end{array}\right] \quad (4.2)$$

$$\underline{\underline{E}}_{\zeta} = \left[\begin{array}{ccc:ccc} 1 & y & z & 0 & 0 & 0 \\ 0 & 0 & 0 & 1 & y & z \end{array}\right] \quad (4.3)$$

and

$$\underline{\underline{\partial}}_{\tau} = \left[\begin{array}{ccc} \dfrac{\partial}{\partial y} & 0 & \dfrac{\partial}{\partial z} \\ 0 & \dfrac{\partial}{\partial z} & \dfrac{\partial}{\partial y} \end{array}\right] \quad (4.4)$$

where $\hat{\underline{\tau}} = \left\{ \alpha_1^{yy} \quad \cdots \quad \alpha_6^{yy} \;\vdots\; \alpha_1^{zz} \quad \cdots \quad \alpha_6^{zz} \;\vdots\; \alpha_1^{yz} \quad \cdots \quad \alpha_6^{yz} \right\}^T$, and (y, z) are the locally based coordinates of the stress calculation domain.

The above description completely defines the stress calculation domain for all types of element and mesh patterns, and no special procedures are needed near the boundaries (nor at the corners) of the mesh. Note that because there is only one possible configuration of stress domain for each element m, the averaging procedure required in refs. [35], [36] is no longer needed.

The RCP method uses the same definition of stress calculation domain [30].

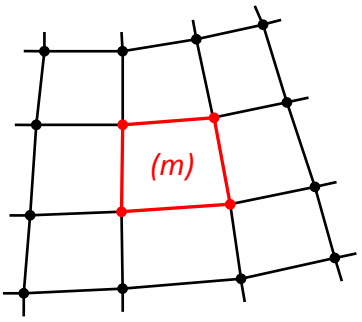

(a) Interior element

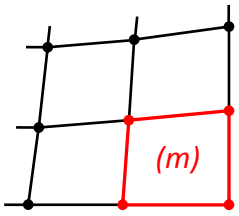

(b) Corner element

Fig. 4.1: *Stress calculation domain used to solve for the unknown stress coefficients* $\hat{\underline{\tau}}$ *for a general 4-node 2D element* m

4.2 Solution procedure for a specific node *i*

For certain problems, we are interested in the stresses at a specific node i, rather than within the element domain. In this situation, we use the union of elements connected to node i as the stress calculation domain. Then, we apply Eq. (2.28) to solve for the unknown stress coefficients, with the interpolation matrices given in Eqs. (4.1) to (4.3).

In the exceptional case where only one element m is connected to node i (e.g. in a corner of the meshed geometry), the elements properly connected to element m should also be included in the stress domain; see *Fig. 4.2*.

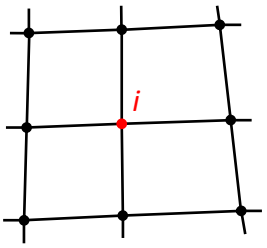

(a) Interior node

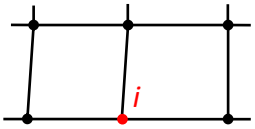

(b) Boundary node

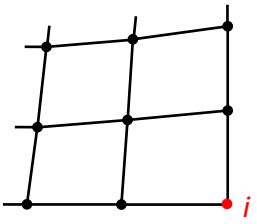

(c) Corner node

Fig. 4.2: *Stress calculation domain used to solve for the unknown stress coefficients* $\underline{\hat{\tau}}$ *at a specific node* i *for a 4-node 2D element mesh*

4.3 Dealing with discontinuous solutions

In an actual implementation, the stress calculation domain only contains elements with equal settings. Boundaries between the element groups are treated as free boundaries; see for example *Fig. 4.3*. This prevents the scheme from smoothing discontinuities present in the exact solution.

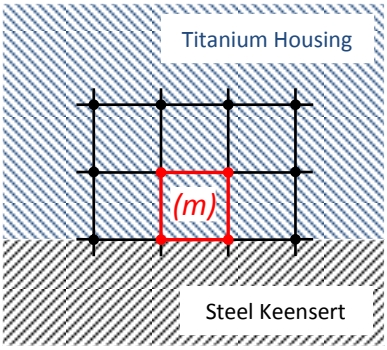

Fig. 4.3: *Stress calculation domain for a general 4-node 2D element* m *between a titanium housing and a steel Keensert. Element* m *belongs to the titanium housing group of elements. Since the steel Keensert elements are not included in the stress domain, there is no smoothing across the material discontinuity*

4.4 Static analysis problems

Two classes of problems are considered: the first where $\underline{f}^{B} \in P_1$, and the second where $\underline{f}^{B} \notin P_1$. We show that the new stress improvement method gives good results for both classes of problems, whereas the RCP method only performs well when $\underline{f}^{B} \in P_1$.

4.4.1 The actuator problem: a case when $\underline{f}^B \in P_1$

The first problem solution involves an actuator subjected to pressure loading. *Fig. 4.4* defines the problem. The problem is statically indeterminate and is solved using both the new method and the RCP method.

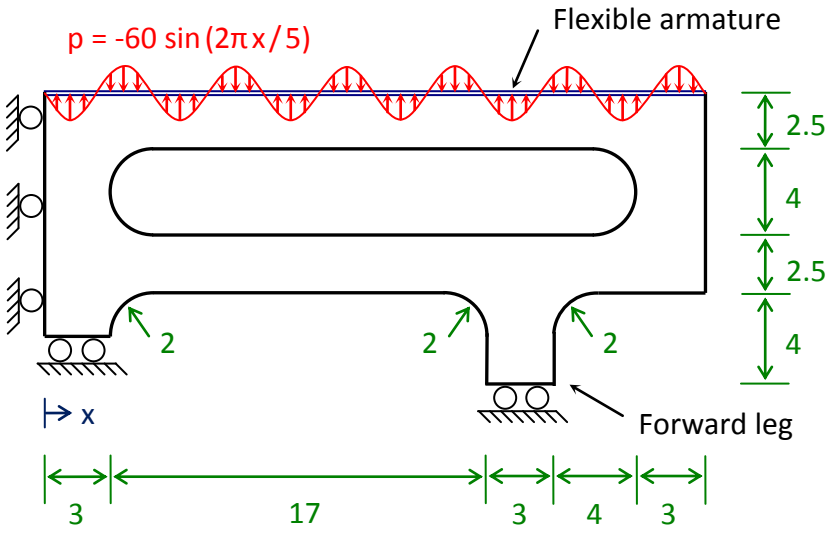

Fig. 4.4: *Actuator subjected to pressure loading problem ($E = 72\times10^3$, $\upsilon = 0.3$, thickness $= 1$, plane stress conditions). The pressure loading is produced by passing current through the armature in the presence of a magnetic field. The armature is flexible as compared to the actuator*

Fig. 4.5 shows the stress convergence curves when a sequence of 3- and 4-node element meshes are used for the solutions. The sequence of meshes is constructed by starting with a mesh of uniform elements of (approximately) equal size, then subdividing each element into four equal new elements to obtain the next (refined) mesh in the sequence, and so on; see *Fig. 4.6*. The mesh size parameter h is calculated by averaging the size of all elements in the assemblage (where the size

is taken to be the diameter of a circle which encompasses that element), and the starting meshes to the convergence curves given in *Fig. 4.5* are shown in *Fig. 4.7*.

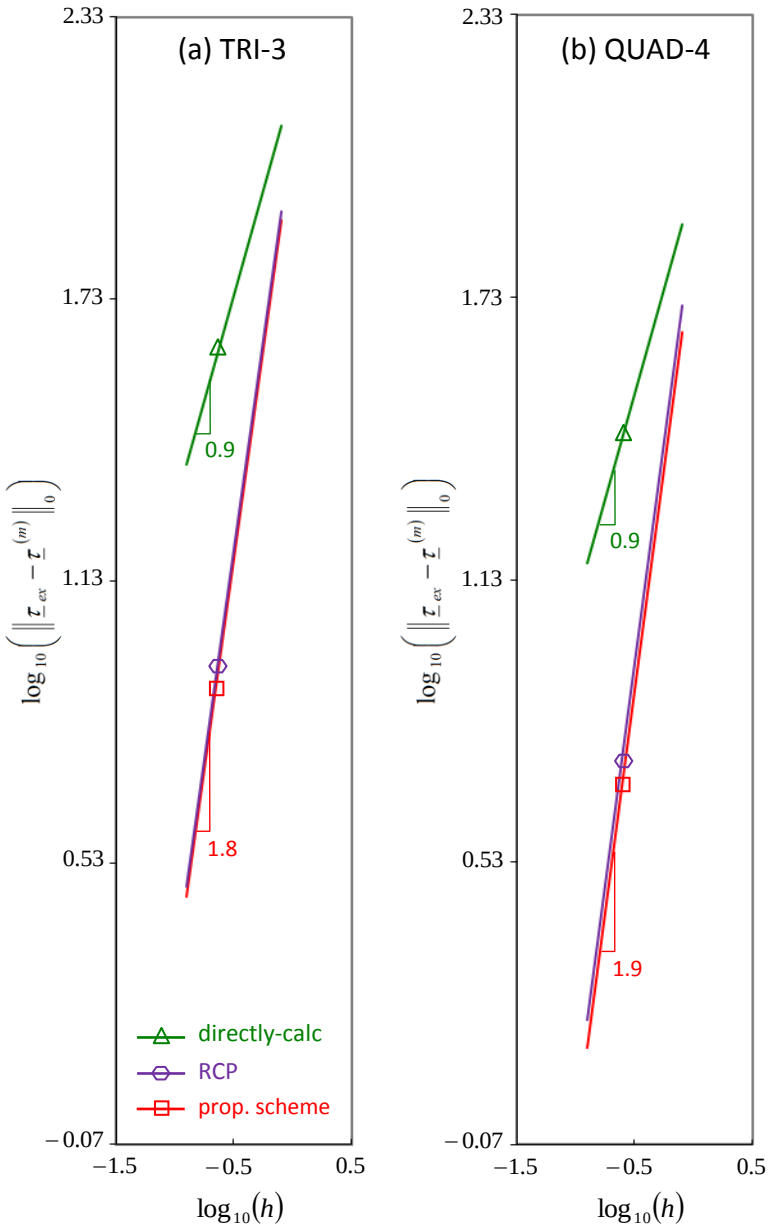

Fig. 4.5: *Stress convergence curves for the actuator problem defined in Fig. 4.4, measured in the* H^0 *norm for: (a) the 3-node triangular and (b) the 4-node quadrilateral element*

Considering the results in *Fig. 4.5*, we see that the RCP solution is similar to the solution obtained using the proposed scheme. This will always be the case when $\underline{f}^{B} \in P_1$, because the quadratically varying stresses are sufficiently rich to satisfy equilibrium point-wise -- that is, Eq. (2.25) reduces to Eq. (2.20) when $\underline{f}^{B} \in P_1$. However, the solutions are not identical due to the Poisson coupling effects in Eq. (2.19).

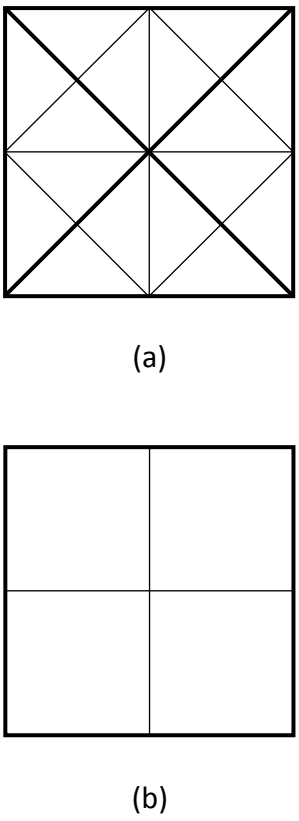

Fig. 4.6: *Refinement sequence used in stress convergence studies. The thick lines depict the initial mesh, and the thinner lines depict the next (refined) mesh in the sequence for: (a) the 3-node triangular and (b) the 4-node quadrilateral element*

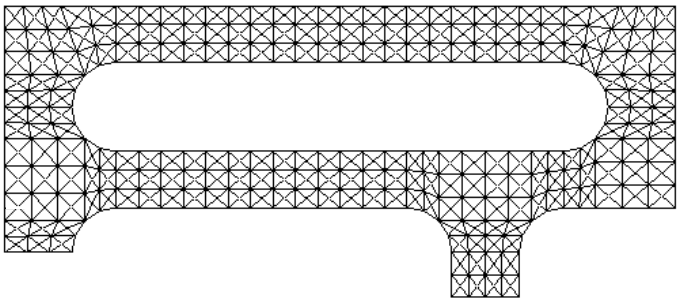

(a)

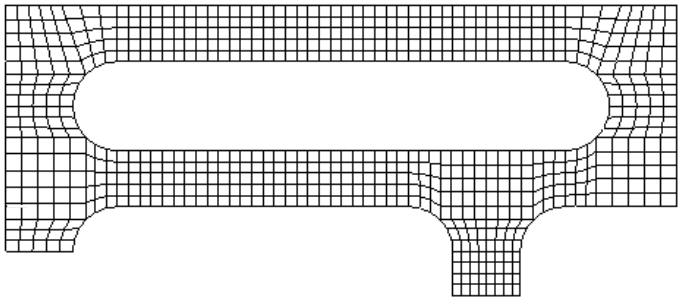

(b)

Fig. 4.7: *Starting meshes for the stress convergence curves given in Fig. 4.5: (a) the 3-node triangular and (b) the 4-node quadrilateral element*

The new procedure can also be used to furnish improved stress predictions for the incompatible modes formulation [1]; see *Fig. 4.8*. In these calculations, the unknown stress coefficients are obtained using Eq. (2.28), where $\underline{\tau}_h^{(m)}$ is established from the incompatible modes solution. This enriches the space implicitly assumed for $\underline{\tau}_h^{(m)}$; however, since $\underline{\tau}^{(m)}$ is assumed quadratically interpolated, the solution is similar, both with and without incompatible modes.

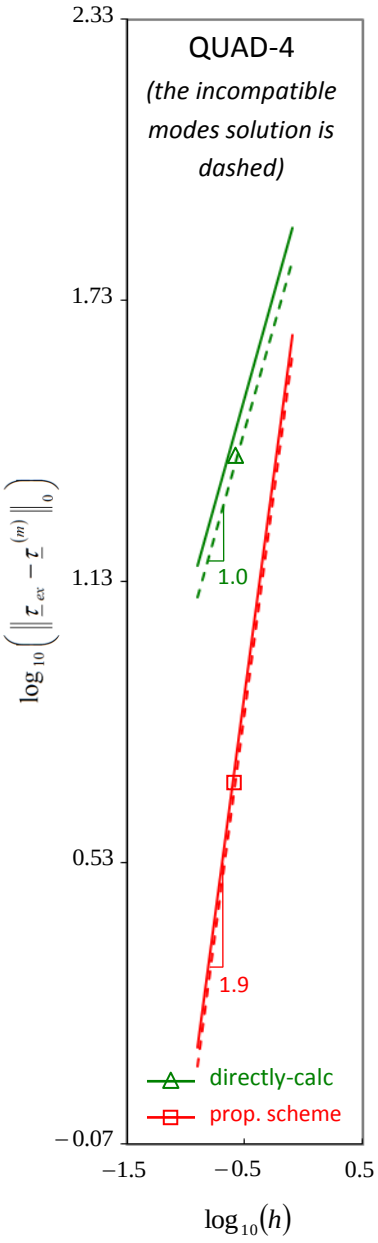

Fig. 4.8: *Stress convergence curves for the actuator problem defined in Fig. 4.4, measured in the* H^0 *norm, for the 4-node quadrilateral element with (dashed line) and without incompatible modes (solid line)*

Mesh 1 (h=0.96)

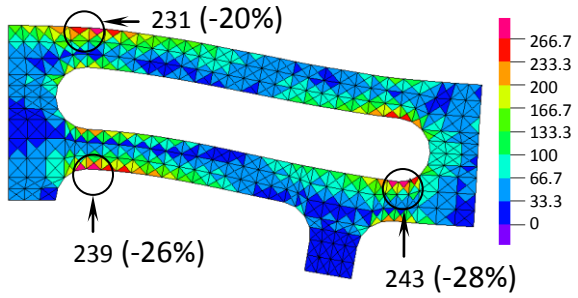

directly-calculated stress

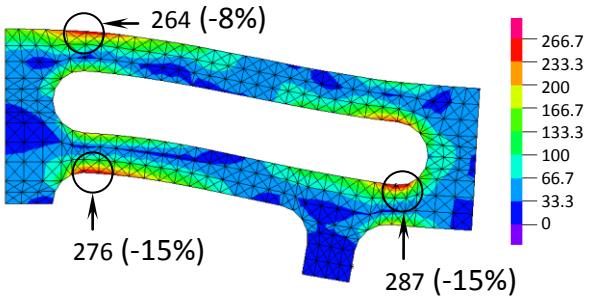

stress of the prop scheme

Mesh 2 (h=0.45)

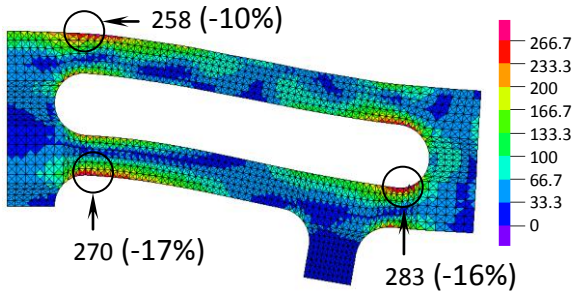

directly-calculated stress

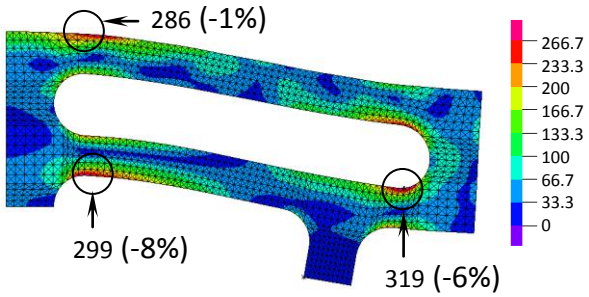

stress of the prop scheme

Mesh 3 (h=0.23)

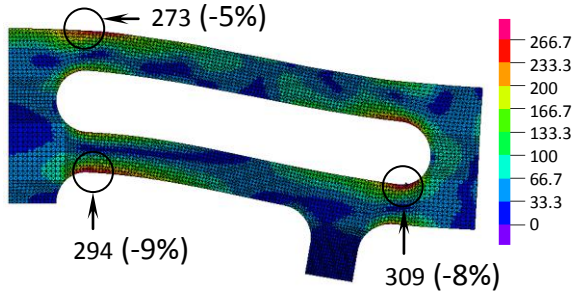

directly-calculated stress

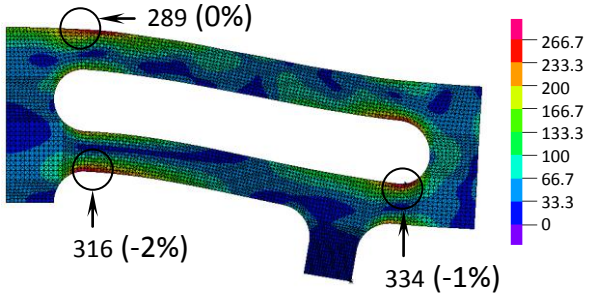

stress of the prop scheme

Fig. 4.9: *von Mises stress band plots for the actuator problem defined in Fig. 4.4, where the forward leg rollers are removed and the material stiffness is reduced by a factor 10. The plate is idealised as an assemblage of 3-node triangular elements. The stress in the band plots is un-averaged (and is shown on the deformed geometry), while the numerical*

stress values are the averaged nodal point stresses with the solution error given in parentheses

Next, consider the situation where the rollers supporting the forward leg are removed and the material stiffness is reduced by a factor of ten. This requires a large deformation solution. *Fig. 4.9* shows the von Mises stress results for three different meshes (plotted on the deformed geometry). As is clear from this figure, the procedure performs well in the large displacement analysis, and significantly enhances the stress prediction. Indeed, we see the enhanced stresses $\underline{\tau}^{(m)}$ are more accurate than the directly-calculated stresses $\underline{\tau}_h^{(m)}$, even when four times more elements are used to calculate $\underline{\tau}_h^{(m)}$ (i.e. $\underline{\tau}^{(m)}$ of Mesh 1 is more accurate than $\underline{\tau}_h^{(m)}$ of Mesh 2, etc.).

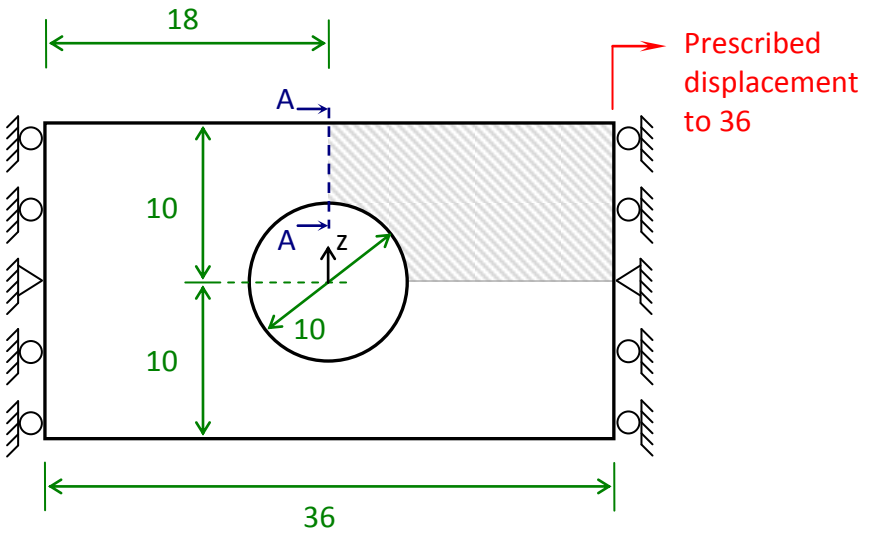

Fig. 4.10: *Large displacement, large strain, rubber plate problem, stretched to 100% of its original length (Ogden material law:* $\mu_1 = 0.7$, $\mu_2 = -0.3$, $\mu_3 = 0.01$, $\alpha_1 = 1.8$, $\alpha_2 = -1.6$, $\alpha_3 = 7.5$, $\kappa = 1000$, *thickness* $= 0.5$, *plane stress conditions). Because of symmetry, only one-quarter of the plate is modelled*

Finally, we solve a large displacement, large strain problem, which includes nonlinear material effects. *Fig. 4.10* defines the problem. The rubber plate is stretched to 100% of its original length by imposing a uniform horizontal displacement at the right end. *Fig. 4.11* and *Fig. 4.12* show the von Mises stress results. As expected, the stresses are considerably improved, especially in those regions of high stress gradients, which, of course, is due to the fact that the directly-calculated stresses are constant for the 3-node finite element. Indeed, in *Fig. 4.12*, we show that the stresses of the new scheme (calculated using 3-node elements) are comparable to those given directly by the displacements of a 6-node element mesh.

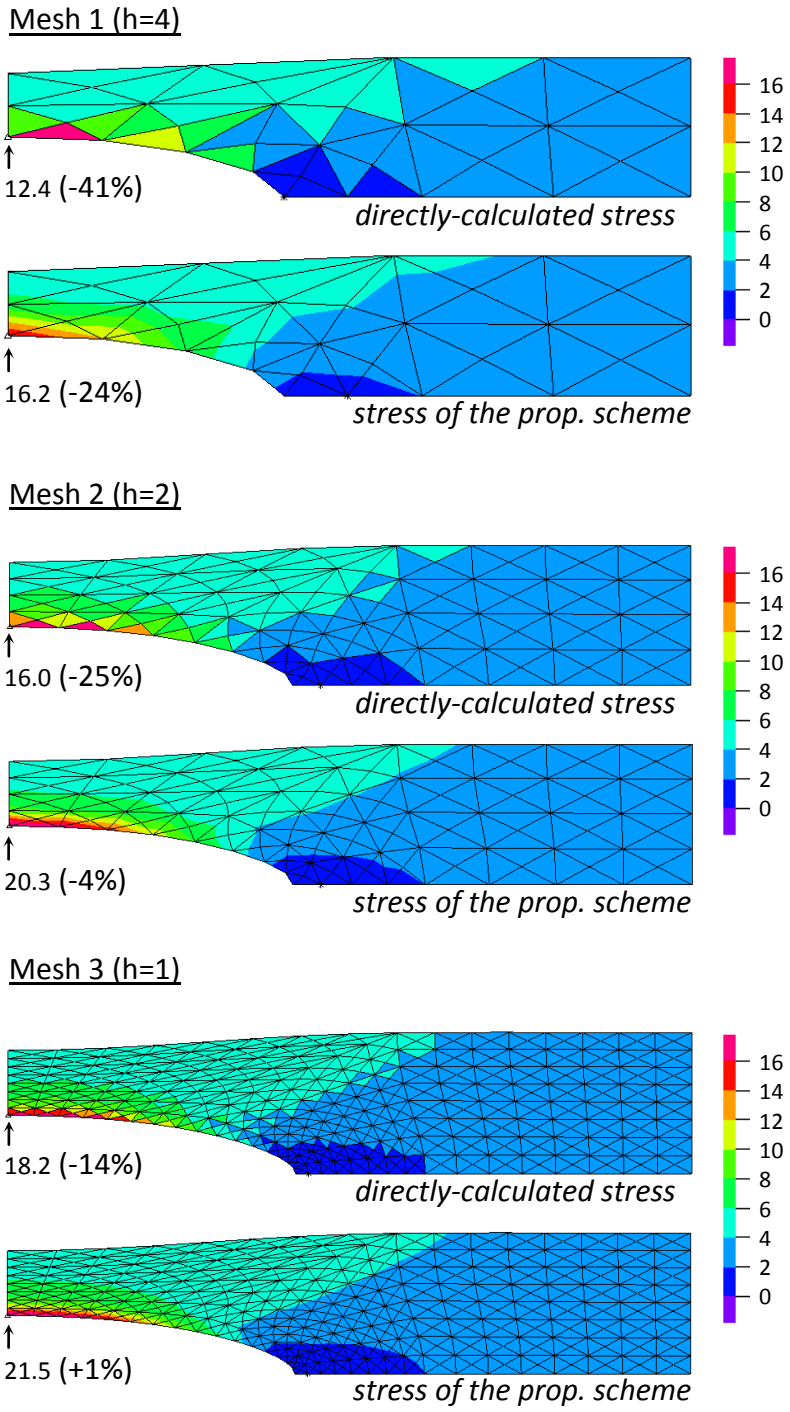

Fig. 4.11: *von Mises stress band plots to the rubber plate problem defined in Fig. 4.10. The plate is idealised as an assemblage of 3-node triangular elements, and the results are shown in the same format as in Fig. 4.9*

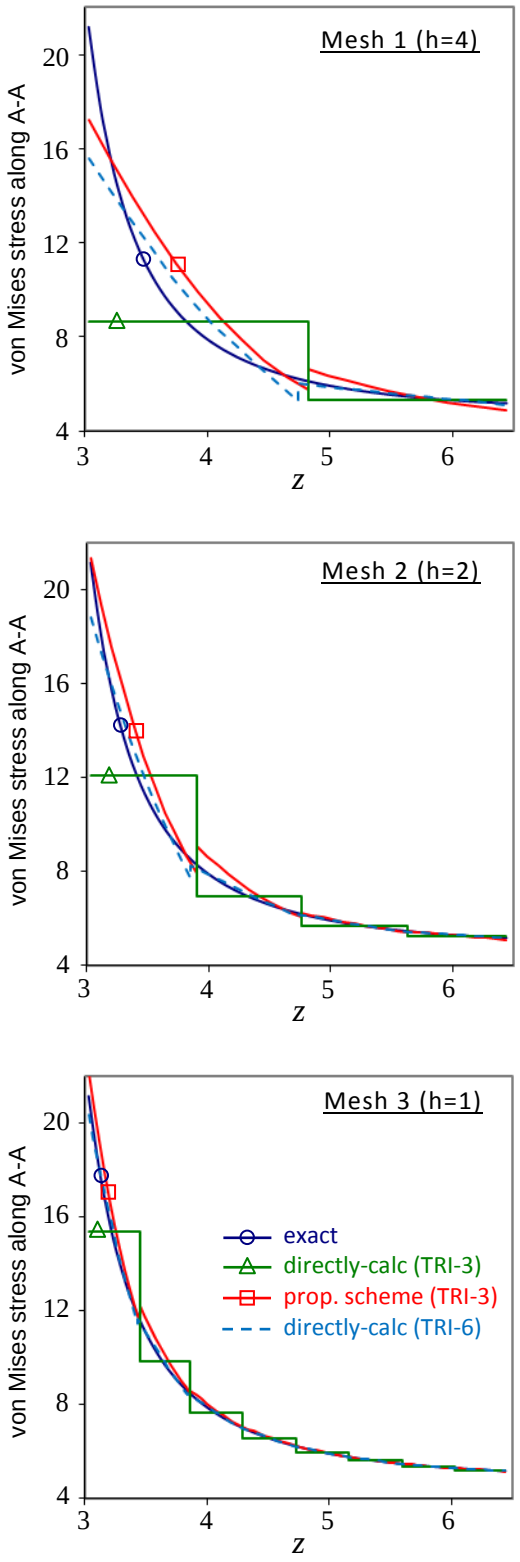

Fig. 4.12: *von Mises stress results to the rubber plate problem defined in Fig. 4.10, along section A-A. The coordinate z references the deformed geometry*

4.4.2 The armature problem: a case when $\underline{f}^{B} \notin P_1$

In this problem solution, the static response of an armature in a magnetic field is studied. *Fig. 4.13* defines the problem. We wish to establish the stresses in the armature due to the Lorentz force. The problem is solved using both the new method and the RCP method.

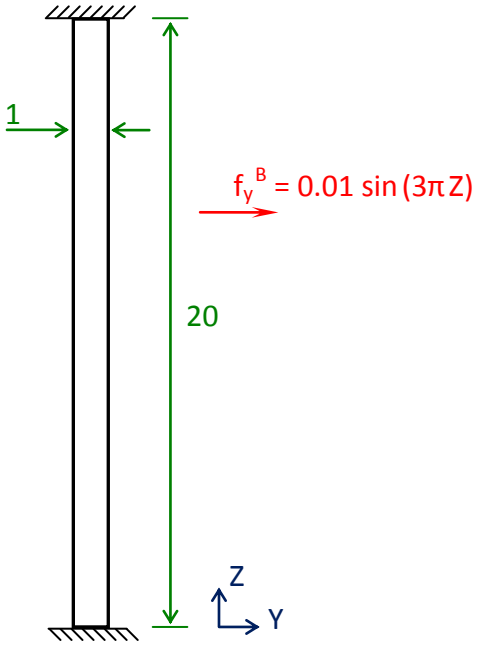

Fig. 4.13: *Armature in a magnetic field problem ($E = 72\times10^3$, $\upsilon = 0$, thickness $= 1$, plane stress conditions). A battery drives constant (direct) current through the armature, and the moving charges experience a Lorentz force in the presence of the magnetic field. The Lorentz force is modelled as a body force f_Y^B. We use $\upsilon = 0$ to avoid stress singularities at the four corners*

Fig. 4.14 shows the stress convergence curves when a 5×100 starting mesh is used. We see that the new method performs well, but the RCP method gives stresses that are *less* accurate than $\underline{\tau}_h^{(m)}$ for coarse meshes.

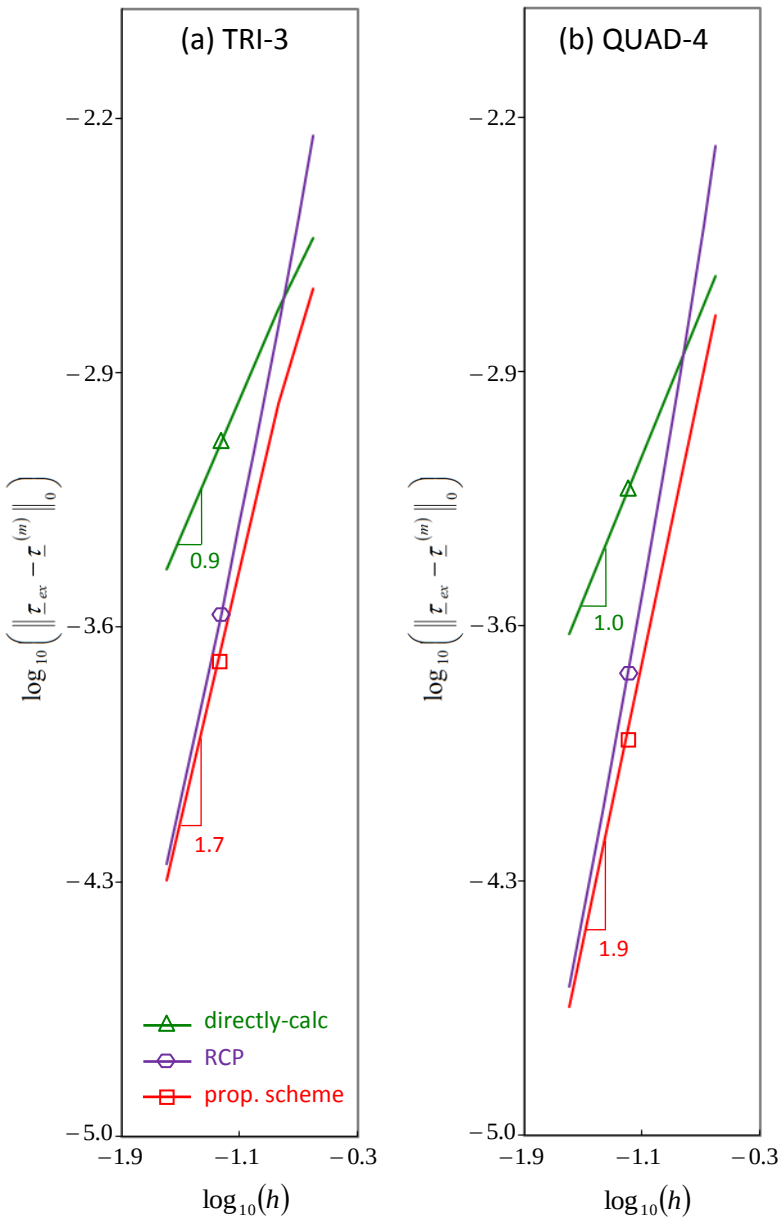

Fig. 4.14: *Stress convergence curves for the armature problem defined in Fig. 4.13, measured in the* H^0 *norm for: (a) the 3-node triangular and (b) the 4-node quadrilateral element*

The reason that the RCP method gives inaccurate results is that the equilibrium constraint in Eq. (2.20) is too severe when $\underline{f}^{B} \notin P_1$. Indeed, to satisfy differential equilibrium, the RCP method uses the following additive decomposition:

$$\underline{\tau}^{(m)} = \underline{\tau}_{h.s.}^{(m)} + \underline{\tau}_{p.s.}^{(m)} \tag{4.5}$$

where $\underline{\tau}_{h.s.}^{(m)}$ is the unknown homogenous solution of Eq. (2.20), and $\underline{\tau}_{p.s.}^{(m)}$ is a particular solution of the same equation, to be established *a priori* [29], [30].

The homogenous solution $\underline{\tau}_{h.s.}^{(m)}$ is assumed to be an element in the subspace of self-equilibrated stresses in P_2 -- that is, $\underline{\tau}_{h.s.}^{(m)} \in \overline{\nabla}^{\tau}$, where $\overline{\nabla}^{\tau}$ is defined in Eq. (2.26) -- and the unknown stress coefficients in $\underline{\tau}_{h.s.}^{(m)}$ are obtained using Eq. (2.19),

$$\begin{aligned} \sum_{m=1}^{N_P} \left(\int_{V^{(m)}} \delta \underline{\bar{\tau}}^{(m)T} \, \underline{C}^{(m)-1} \, \underline{\tau}_{h.s.}^{(m)} \, dV \right) \\ = \sum_{m=1}^{N_P} \left(\int_{V^{(m)}} \delta \underline{\bar{\tau}}^{(m)T} \left\{ \underline{\varepsilon}^{(m)} - \underline{C}^{(m)-1} \, \underline{\tau}_{p.s.}^{(m)} \right\} dV \right) \end{aligned} \tag{4.6}$$

with the particular solution $\underline{\tau}_{p.s.}^{(m)}$ taken as:

$$\underline{\tau}_{p.s.}^{(m)} = \left\{ \tau_{p.s.}^{yy(m)} \quad \tau_{p.s.}^{zz(m)} \quad \tau_{p.s.}^{yz(m)} \right\}^T$$

$$\tau_{p.s.}^{yy(m)} = -\int_0^y f_y^B \, dy, \quad \tau_{p.s.}^{zz(m)} = -\int_0^z f_z^B \, dz, \quad \tau_{p.s.}^{yz(m)} = 0$$

Therefore, the dimension of $\underline{\tau}_{p.s.}^{(m)}$ depends on $\underline{f}^{B}$, and the components in Eq. (4.5) are mismatched when $\underline{f}^{B} \notin P_1$. As a result, the RCP method is unreliable when

$\underline{f}^{B} \notin P_1$ -- e.g. in problems with electromagnetic forces, piezoelectric forces [49], etc. -- and gives inaccurate results.

4.5 Dynamic analysis problems

Our objective in this section is to assess the performance of the new method and the RCP method in solving dynamic analysis problems. We show that the new method performs well in dynamic analysis and can be used for distorted isoparametric elements, whereas the RCP method can only be used if the elements in the assemblage are un-distorted.

4.5.1 Solution procedure

Stress calculations in dynamics are performed as those in statics, except now the d'Alembert inertia forces are included in $\underline{f}^{B}$. That is, to obtain the stress coefficients ${}^{t}\underline{\hat{\tau}}$ of the new method at time t, we use

$$\left[\sum_{m=1}^{N_P}\begin{pmatrix}\int_{V^{(m)}} \underline{\overline{E}}_{\tau}^{T}\,\underline{E}_{\tau}\,dV \\ \int_{V^{(m)}} \underline{E}_{\zeta}^{T}\,\underline{\partial}_{\tau}\,\underline{E}_{\tau}\,dV\end{pmatrix}\right]{}^{t}\underline{\hat{\tau}} = \left\{\sum_{m=1}^{N_P}\begin{pmatrix}\int_{V^{(m)}} \underline{\overline{E}}_{\tau}^{T}\,{}^{t}\underline{\tau}_{h}^{(m)}\,dV \\ \int_{V^{(m)}} \underline{E}_{\zeta}^{T}\left\{\rho^{(m)}\,\underline{H}^{(m)}\,{}^{t}\ddot{\underline{U}} - {}^{t}\underline{f}^{B}\right\}dV\end{pmatrix}\right\} \qquad (4.7)$$

where $\rho^{(m)}$ is the mass density of element m, ${}^{t}\ddot{\underline{\hat{U}}}$ lists the nodal point accelerations (i.e. the second time derivative of ${}^{t}\underline{\hat{U}}$), and the nodal solutions are established using a time integration scheme [1]. In our examples, we use the Bathe implicit time integration procedure because spurious oscillations are very small [51] to [53]. *Fig. 4.15* gives an example solution where, for the mesh used, we give the best results obtained by the Newmark method (trapezoidal rule) and the Bathe method when changing for each method the time step size (i.e. the CFL number).

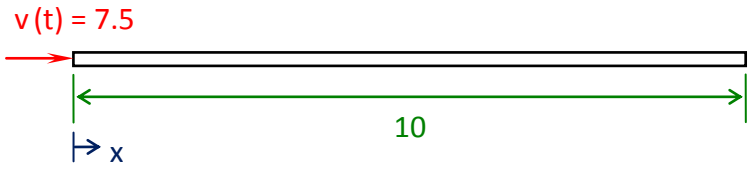

(a) Problem solved

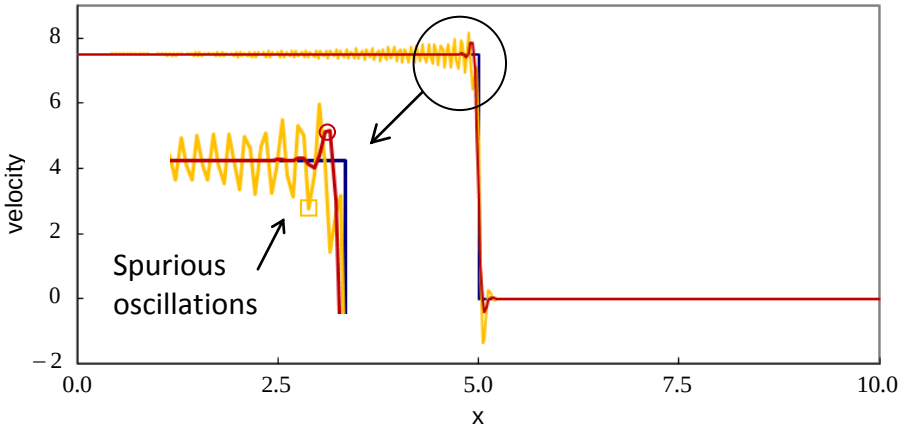

(b) Velocity

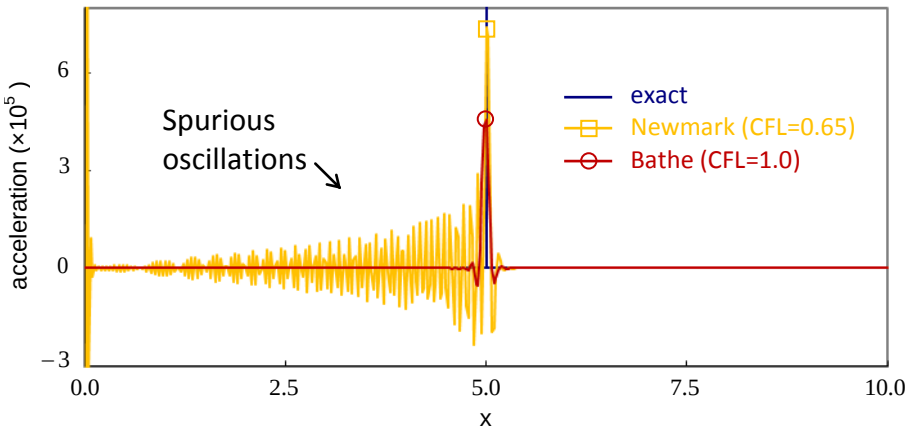

(c) Acceleration

Fig. 4.15: *Impact of an elastic bar ($E = 200\times10^9$, $\rho = 8000$, $A = 1$). The bar is initially at rest, and the response at time $t = 1\times10^{-3}$ is sought. During this time the wave propagates to $x = 5$, there are no reflections. The bar is idealised as an assemblage of 1D 2-node elements of size $h = 0.025$ (400 elements). We give the best results obtained using the Newmark method and the Bathe method when changing for each method the time step size (i.e. the CFL number)*

To obtain the RCP stresses, we use Eqs. (4.5) and (4.6), with the particular solution taken as:

$$ {}^t\underline{\tau}^{(m)}_{p.s.} = \left\{ {}^t\tau^{yy(m)}_{p.s.} \quad {}^t\tau^{zz(m)}_{p.s.} \quad {}^t\tau^{yz(m)}_{p.s.} \right\}^T $$

$$ {}^t\tau^{yy(m)}_{p.s.} = \int_0^y \left(\rho^{(m)} \, {}^t\underline{\ddot{u}}^{(m)}_y - {}^tf^B_y \right) dy, \qquad {}^t\tau^{zz(m)}_{p.s.} = \int_0^z \left(\rho^{(m)} \, {}^t\underline{\ddot{u}}^{(m)}_z - {}^tf^B_z \right) dz, \qquad {}^t\tau^{yz(m)}_{p.s.} = 0 $$

where ${}^t\underline{\ddot{u}}^{(m)} = \left[{}^t\underline{\ddot{u}}^{(m)}_y , {}^t\underline{\ddot{u}}^{(m)}_z \right]^T = \underline{H}^{(m)} \, {}^t\underline{\ddot{\hat{U}}}$; however, establishing this particular solution for distorted isoparametric elements is difficult and an outstanding issue to be solved.

4.5.2 Numerical examples

The first problem solution involves the propagation response of a wave in an elastic bar. *Fig. 4.16* defines the problem. While solved using 2D meshes, due to the geometry and the material definition, this is effectively a 1D wave solution. The problem is solved using both the new method and the RCP method.

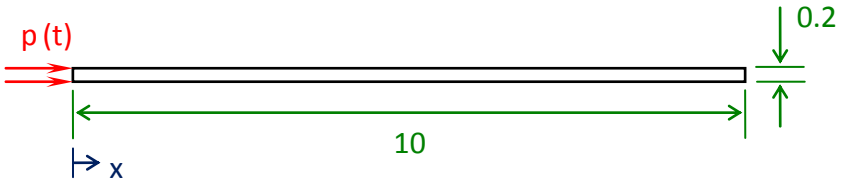

(a) Physical structure

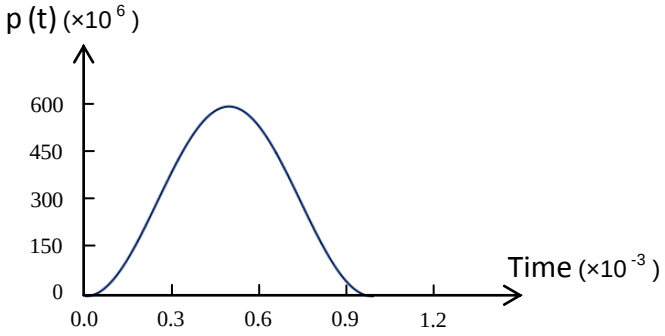

(b) Time variation of pressure

Fig. 4.16: *Propagation of a wave in an elastic bar problem ($E = 200\times10^9$, $\rho = 7800$, $\upsilon = 0$, thickness $= 0.2$, plane stress conditions). The bar is initially at rest, and is subjected to a sudden pressure load at one end. The response at time $t = 0.001284$ is sought. During this time the wave propagates to $x = 6.5$, there are no reflections*

Fig. 4.17 shows the stress results at time $t = 0.001284$; as is clear from this figure, both the new method and the RCP method gives good results.

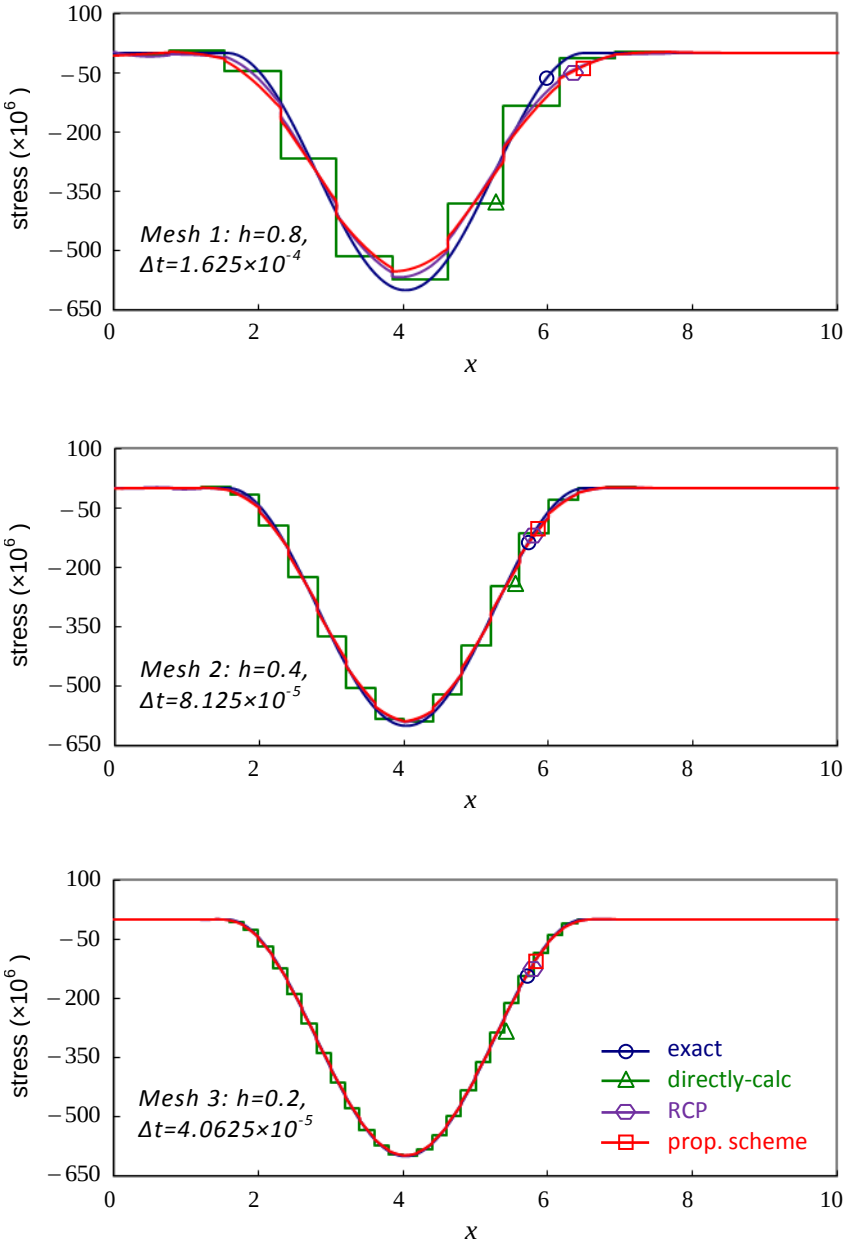

Fig. 4.17: *Longitudinal stress results at* $t = 0.001284$ *to the wave propagation problem defined in Fig. 4.16, using* 40 *time steps. The bar is idealised as an assemblage of regular 4-node quadrilateral elements, where* h *denotes the element size and* Δt *is the time step used. In each case, the CFL number =1*

We note that if spurious oscillations are present in the calculated response, the new method outperforms the RCP method. The reason is that the differential

equilibrium constraint in Eq. (2.20) is too severe when the calculated accelerations vary significantly over the stress calculation domain.

In the second problem solution, a lightweight cantilevered plate subjected to base excitation is studied. *Fig. 4.18* defines the problem. The problem is solved using the new procedure. The RCP method cannot be used, since the elements in the assemblage are distorted.

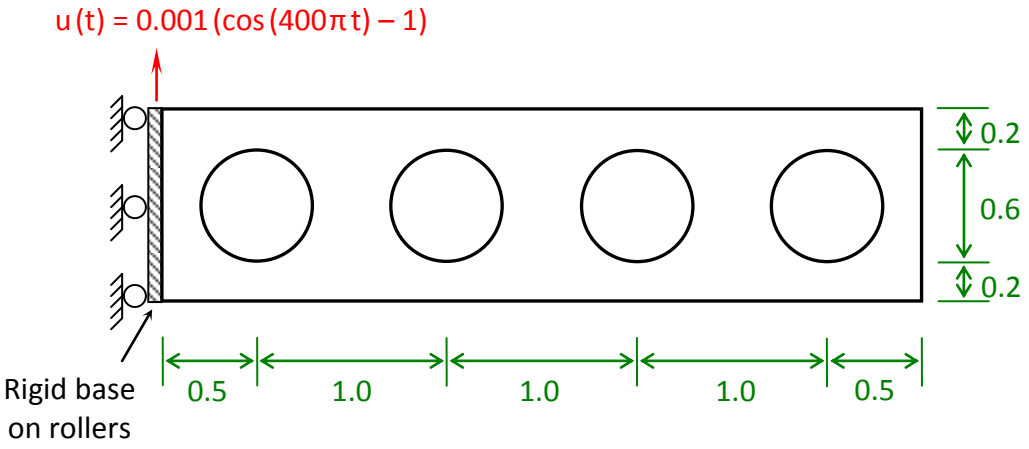

Fig. 4.18: *Lightweight cantilevered plate subjected to base excitation problem* ($E = 200 \times 10^9$, $\rho = 7800$, $\upsilon = 0$, *thickness* $= 1$, *plane stress conditions). The plate is initially at rest, and the response at* $t = 0.01902$ *is sought. No physical damping is introduced in the model. The base of the plate is rigid, and the enforced displacement dynamically excites the first eight natural modes of the plate. We use* $\upsilon = 0$ *to avoid stress singularities at the two corners of the built-in end*

Fig. 4.19 and *Fig. 4.20*, respectively, show the von Mises band plots and the stress convergence curves at time $t = 0.01902$. We see that the enhanced stresses are significantly more accurate than the directly-calculated values, both for the 3-node triangular and the 4-node quadrilateral element, and converge at order $O\left(h^2\right)$.

Mesh 1 (h=0.105)

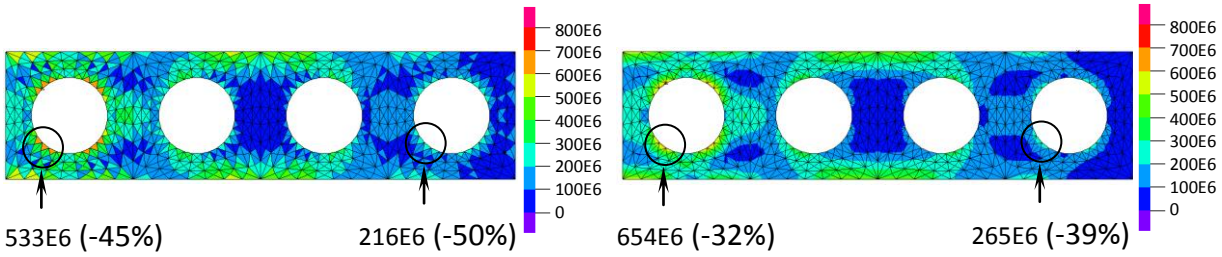

directly-calculated stress *stress of the prop scheme*

Mesh 2 (h=0.075)

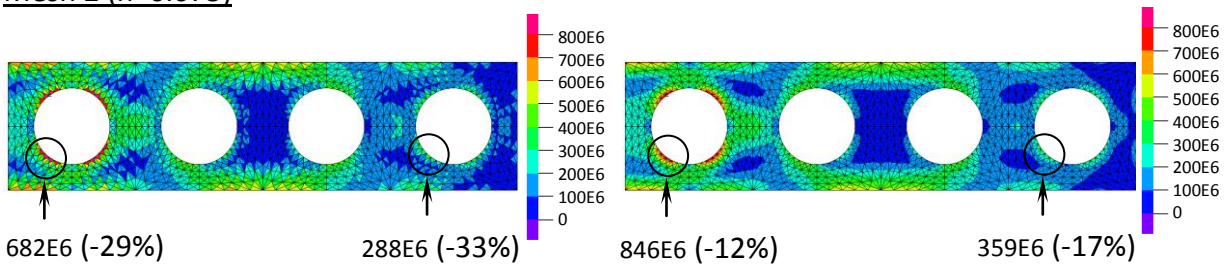

directly-calculated stress *stress of the prop scheme*

Mesh 3 (h=0.037)

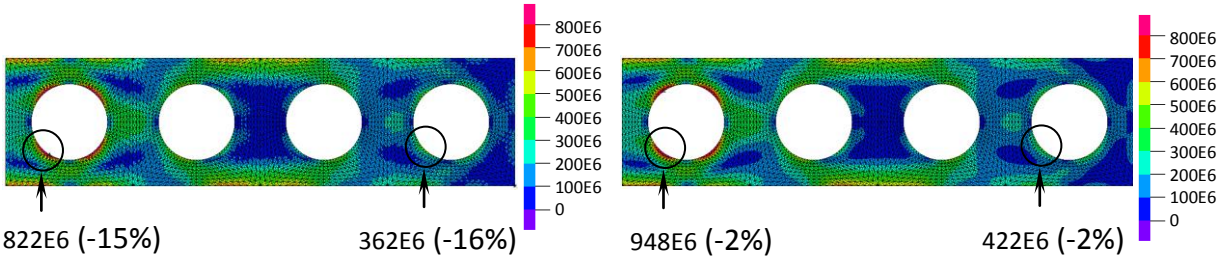

directly-calculated stress *stress of the prop scheme*

Fig. 4.19: *von Mises stress band plots at* $t = 0.01902$ *to the lightweight cantilevered plate problem defined in Fig. 4.18, using* 152 *time steps. The plate is idealised as an assemblage of 3-node triangular elements. The results are shown in the same format as in Fig. 4.9*

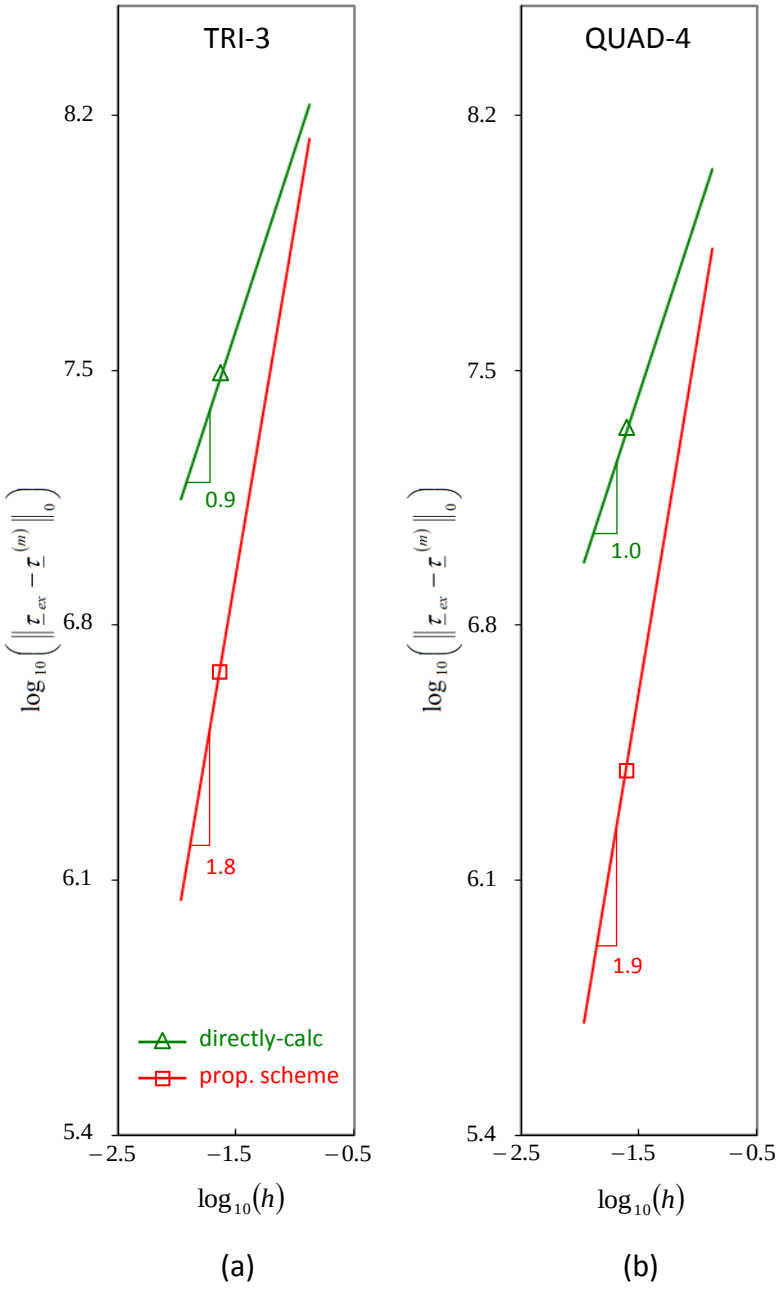

Fig. 4.20: *Stress convergence curves at* $t = 0.01902$ *for the lightweight cantilevered plate problem defined in Fig. 4.18, using* 152 *time steps, measured in the* H^0 *norm for: (a) the 3-node triangular and (b) the 4-node quadrilateral element*

Concluding remarks

The objective of this thesis was to present a general stress improvement method that can be used in static, dynamic and nonlinear solutions. We focused the development on the use of low-order displacement-based elements.

First, we showed that the PEM and the REP, RCP and the NPF-based methods [23] to [36] can all be derived from (or be related to) a mixed formulation, based on the Hu-Washizu principle, where the stress-strain relationship is point-wise relaxed but the fulfilment of equilibrium is enhanced.

This mixed variational formulation gives insight, which we used to develop a new stress improvement scheme.

For 1D problems with arbitrary loading and material properties, but constant cross-sectional area, we proved that the new stress improvement scheme is reliable, giving stresses that are, in fact, optimal stress predictions (in the norm used), with the order of convergence being quadratic, i.e. with the same order as the displacements. This convergence behaviour was also seen numerically in 1D and 2D solutions. Indeed, we obtained excellent numerical results for the 1D and 2D problems solved, with the predicted stresses converging quadratically and with a significant downward shift.

While only 1D and 2D solutions are considered here, in linear and nonlinear analyses, the proposed method is directly applicable to 3D solutions in an analogous way, and similar results can be expected.

Regarding future research, the possibilities to establish solution error estimates [7], [8], and to apply the procedure in shell analyses [2] and in the solution of multiphysics problems [54] might be explored.

Appendix A

The NPF-based method

When considering the finite element solution, two important facts hold, namely, (1) at each node, the sum of the element nodal point forces are in equilibrium with the externally applied nodal point loads, and (2) each element is in force and moment equilibrium under the action of its own nodal point forces -- and, most importantly, these two properties hold for *any* coarseness of mesh -- just as in the analysis of truss and beam structures, see refs. [1] and [14]. For this reason, it seems somewhat natural to use these forces to calculate improved stress predictions, but the details of establishing a general and effective algorithm are far from apparent.

Our objective in this appendix is to present a novel approach to calculate the element stresses using the element nodal point forces. That is, the solution for the element nodal point displacements is performed as usual, the element nodal point forces are calculated as usual, and then a simple procedure is employed to calculate the element stresses from the nodal point forces using the principle of virtual work. Accordingly, we call this procedure the “nodal point force based stress calculation method” or the “NPF-based method” giving “NPF-based stresses”, for short.

To demonstrate the effectiveness of the nodal point force based stress calculation method, we first apply the procedure to the 3- and 4-node two-dimensional continuum solid elements, and solve a number of problems. As expected, we see a significant improvement in the accuracy of the stresses for all problems considered. Then, we apply the procedure to the 4-node three-dimensional tetrahedral elements and solve the same set of problems considered before, but of course this time in three-dimensional settings. Once again, we see a significant improvement for all problems considered. These results are of particular interest, since reliable improvements in stresses for the 4-node tetrahedral element, using incompatible modes or enhanced strains, are difficult to reach in general analyses [41] to [43].

A.1 Using the principle of virtual work

The *nodal point force based stress calculation method* (referred to later as the NPF-based method) uses, as its ingredients, what we shall call the principles of virtual work in the form of boundary tractions and in the form of internal stresses. We review these general and well-known principles in this section, and summarize and focus on some of their powerful properties, see also ref. [1]. In sections A.2 and A.3, we apply these principles -- and their properties -- to establish our simple and effective algorithm for the improved stress predictions, in two- and three-dimensional settings, respectively.

A.1.1 The principle of virtual work in the form of boundary tractions

Consider the equilibrium of a general three-dimensional body of volume V and surface area S. The body is supported on the area S_u with prescribed displacements $\underline{\hat{u}}$, and is subjected to surface tractions $\underline{f}^S$ on the area S_f. In addition, the body is subjected to externally applied body forces $\underline{f}^B$ per unit volume. We assume linear analysis conditions.

In the differential formulation of the problem we seek to calculate the response of the body from the governing differential equations of equilibrium and compatibility, with the constitutive relationships, subject to the applied boundary conditions. That is, we want to solve

$$\begin{aligned} div\left[\underline{\tau}_{ex}\right] + \underline{f}^B &= \underline{0} \\ \underline{\varepsilon}_{ex} &= \underline{\partial}_{\varepsilon}\, \underline{u}_{ex} \\ \underline{\tau}_{ex} &= \underline{C}\, \underline{\varepsilon}_{ex} \end{aligned}$$

subject to

$$\begin{aligned} \underline{u}_{ex} &= \underline{u}_p \quad on\ S_u \\ \underline{f}^S &= \underline{\tau}_{ex}\, \underline{n} \quad on\ S_f \end{aligned}$$

where $\underline{u}_{ex}$, $\underline{\varepsilon}_{ex}$ and $\underline{\tau}_{ex}$ are the exact displacements, strains and stresses, respectively, $\underline{\partial}_{\varepsilon}$ is the differential operator on $\underline{u}_{ex}$ to obtain the strain components $\underline{\varepsilon}_{ex}$, $\underline{C}$ is the stress-strain matrix, and $\underline{n}$ is the unit outward normal vector to the surface S_f.

A second, but entirely equivalent approach to the solution of the problem is given by the variational formulation, that is, the principle of virtual work [1], [2], [38]. This formulation states that for *any* continuous virtual displacement field $\underline{\bar{u}}$, zero on S_u, imposed onto the body in its state of equilibrium, the total internal virtual work is equal to the total external virtual work; that is:

$$\int_V \nabla \underline{\bar{u}} : \underline{\tau}_{ex} \, dV = \int_{S_f} \underline{\bar{u}} \cdot \underline{f}^S \, dS + \int_V \underline{\bar{u}} \cdot \underline{f}^B \, dV \qquad \text{(A.1)}$$

Of course, closed-form analytical solutions to these equations can only be found when relatively simple problems are considered, and so the objective of the finite element method is to establish for complex problems a numerical solution which satisfies the above governing equations as closely as possible. To this end, we assume in the displacement-based finite element method a displacement field within each element m, that is, $\underline{u}^{(m)} = \underline{H}^{(m)} \underline{U}$ where $\underline{H}^{(m)}$ is the displacement interpolation matrix, and $\underline{U}$ contains the nodal point displacements of the assemblage. With this assumption, Eq. (A.1) becomes:

$$\left[\sum_m \int_{V^{(m)}} \underline{B}^{(m)T} \underline{C}^{(m)} \underline{B}^{(m)} \, dV \right] \underline{U} = \sum_m \int_{S_f^{(m)}} \underline{H}^{(m)T} \underline{f}^S \, dS + \sum_m \int_{V^{(m)}} \underline{H}^{(m)T} \underline{f}^B \, dV \qquad \text{(A.2)}$$

where $\underline{B}^{(m)}$, $V^{(m)}$, and $S_f^{(m)}$ are the strain-displacement matrix, the volume, and the surface area with externally applied tractions of element m, respectively, and we sum over all elements in the mesh, see for example ref. [1].

If the body is adequately constrained, the stiffness matrix established from Eq. (A.2) can be factorised to solve for $\underline{U}$, from which the directly-calculated finite

element stress $\underline{\tau}_h^{(m)}$ is determined using the derivatives of the displacement solution

$$\underline{\tau}_h^{(m)} = \underline{C}^{(m)}\,\underline{\varepsilon}^{(m)} = \underline{C}^{(m)}\,\underline{B}^{(m)}\,\underline{U} \qquad (A.3)$$

An important fact is that -- for the continuum considered -- the principle of virtual work holds, of course, for the entire body and when applied to *any* arbitrary segment of the body. Therefore, let us consider this segment to be a single finite element and define the element nodal point forces, in fact already used in Eq. (A.2),

$$\underline{F}^{(m)} = \left[\int_{V^{(m)}} \underline{B}^{(m)T}\,\underline{C}^{(m)}\,\underline{B}^{(m)}\,dV\right]\underline{U} \qquad (A.4)$$

where $\underline{U}$ is the displacement vector calculated in Eq. (A.2). Now making the fundamental assumption that there exists and we can calculate an improved finite element stress $\underline{\tau}^{(m)}$ that results into element surface tractions equivalent in the virtual work sense to these nodal point forces (including the effect of the body forces), we obtain from Eq. (A.2)

$$\int_{S_f^{(m)}} \underline{H}^{(m)T}\left\{\underline{\tau}^{(m)}\,\underline{n}^{(m)}\right\}dS = \underline{F}^{(m)} - \int_{V^{(m)}} \underline{H}^{(m)T}\,\underline{f}^{B}\,dV \qquad (A.5)$$

where $\underline{n}^{(m)}$ is the unit normal to the element boundary, and, of course, the element nodal point forces $\underline{F}^{(m)}$ correspond to the directly-calculated stresses $\underline{\tau}_h^{(m)}$:

$$\underline{F}^{(m)} = \int_{V^{(m)}} \underline{B}^{(m)T}\left\{\underline{\tau}_h^{(m)}\right\}dV \qquad (A.6)$$

In the absence of body forces, Eq. (A.5) reduces to:

$$\int_{S_f^{(m)}} \underline{H}^{(m)T} \left\{ \underline{\tau}^{(m)} \underline{n}^{(m)} \right\} dS = \underline{F}^{(m)} \qquad \text{(A.7)}$$

This equation states that for any virtual displacement field contained in the element interpolation functions of $\underline{H}^{(m)}$, the virtual work by the element boundary tractions is equal to the virtual work by the element nodal point forces, and hence we call this equation "the principle of virtual work in the form of boundary tractions".

We use this relation to establish the finite element stresses without differentiation of another field, and use interpolation functions that correspond to a larger stress space than implicitly used for $\underline{\tau}_h^{(m)}$. As a result $\underline{\tau}^{(m)}$ should be closer to the exact stresses than $\underline{\tau}_h^{(m)}$. Furthermore, if the finite element stresses are calculated using the principle of virtual work in traction form, we have

Property 1: *Every element in the assemblage is in force and moment equilibrium under the action of its boundary tractions.*

Property 2: *An averaged equilibrium is satisfied over the finite element domain.*

Property 3: *The patch test [1] is satisfied.*

Property 1 holds since the element nodal point forces satisfy this property, see ref. [1]. Note that therefore, no work is done under any imposed rigid body motion. Therefore, also

$$\int_{S_f^{(m)}} \left\{ \underline{\tau}^{(m)} \underline{n}^{(m)} \right\} dS + \int_{V^{(m)}} \underline{f}^B \, dV = \underline{0} \qquad \text{(A.8)}$$

and hence Property 2 follows

$$\int_{V^{(m)}} \left\{ div\left(\underline{\tau}^{(m)}\right) + \underline{f}^{B} \right\} dV = \underline{0} \qquad \text{(A.9)}$$

Therefore, rather than imposing equilibrium on the differential level, the principle of virtual work in traction form imposes an averaged equilibrium over the finite element domain.

Finally, if the finite element solution $\underline{U}$ is exact, the element nodal point forces correspond to the exact element boundary tractions and Property 3 follows.

A.1.2 The principle of virtual work in the form of internal stresses

Although the finite element solution obtained in Eq. (A.2) does not satisfy differential equilibrium at every point in the continuum, as already mentioned, two important properties always hold for *any* coarseness of mesh [1], [14].

Nodal Point Equilibrium: *At any node the sum of the element nodal point forces is in equilibrium with the externally applied nodal loads.*

Element Equilibrium: *Each element m is in force and moment equilibrium under the action of its nodal point forces, $\underline{F}^{(m)}$.*

Hence, we also require in our procedure that the improved finite element stress must correspond to the element nodal point forces given in Eq. (A.6); that is, we require

$$\int_{V^{(m)}} \underline{B}^{(m)T} \left\{ \underline{\tau}^{(m)} \right\} dV = \underline{F}^{(m)} \qquad \text{(A.10)}$$

Equation (A.10) states that for any virtual displacement field contained in the element interpolation functions, the element internal virtual work is equal to the virtual work of the element nodal point forces, and hence we call this equation "the principle of virtual work in the form of internal stresses".

Unlike for Eq. (A.5), not all the equations in Eq. (A.10) are linearly independent of each other. Specifically, in two-dimensional analysis, the displacement interpolation functions contain the three rigid body modes, and hence *only* $N-3$ *equations are linearly independent* when N is the number of nodal point element displacement degrees of freedom. Additionally, the two forms of the principle of virtual work are not necessarily independent of each other. Expressing Eq. (A.5) in index notation, we have

$$\int_{S_f^{(m)}} h_i^{(m)} \tau_{kj}^{(m)} n_j^{(m)} \, dS = F_i^{k\,(m)} - \int_{V^{(m)}} h_i^{(m)} \, f_k^{B} \, dV \qquad \text{(A.11)}$$

and hence we obtain

$$\int_{V^{(m)}} \left(h_{i,j}^{(m)} \tau_{kj}^{(m)} + h_i^{(m)} \tau_{kj,j}^{(m)} \right) dV = F_i^{k\,(m)} - \int_{V^{(m)}} h_i^{(m)} \, f_k^{B} \, dV$$

Thus

$$\int_{V^{(m)}} \underline{H}^{(m)T} \left\{ div\left(\underline{\tau}^{(m)} \right) + \underline{f}^{B} \right\} dV = \underline{F}^{(m)} - \int_{V^{(m)}} \underline{B}^{(m)T} \left\{ \underline{\tau}^{(m)} \right\} dV \qquad \text{(A.12)}$$

As a consequence of Eq. (A.10), the right hand side of Eq. (A.12) is zero and we have

$$\int_{V^{(m)}} \underline{H}^{(m)T} \left\{ div\left(\underline{\tau}^{(m)}\right) + \underline{f}^{B} \right\} dV = \underline{0} \qquad \text{(A.13)}$$

Therefore, the benefit of imposing the principle in both forms is that differential equilibrium over the element is satisfied more closely than if the principle were only imposed in traction form.

Finally, from Eqs. (A.9) and (A.13) it is evident that the two principle of virtual work statements are only independent of each other if the assumed space for $\underline{\tau}^{(m)}$ contains functions of high enough order.

A.2 A scheme for two-dimensional problems

The basis of the nodal point force based stress calculation method is the fact that the element nodal point forces are of higher quality than the directly-calculated finite element stresses, and so we use the two principle of virtual work statements discussed above to calculate the finite element stresses.

However, we need to recognize that for low interpolation orders of element displacements, the element nodal point forces are not unique to a particular stress state since they result from tractions acting on either face that the node connects to. Consequently, we use the nodal point forces acting on a predetermined patch of elements and call this patch of elements “the stress calculation domain”. The basic steps employed by the procedure are:

1. Idealise the structure or continuum as an assemblage of discrete finite elements, and perform the usual finite element analysis to solve for the element nodal point displacements $\underline{U}$, and the element nodal point forces $\underline{F}^{(m)}$.

2. Assume appropriate functions for $\underline{\tau}^{(m)}$ for each displacement-based element contained within the stress calculation domain.

3. Use the two principle of virtual work statements -- Eqs. (A.5) and (A.10) -- to solve for the unknown stress coefficients in $\underline{\tau}^{(m)}$.

4. Finally, to establish the improved stresses for a general displacement-based element m, in two-dimensional analysis, the stress coefficients corresponding to all possible combinations of stress calculation domains that contain element m are calculated using the above steps, and the results are averaged. By averaging the stress coefficients, the solution is independent of the specific application of stress calculation domain for the element, and the maximum amount of element nodal point force information is utilised.

An important decision is to choose appropriate functions for $\underline{\tau}^{(m)}$. The functions must be symmetric for all stress components so as to ensure invariance, and the dimension must be such that the application of the principle of virtual work in both forms generates either a determined or an over-determined system of equations. There are many possibilities for choosing the stress space; however, evidently, the larger the size, the more accurate the solution, and so the largest space which results in a well-posed problem for all patch geometries, that is, stress calculation domains, which might be used.

The numerical effort to calculate the element stresses using the above algorithm is small but, also, these stress calculations need of course not be performed for each element in the entire finite element assemblage. Instead, the procedure could only be used for certain regions of the analysis domain, namely those regions where improved stresses are of interest.

In the following we consider two cases: the first case leads to a determined system of equations, and the second case leads to an over-determined system of equations for the improved element stresses. In both cases, we find that the stress prediction is greatly improved.

A.2.1 Improving the stresses of the 4-node quadrilateral element: a case where the system of equations is determined

Consider an undistorted 4-node quadrilateral element. The displacement trial functions are C^0 continuous and take the form:

$$\underline{u}^{(m)} = \begin{Bmatrix} v^{(m)} \\ w^{(m)} \end{Bmatrix} = \begin{Bmatrix} \alpha_1^{(m)} + \alpha_2^{(m)}\, y + \alpha_3^{(m)}\, z + \alpha_4^{(m)}\, y\, z \\ \beta_1^{(m)} + \beta_2^{(m)}\, y + \beta_3^{(m)}\, z + \beta_4^{(m)}\, y\, z \end{Bmatrix}$$

Upon differentiating, the strains are found to be:

$$\underline{\varepsilon}^{(m)} = \begin{Bmatrix} \varepsilon_{yy}^{(m)} \\ \varepsilon_{zz}^{(m)} \\ \gamma_{yz}^{(m)} \end{Bmatrix} = \begin{Bmatrix} \alpha_2^{(m)} + \alpha_4^{(m)}\, z \\ \beta_3^{(m)} + \beta_4^{(m)}\, y \\ \left(\alpha_3^{(m)} + \beta_2^{(m)}\right) + \alpha_4^{(m)}\, y + \beta_4^{(m)}\, z \end{Bmatrix} \qquad \text{(A.14)}$$

Equation (A.14) shows that the stresses do not admit zero shear strain when the element is subjected to bending. It follows that the element is much too stiff in bending, and this phenomenon is known as shear locking [1].

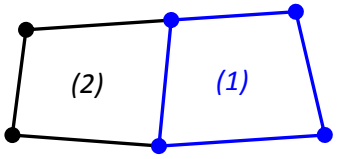

Fig. A.1: *The stress calculation domain for the 4-node quadrilateral element, two 4-node adjacent finite elements; element m would one of the two elements*

In order to improve the predictive capabilities, the element stress space must be increased, and we use a stress calculation domain corresponding to two adjacent displacement-based elements, see *Fig. A.1*. The stresses within each displacement-based element m are bilinearly interpolated, and hence each stress calculation domain requires twenty-four coefficients

$$\underline{\tau}^{(m)} = \begin{Bmatrix} \tau_{yy}^{(m)} \\ \tau_{zz}^{(m)} \\ \tau_{yz}^{(m)} \end{Bmatrix} = \begin{Bmatrix} \alpha_1^{(m)} + \alpha_2^{(m)}\, y + \alpha_3^{(m)}\, z + \alpha_4^{(m)}\, y\, z \\ \beta_1^{(m)} + \beta_2^{(m)}\, y + \beta_3^{(m)}\, z + \beta_4^{(m)}\, y\, z \\ \zeta_1^{(m)} + \zeta_2^{(m)}\, y + \zeta_3^{(m)}\, z + \zeta_4^{(m)}\, y\, z \end{Bmatrix} \quad \text{for } m = 1, 2$$

where the $\alpha_i^{(m)}$, $\beta_i^{(m)}$, $\zeta_i^{(m)}$ are the twenty-four stress coefficients to be found.

These unknown stress coefficients are determined by imposing Eq. (A.5) to all possible closed contour boundaries contained within the domain and Equation (A.10) to the complete domain.

Finally, the stresses for each displacement-based element m are obtained by averaging the stress coefficients corresponding to the possible stress calculation

domains that contain element m. Of course, for this stress calculation domain there can be no more than four domains that contain element m.

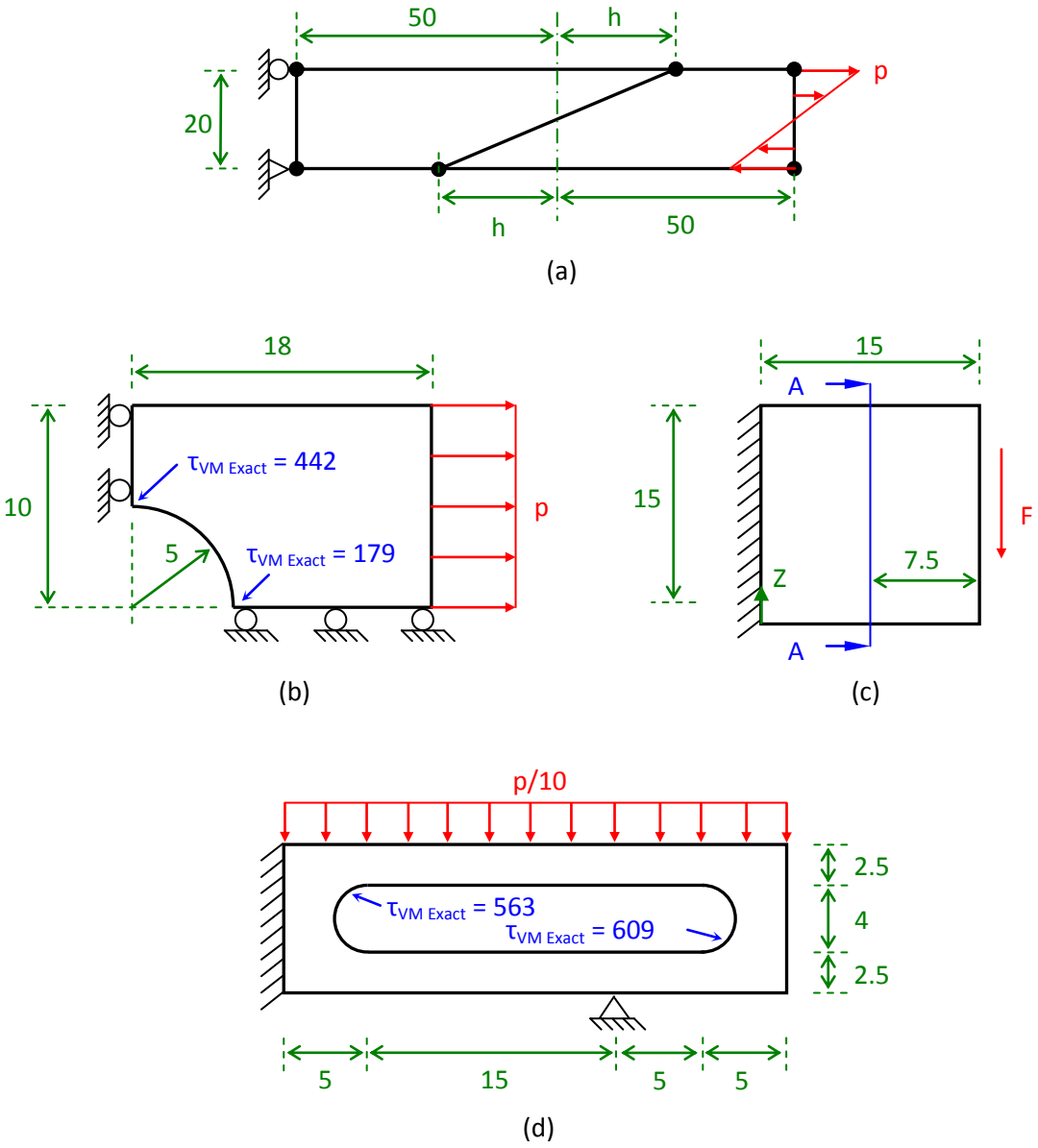

Fig. A.2: *Four plane stress test problems for the 4-node quadrilateral element (E = 72E9, v = 0.0, t =1, p = 100, F = 1,500): (a) the beam in pure bending problem, (b) the finite plate with a central hole under tensile loading problem, (c) the square cantilevered plate under shear loading problem, and (d) the tool jig problem*

In this case, the stresses have been assumed to be discontinuous and bilinear; however, it can be shown that the application of the two principle of virtual work statements in essence reduces the assumption on the stresses to be simply linear, and ensures that the mutual forces of action and reaction are continuous across the internal boundary.

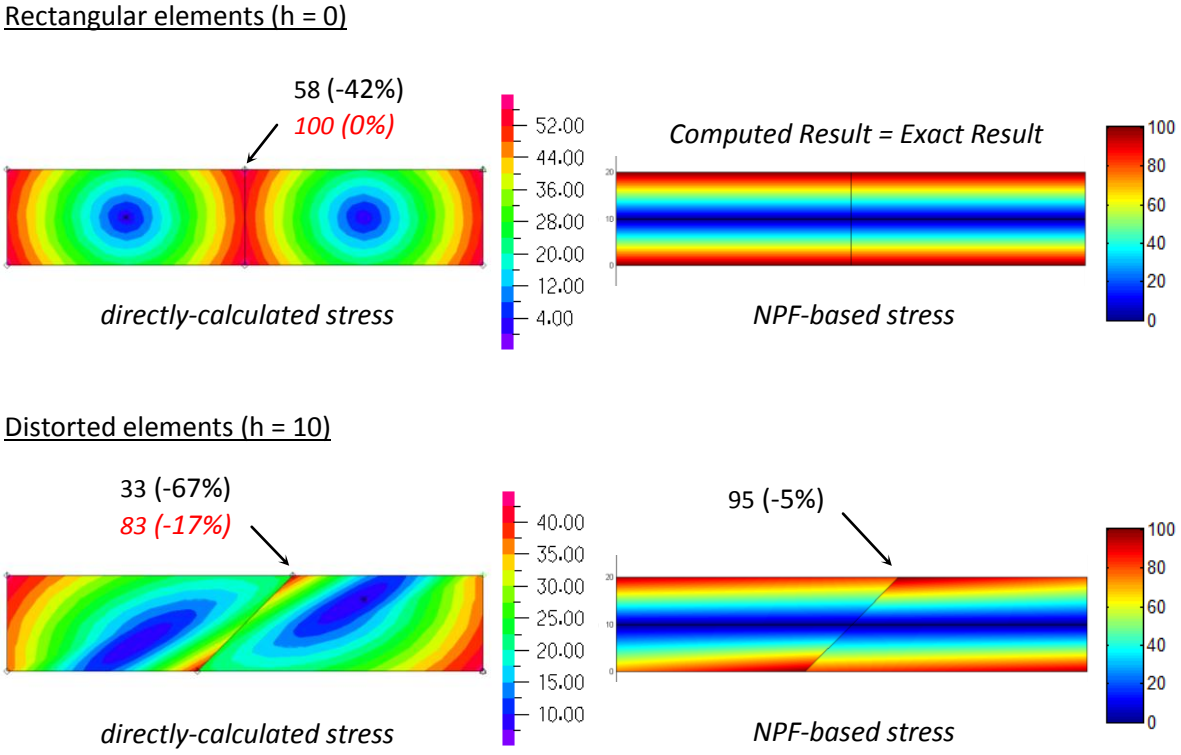

Fig. A.3: *von Mises stress results for the beam problem. The solution error is given in parentheses. The incompatible modes directly-calculated stress results are given underneath the displacement-based directly-calculated stress*

The effectiveness of the stress calculation procedure for the 4-node quadrilateral element is illustrated using the following four plane stress test problems: a beam in pure bending, a finite plate with a central hole under tensile loading, a square cantilevered plate under shear loading, and a tool jig problem (like considered in ref. [14]). These test problems are defined in *Fig. A.2*, and the results (rounded to

full digits) are given in *Fig. A.3* to *Fig. A.6* respectively, where the NPF-based stress refers to the stresses calculated using the proposed nodal point force based stress calculation method.

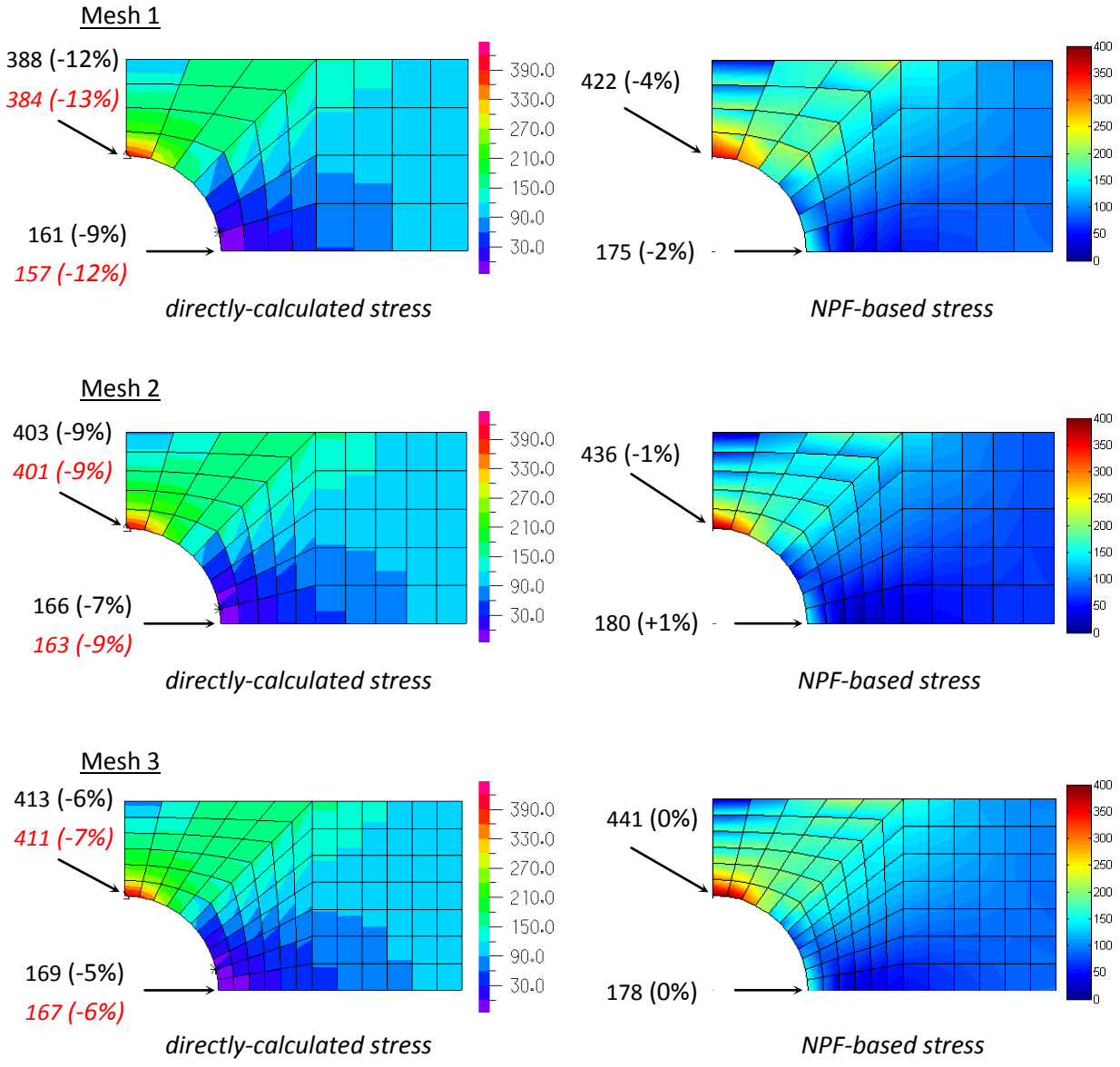

Fig. A.4: *von Mises stress results for the finite plate with a central hole problem. These results are presented in the same form as those shown in Fig. A.3*

Considering the results, the values given in the contour plots are un-averaged, while the actual stress values are the averaged nodal point values with the solution error shown in parentheses. This error is measured with respect to the solution obtained with a very fine mesh of 9-node elements. Also, for reference, the directly-calculated stresses using incompatible modes are reported, since these values can be more accurate than the stresses obtained without the use of incompatible modes [1].

As expected, we see a significant improvement in the accuracy of the predicted stresses for all problems considered. The beam problems are statically determinate problems and hence a large improvement in the stress accuracy should be expected, but, also, in the analysis of the plate with a hole and the tool jig problem a good improvement in accuracy is seen.

Mesh 1

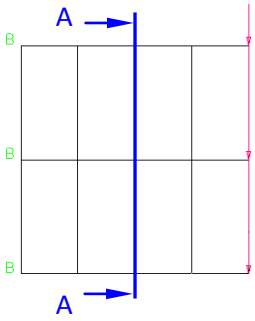

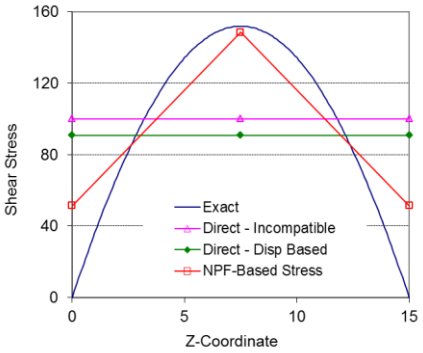

Mesh 2

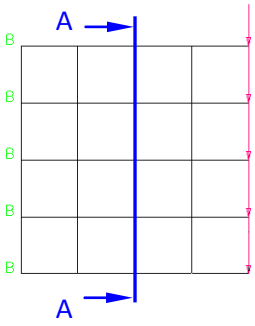

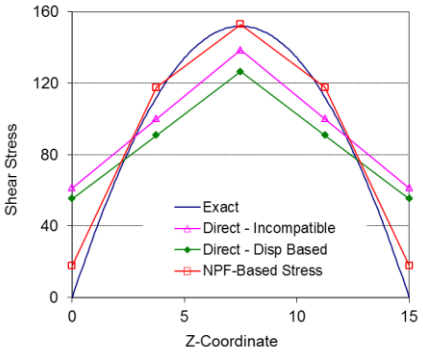

Mesh 3

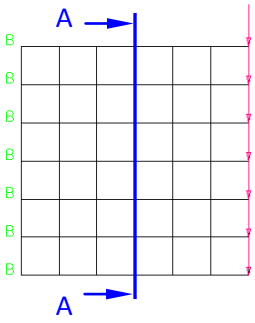

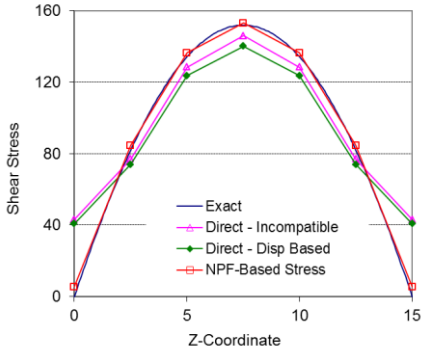

Fig. A.5: *In-plane shear stress results for the square cantilevered plate problem*

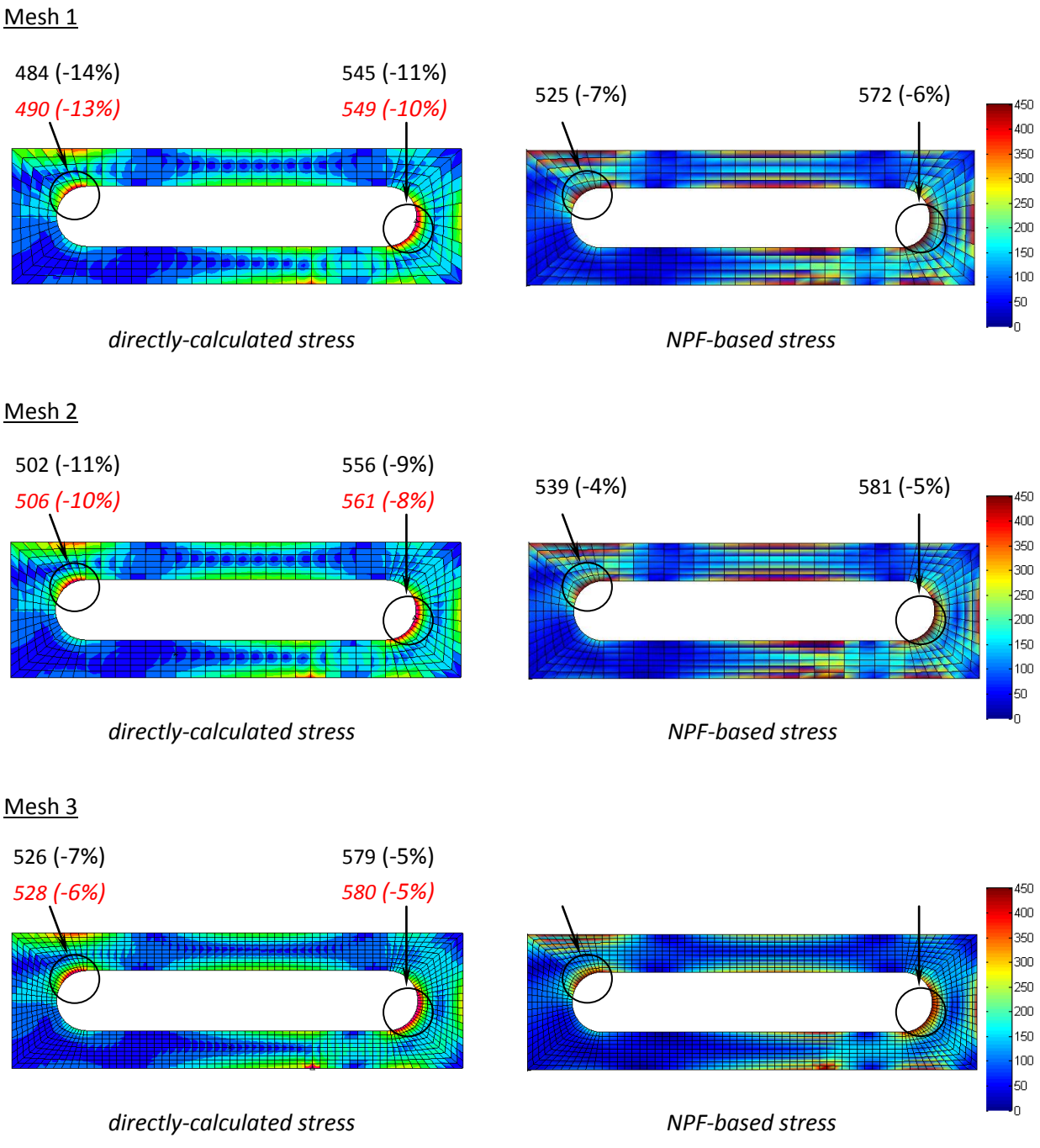

Fig. A.6: *von Mises stress results for the tool jig problem. These results are presented in the same form as those shown in Fig. A.3*

A.2.2 Improving the stresses of the 3-node triangular element: a case where the system of equations is over-determined

The displacement functions for the 3-node triangular element are linear; therefore, the strains (and hence the stresses) are constant over the element in plane stress analysis. The element is of particular interest because it is inexpensive to calculate, and the use of incompatible modes (or enhanced strains) for this element is not effective.

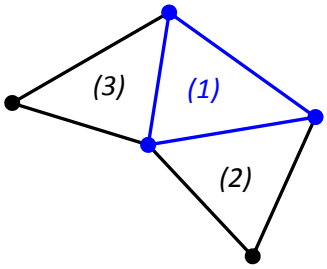

Fig. A.7: *Stress calculation domain for the constant strain triangle; element m would be the middle element or a side element*

In our procedure, we use a stress calculation domain of any three adjacent constant strain triangles, such as shown in *Fig. A.7*. As for the quadrilateral element, the stresses are interpolated bilinearly but now stress inter-element continuity is assumed throughout the domain. Hence, each domain leads to

$$\underline{\tau}^{(m)} = \begin{Bmatrix} \tau_{yy}^{(m)} \\ \tau_{zz}^{(m)} \\ \tau_{yz}^{(m)} \end{Bmatrix} = \begin{Bmatrix} \alpha_1 + \alpha_2\, y + \alpha_3\, z + \alpha_4\, y\, z \\ \beta_1 + \beta_2\, y + \beta_3\, z + \beta_4\, y\, z \\ \zeta_1 + \zeta_2\, y + \zeta_3\, z + \zeta_4\, y\, z \end{Bmatrix} \quad for \quad m = 1, 2, 3$$

where the α_i, β_i, ζ_i are the twelve stress coefficients to be found.

Mesh 1

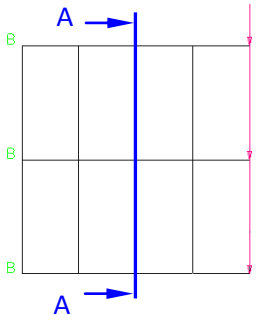

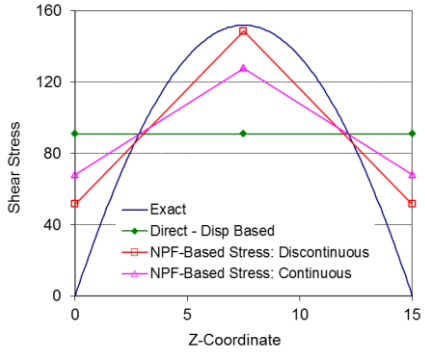

Mesh 2

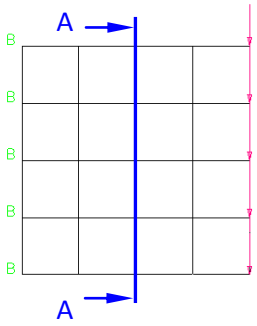

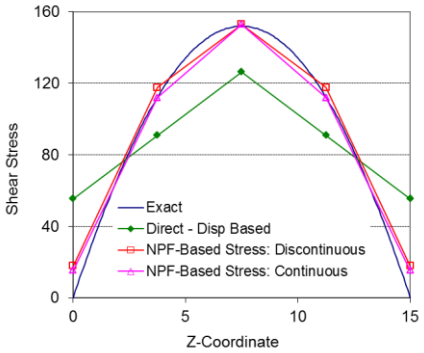

Mesh 3

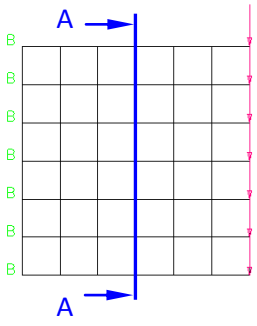

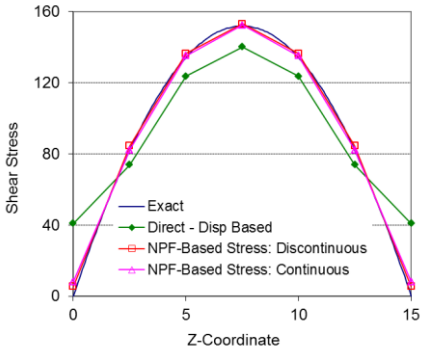

Fig. A.8: *In-plane shear stress results for the square cantilevered plate problem of Fig. A.2c. The directly-calculated stress is compared to the improved stress calculated using the discontinuous and continuous stress assumptions*

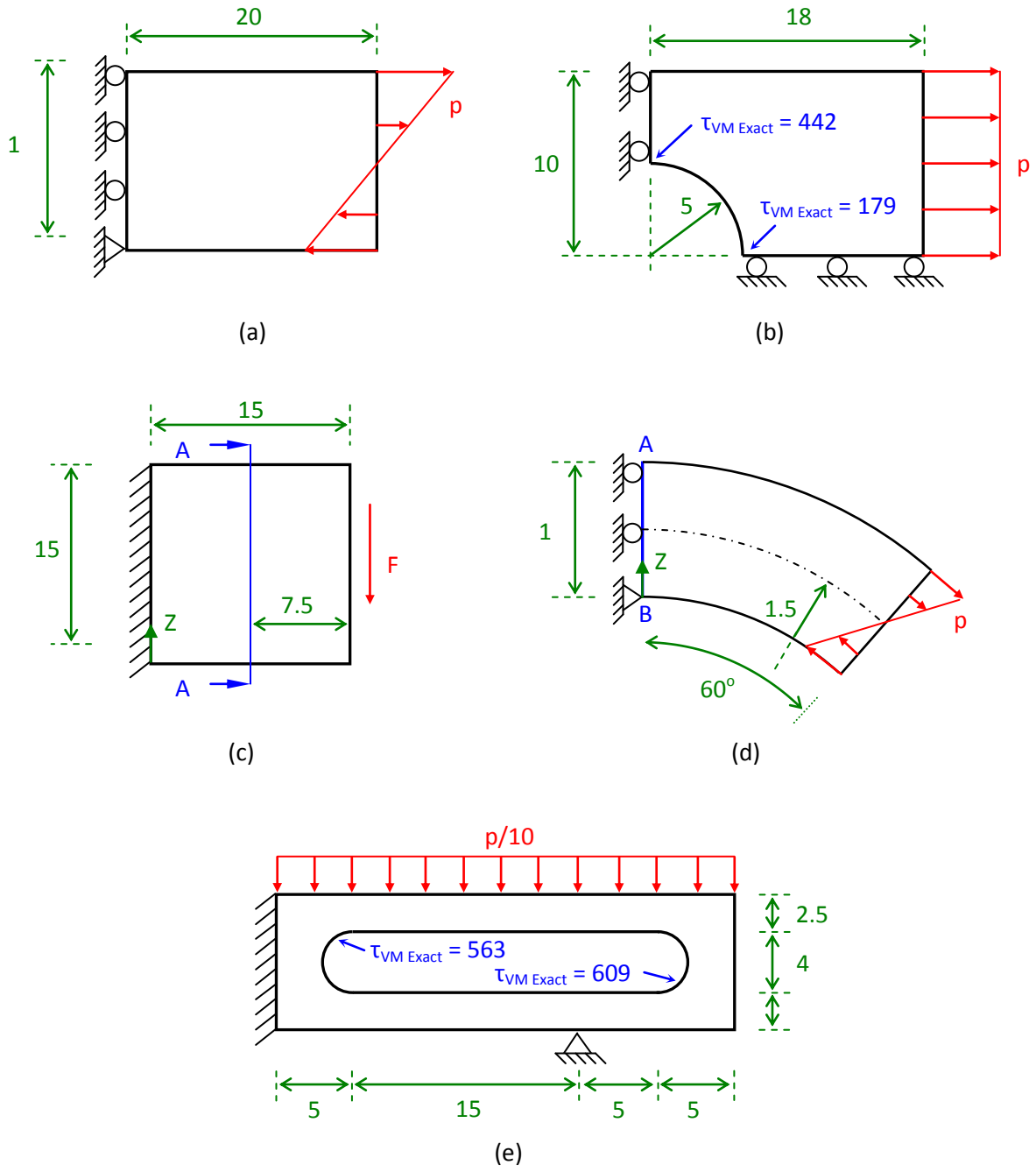

Fig. A.9: *Five plane stress test problems for the constant strain triangular element (E = 72E9, v = 0.0, t =1, p = 100, F = 1,500): (a) the beam in pure bending problem, (b) the finite plate with a central hole under tensile loading problem, (c) the square cantilevered plate under shear loading problem, (d) the curved structure under pure bending problem, and (e) the tool jig problem*

These unknown stress coefficients are determined by imposing Equation (A.5) to all possible closed contour boundaries contained within the domain and Equation (A.10) to the complete domain.

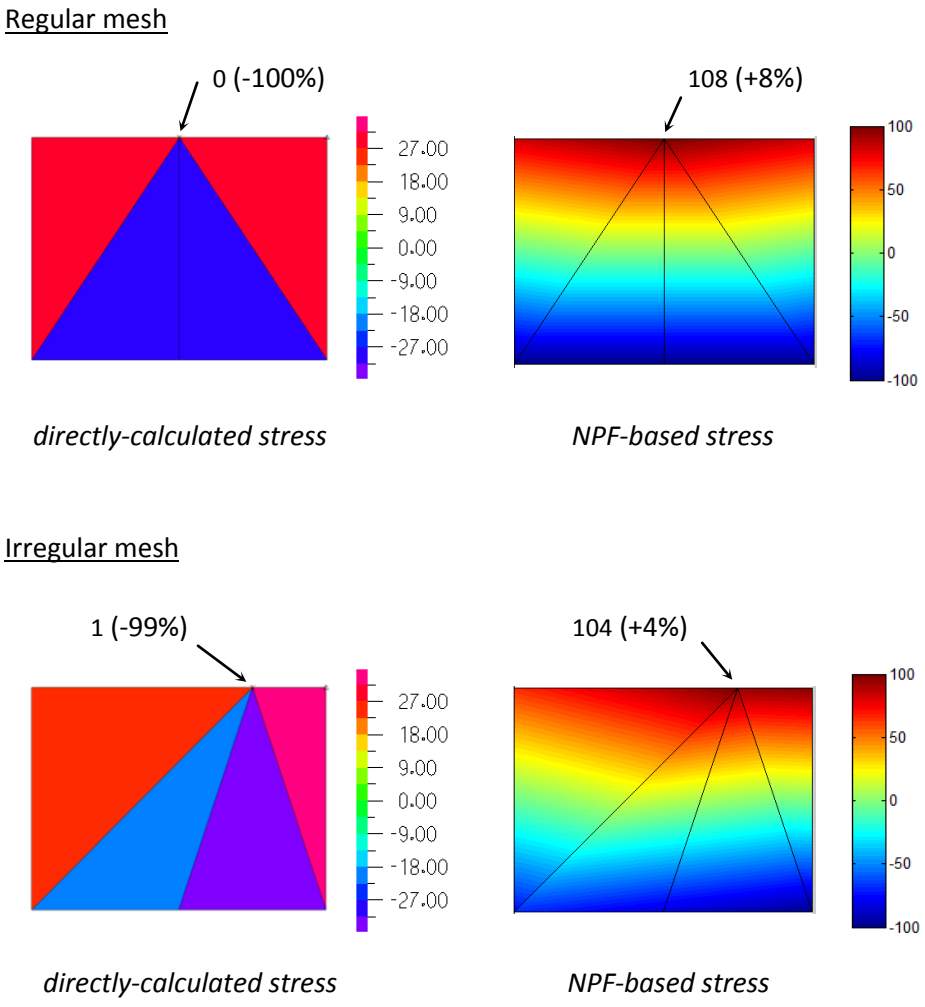

Fig. A.10: *Longitudinal stress results for the beam problem. The solution error is given in the parentheses*

Finally, the stresses for each constant strain triangle m are calculated by averaging the stress coefficients corresponding to all possible stress calculation domains that contain element m, and for the chosen geometry there can be no more than nine

different domains that contain element m, three and six for the element taking the position of the middle and side elements, respectively.

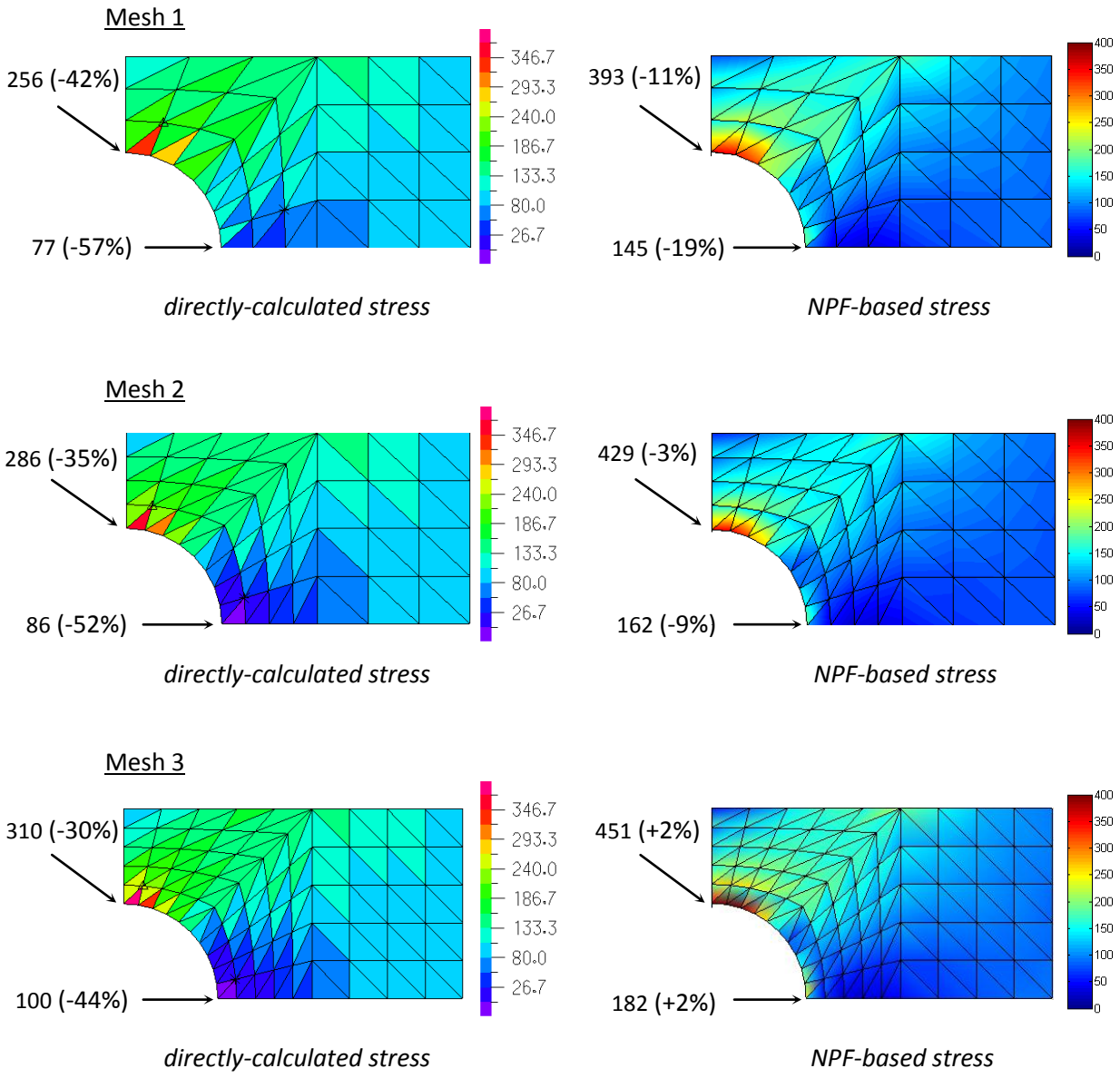

Fig. A.11: *von Mises stress results for the finite plate with a central hole problem. These results are presented in the same format as those shown in Fig. A.10*

In this case, inter-element stress continuity has been assumed. Hence, Eq. (A.5) can be imposed to every possible closed contour boundary, simply by imposing

the equation to the three displacement-based element boundaries. Furthermore, since the functional stress space corresponds to only twelve coefficients, the problem is over-determined, and so, in general, a solution which exactly satisfies the two principle of virtual work statements does not exist; hence we use the least squares method to evaluate the stress coefficients.

Mesh 1

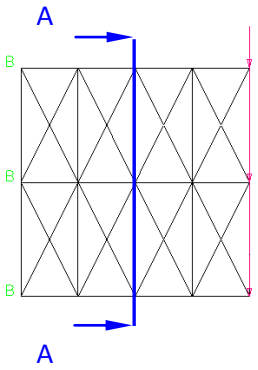

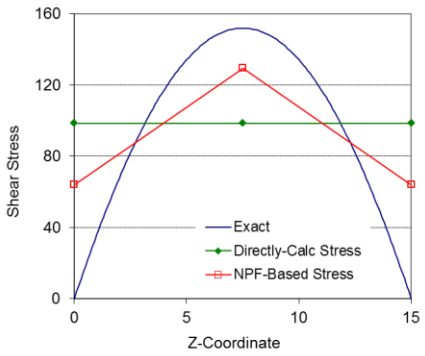

Mesh 2

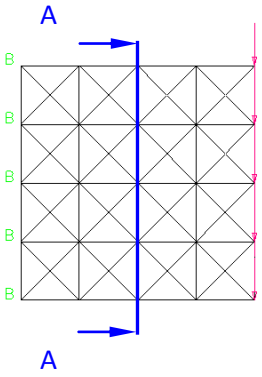

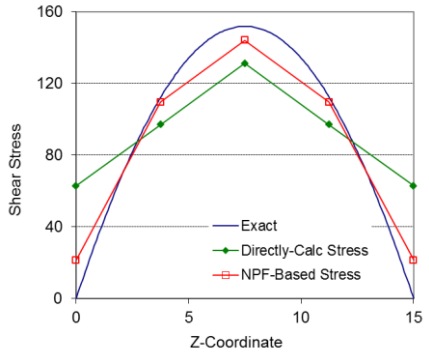

Mesh 3

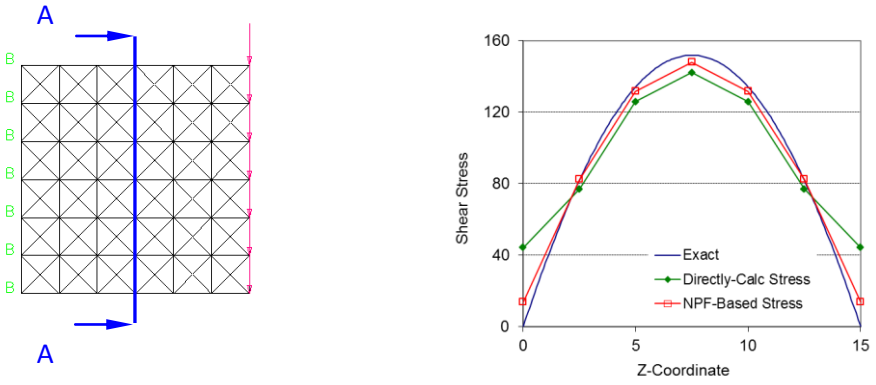

Fig. A.12: *In-plane shear stress results for the square cantilevered plate problem*

It is interesting to note that this continuous bilinear stress space could also have been used to calculate the stresses for the 4-node quadrilateral element. However, since this stress space is smaller than the discontinuous field assumed in appendix A.2.2, this assumption will produce less accurate stresses than those given earlier, for a comparison see *Fig. A.8*.

The effectiveness of our procedure for the constant strain element is illustrated using the following five plane stress test problems: a beam in pure bending, a finite plate with a central hole under tensile loading, a square cantilevered plate in shear loading, a curved structure in pure bending, and a tool jig problem. These test problems are defined in *Fig. A.9*, and the results are given in *Fig. A.10* to *Fig. A.14*, respectively.

The results are presented in the same form as those given in appendix A.2. We note that in this case, the improvement in the accuracy of the predicted stresses is even more pronounced than seen for the 4-node quadrilateral element, which of course is due to the fact that $\underline{\tau}_h^{(m)}$ is constant in the 3-node finite element.

Mesh 1

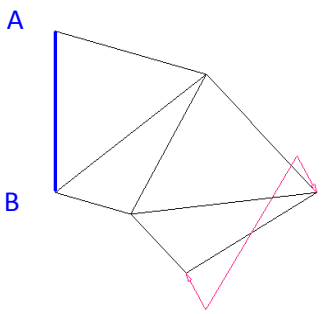

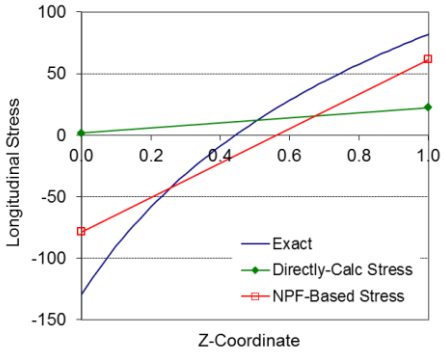

Mesh 2

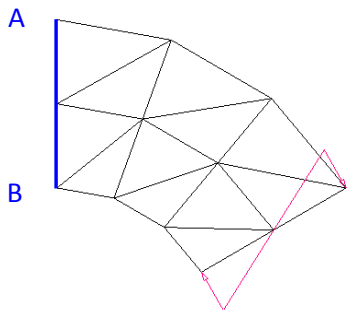

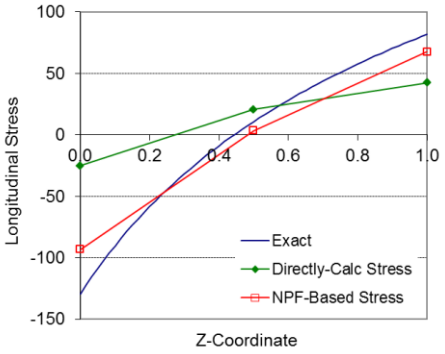

Mesh 3

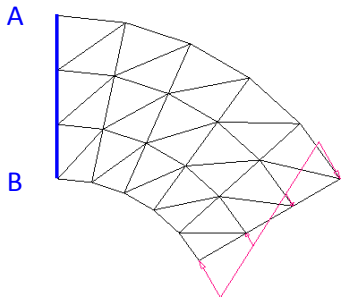

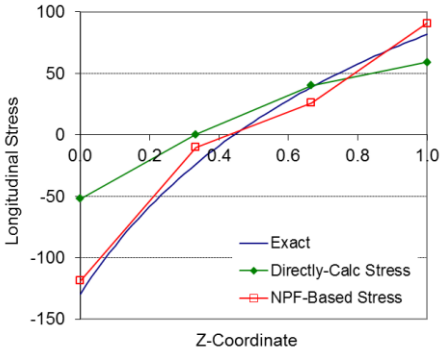

Fig. A.13: *Longitudinal normal stress results for the curved structure problem*

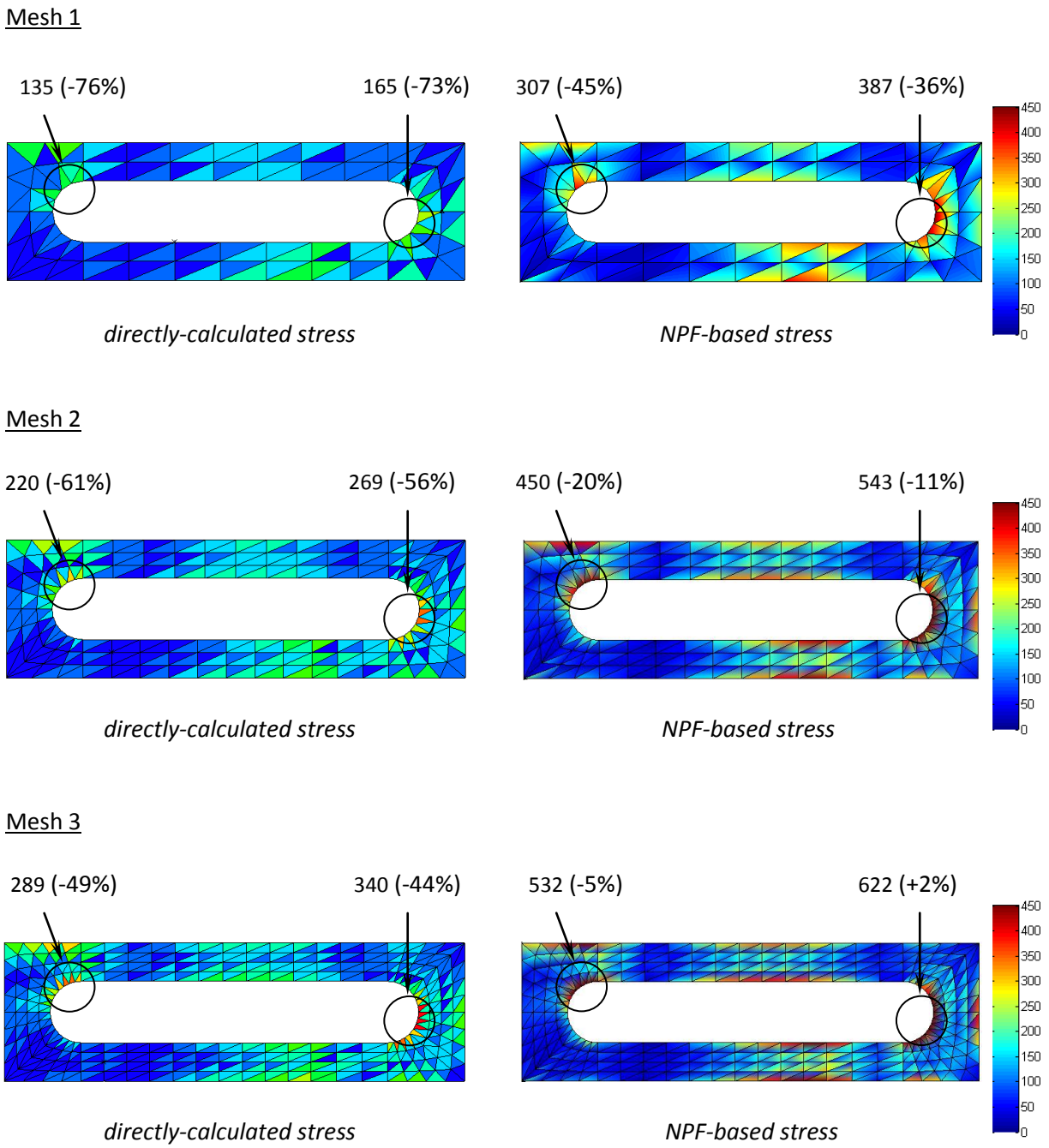

Fig. A.14: *von Mises stress results for the tool jig problem. These results are presented in the same format as those shown in Fig. A.10*

A.3 A scheme for three-dimensional problems

Most engineering problems in solids and structures are three-dimensional in nature. Since the geometry and other data of the problem are then usually complex, the structure is best analysed using finite element methods. The crucial step in any finite element analysis is to choose an appropriate mathematical model for the physical structure (or more generally the physical phenomenon), since a finite element solution solves only this model, see ref. [1]. For example, if the structure is thin in one direction and long in the other two directions a shell mathematical model is appropriate, and the problem is solved efficiently using the MITC shell elements, see refs. [2], [45] to [47]. However, if the length scales of the structure are similar in all directions, and the loading is general, then there is no option other than to solve the problem using an assemblage of discrete three-dimensional solid elements, see refs. [1] and [14].

The simplest three-dimensional solid element available to the finite element analyst is the 4-node constant strain tetrahedral element. This element is used abundantly in practice because the analyst is able to mesh almost any volume regardless of complexity, the element is robust in contact analysis, the element matrices are inexpensive to calculate, and the resulting global stiffness matrix has a relatively small bandwidth. In a typical approach, the analyst would use a mesh of 4-node tetrahedral elements, in a first analysis, to identify the locations of high stress concentrations, and then based upon these results, the analyst would refine the mesh -- or, if possible, convert the mesh to 10-node or 11-node tetrahedral elements -- in the localised regions of concern, see ref. [14]. This is necessary, simply because the stresses predicted using the 4-node tetrahedral element are known to be poor, and the lack of accuracy can be seen using stress band plots of unsmoothed stresses, see refs. [1], [4], [14].

The NPF-based method uses, as its ingredients, two fundamental virtual work statements -- Eqs. (A.5) and (A.10) -- to obtain finite element stresses that we can expect to be more accurate than those given by Eq. (A.3). We expect that, in general, more accurate stresses are predicted because, firstly, the method allows us to assume a richer functional space for the stresses than that implicitly assumed in establishing the stiffness matrix, and, secondly, the nodal point forces are used which always satisfy the above-mentioned important equilibrium requirements, irrespective of the coarseness of the mesh.

Our objective in this section is to apply the NPF-based method to the 4-node three-dimensional tetrahedral element, and show that by using a simple algorithm, we are able to enhance the stresses in localised regions of concern, without having to refine the mesh or re-analyse the model.

We showed that the NPF-based method can be used effectively to significantly improve the accuracy of the finite element stress predictions obtained using the 3- and 4- node displacement-based elements in two-dimensional analyses. It is reasonable to expect similar improvements for the 4-node three-dimensional tetrahedral element. We solve the same set of problems previously considered, but of course this time in three-dimensional settings. As expected, we see a significant improvement in the accuracy of the stress predictions for all problems considered. These results are of particular interest, since reliable improvements in stresses for the 4-node tetrahedral element, using incompatible modes or enhanced strains, are difficult to reach in general analyses [41] to [43].

A.3.1 Improving the stresses of the 4-node tetrahedral element

In order to establish improved stress predictions for a *general* finite element m, the NPF-based stress calculation algorithm employs four basic steps:

1. Solve, in the usual manner, for the element nodal point displacements $\underline{U}$, and the element nodal point forces $\underline{F}^{(m)}$, in accordance with Eq. (A.6).

2. Assume appropriate functions for $\underline{\tau}^{(m)}$ across a predetermined patch of elements; we call this patch of elements "the stress calculation domain".

3. Use the two principle of virtual work statements -- Eqs. (A.5) and (A.10) -- to solve for the unknown stress coefficients in $\underline{\tau}^{(m)}$.

4. Finally, to establish the improved stresses for an individual element m, the stress coefficients corresponding to all possible element combinations to obtain stress calculation domains that contain element m are calculated using the above steps, and the results are averaged for element m.

Of course, it is important to select appropriate functions for the stress fields in $\underline{\tau}^{(m)}$, since we aim to have a sufficiently rich assumed stress space for the stress calculation domain. Clearly, the dimension of the assumed stress space must depend on the number of elements used within the stress calculation domain. That is, for a given dimension of assumed stress space, we must have that the domain contains a sufficient number of elements, such that the problem solution for the

unknown stress coefficients is well-posed for all possible domain geometries that might be used.

In the specific case of the 4-node tetrahedral three-dimensional element, we assume the stresses to be linearly interpolated and continuous across the entire stress calculation domain,

$$\tau_{ij}^{(m)} = \alpha_1^{ij} + \alpha_2^{ij}\, x + \alpha_3^{ij}\, y + \alpha_4^{ij}\, z \qquad \textit{for} \qquad m = 1, 2, 3, 4, 5 \qquad \text{(A.15)}$$

where the (i, j) refer to the coordinate directions, and the α_k^{ij} are the twenty-four unknown stress coefficients to be found. As an aside, we note that for the 3-node constant strain triangle considered in section A.2 we instead assumed bilinear interpolations across its stress calculation domain.

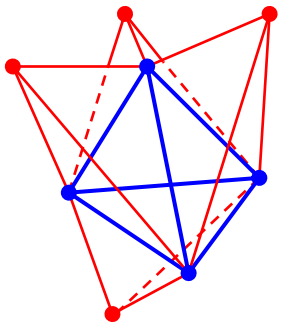

Fig. A.15: *The stress calculation domain for the 4-node tetrahedral element; element m would be the central element or a peripheral element*

With the assumption in Eq. (A.15), each stress calculation domain for the 4-node tetrahedral element shall contain at least five elements, this way we ensure a well-posed problem for the solution of the coefficients. Although any five adjacent elements could be used, we define a stress calculation domain in a quite natural

manner as the unique combination corresponding to a central element surrounded by four peripheral elements, where each peripheral element shares a face with the central element, as shown in *Fig. A.15*. This stress calculation domain allows us also to maximise the accuracy of the stress prediction, since the averaging in step 4 is used, see above and the further comments below.

In general, the algorithm solves for the unknown stress coefficients in $\underline{\tau}^{(m)}$ by imposing Eq. (A.5) to all possible closed contour boundaries contained within the stress calculation domain, and in addition Eq. (A.10) to the complete domain. However, in this case, we have assumed the stresses to be linearly interpolated, and hence we need to only apply Eq. (A.5) in order to solve for the stress coefficients. The reason is that in the absence of body forces, Eq. (A.5) is not independent of Eq. (A.10), see section A.1. Furthermore, we assume inter-element stress continuity, and hence Eq. (A.5) can be imposed to every possible closed contour boundary by simply imposing the equation to the five tetrahedral element boundaries.

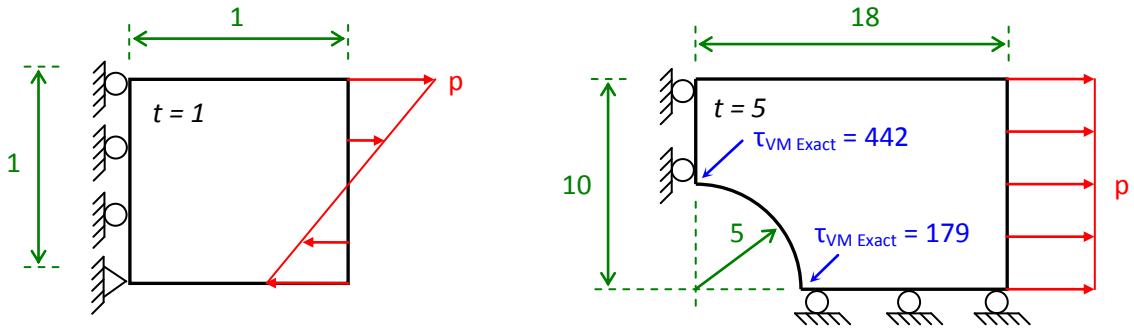

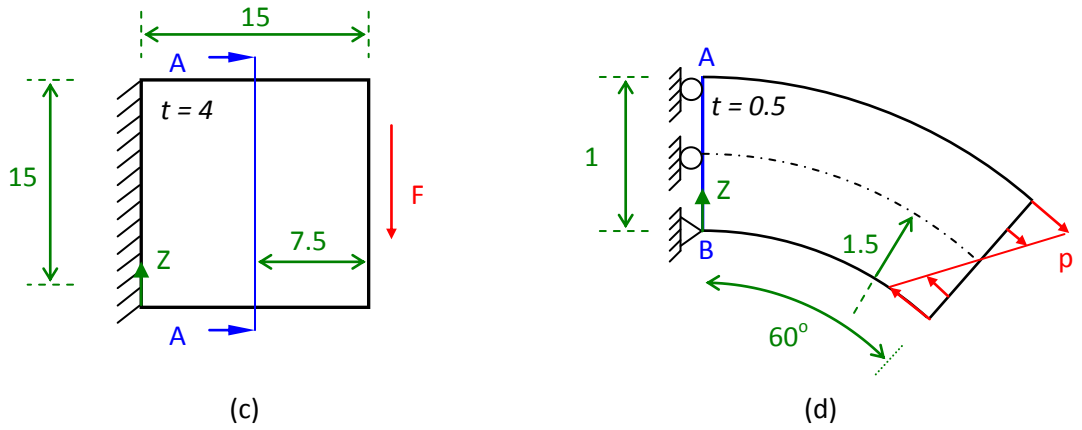

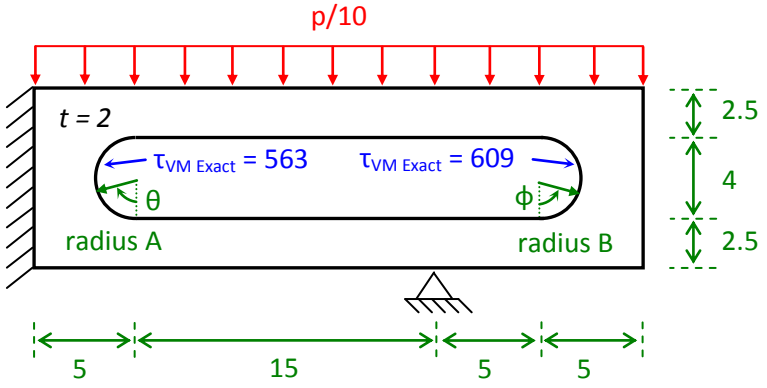

Fig. A.16: *Five test problems for the 4-node tetrahedral three-dimensional element (E = 72E9, v = 0.0, p = 100, F = 6,000, t = thickness): (a) the beam in pure bending problem, (b) the finite plate with a central hole under tensile loading problem, (c) the square cantilevered plate under shear loading problem, (d) the curved structure in pure bending, and (e) the tool jig problem*

In this way, we generate sixty equations, of which, for the configuration considered in *Fig. A.15*, only thirty-three are linearly independent. Since there are twenty-four unknown stress coefficients, the system of equations is over-determined, and so, in general, a solution which exactly satisfies Eq. (A.5) does

not exist. Hence we use the least squares method to solve for the unknown stress coefficients, with the consequence that the element nodal point forces calculated from the NPF-stresses (see Eq. (A.10)) will only satisfy the individual element and nodal equilibrium properties mentioned earlier, in a least squares sense.

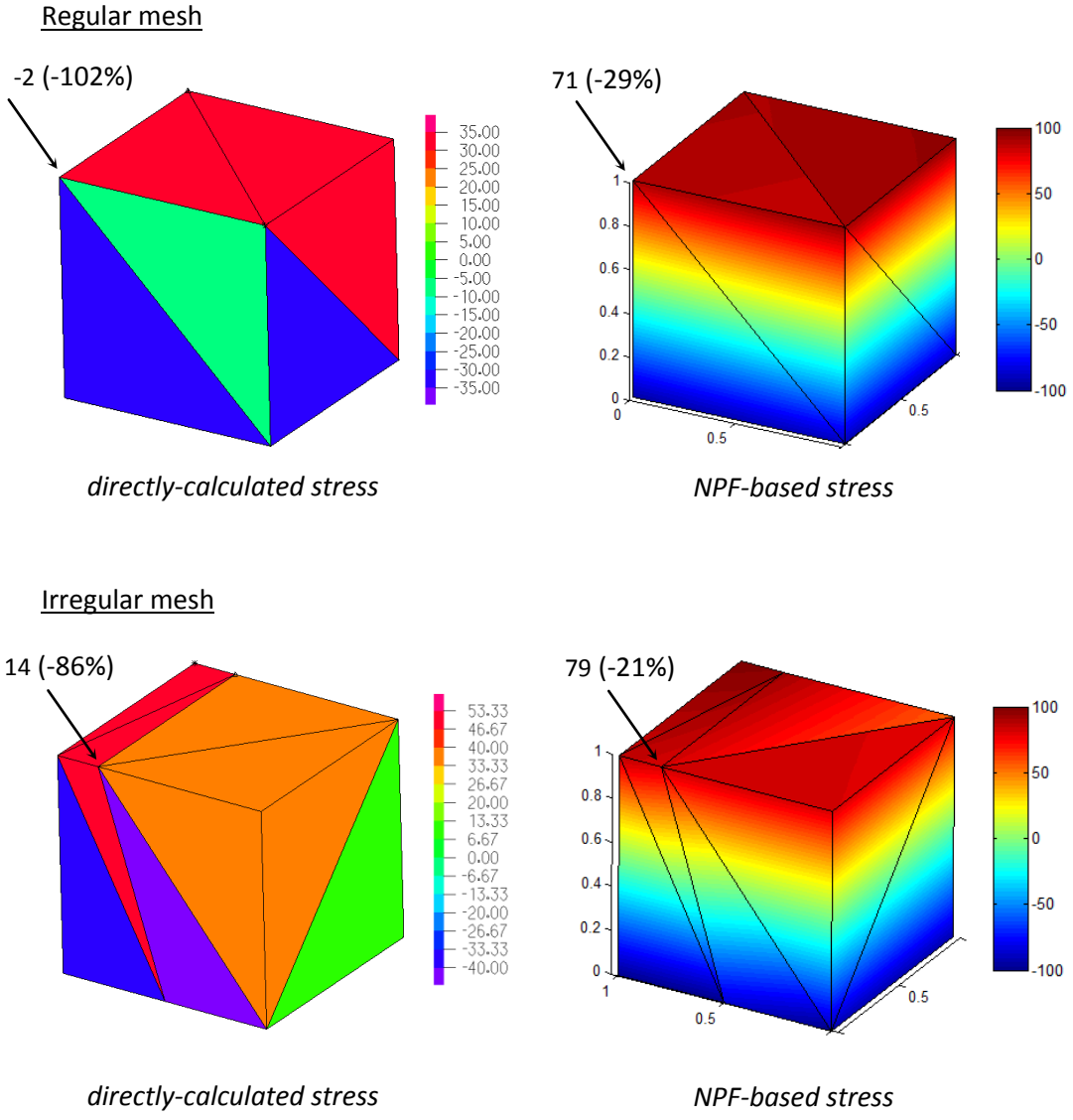

Fig. A.17: *Longitudinal stress results for the beam in pure bending problem. The solution error is given in the parentheses*

Finally, to obtain the improved stresses for each tetrahedral element m, we average the stress coefficients corresponding to the possible stress calculation domains that contain element m. Of course, for the chosen geometry there can be no more than five domains that contain element m, that is, respectively, one and four domains for the element taking the position of the central element and the peripheral elements. In the exceptional case that no domain, as described above, exists which contains element m (e.g. in a corner of a meshed geometry), we simply construct the stress domain using four elements that are properly connected to element m, and no averaging is applied.

Since we assume the stresses to be linearly interpolated, the numerical effort involved in improving the stress predictions for each tetrahedral element is given by the effort required to solve for twenty-four unknown stress coefficients at most five times (that is, we must calculate the stress coefficients corresponding to every possible domain which contains element m).

This computational effort is relatively small, but, also, an important feature of the algorithm is that there is no need to apply these stress calculations to all elements in the assemblage, instead only to those elements where improved stresses should be calculated. Indeed, in practice, the finite element analyst is not always able to perform -- due to stringent constraints on time and computational resources -- a detailed mesh refinement stress convergence study, especially for complex problems that are expensive to solve. Instead, in many cases, the analyst will solve the problem only once, using the finest mesh possible that for the available computational resources still results in a reasonable solution time. Given this solution and the above rather simple algorithm, it is then possible to enhance the stress prediction with relatively little computational effort in only the specific areas of concern.

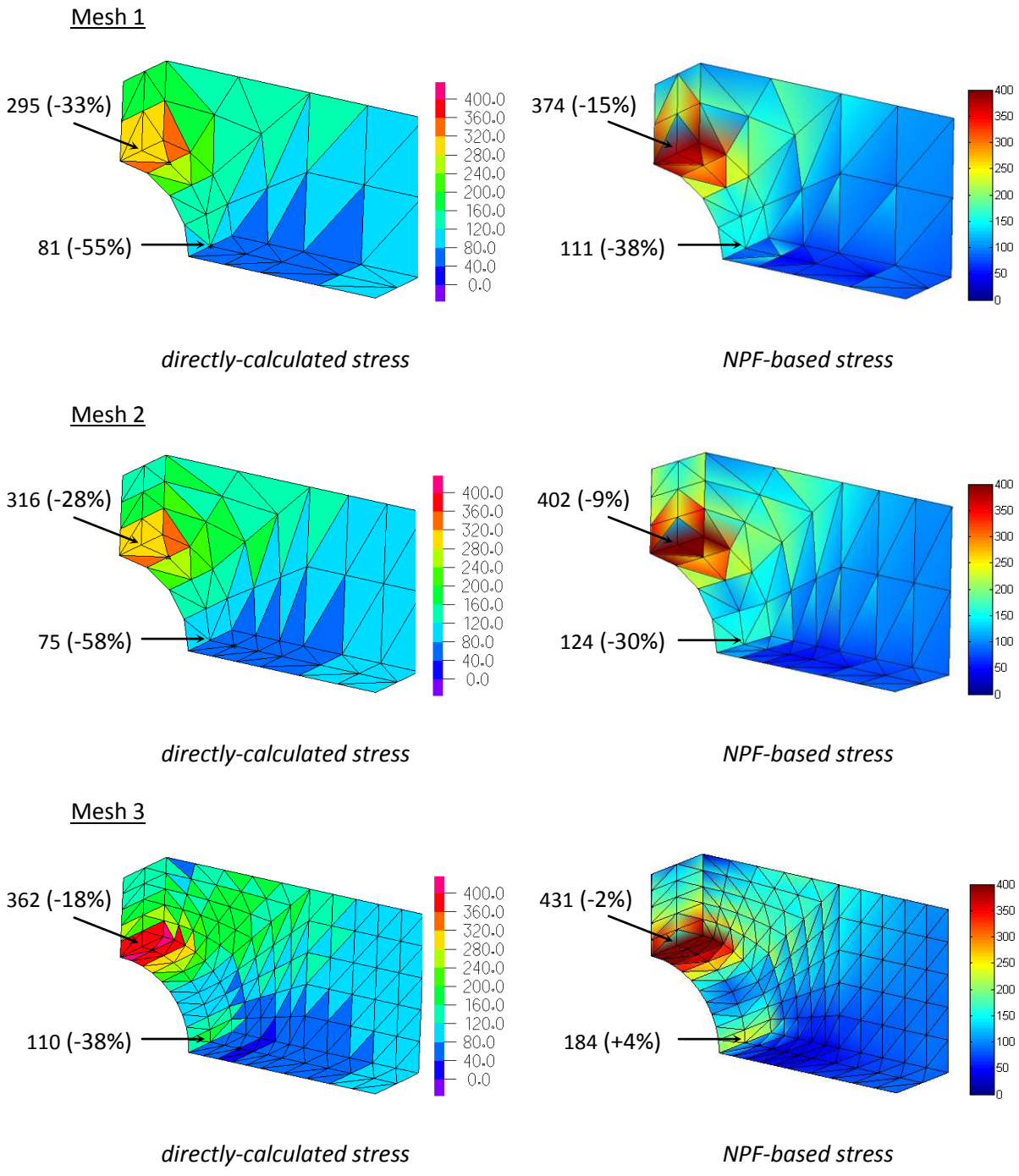

Fig. A.18: *von Mises stress results for the finite plate with a central hole problem. The solution error is given in the parentheses*

In addition to enhancing the stress prediction, the results obtained with the algorithm give, of course, also insight into the accuracy of the directly-calculated stresses. Namely, if the two stress values are far apart, in important areas of the model, the mesh used is too coarse for the directly-calculated stresses to be sufficiently accurate.

We recognise that we have not mathematically proven stability of the algorithm for *all* possible geometries of the stress calculation domains. Therefore, it is possible, that for certain meshes with grossly distorted elements the algorithm establishes ill-conditioned matrices in which case the solution would have to be abandoned for that particular domain (where the elements are too distorted). However, we have tested the procedure in a large number of domains containing highly distorted elements and have not encountered this difficulty. Hence our experience is that as long as the mesh is reasonable (which is anyways required for the original displacement solution) the algorithm seems to be quite robust and stable.

The effectiveness of the algorithm for the 4-node tetrahedral element is illustrated using the same five test problems as considered in section A.2: a beam in pure bending, a finite plate with a central hole under tensile loading, a square cantilevered plate under shear loading, a curved structure in pure bending, and a tool jig problem (like considered in ref. [14]). We define these test problems in *Fig. A.16*, and show the results (rounded to full digits) in *Fig. A.17* to *Fig. A.22* respectively, where the NPF-based stress refers to the stresses calculated using the proposed nodal point force based stress calculation method.

Mesh 1

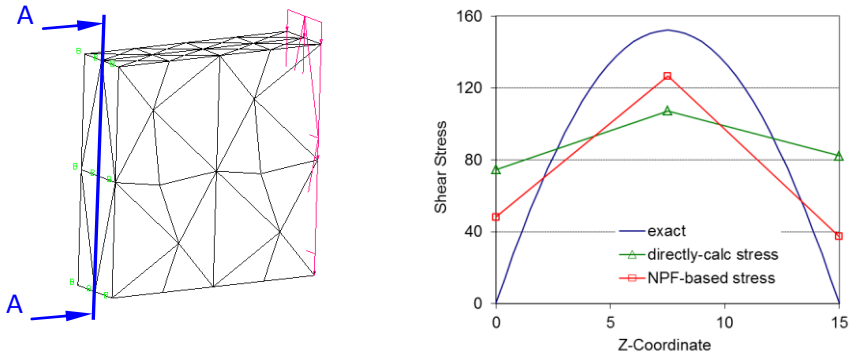

Mesh 2

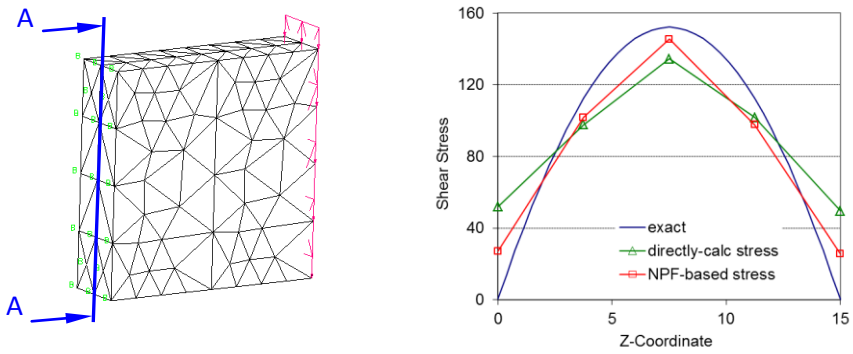

Mesh 3

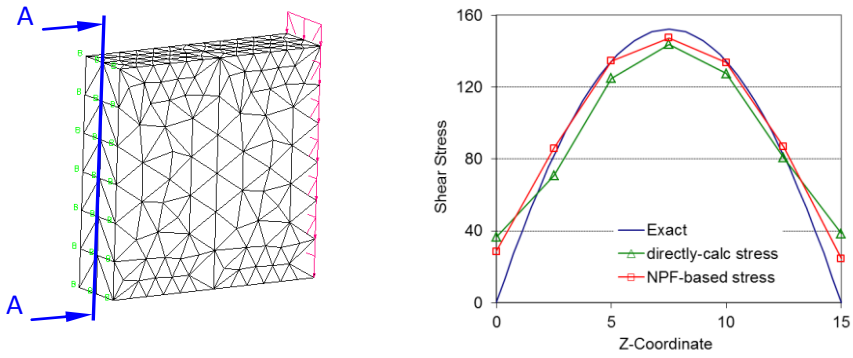

Fig. A.19: *In-plane shear stress results for the square cantilevered plate problem across section A*

Mesh 1

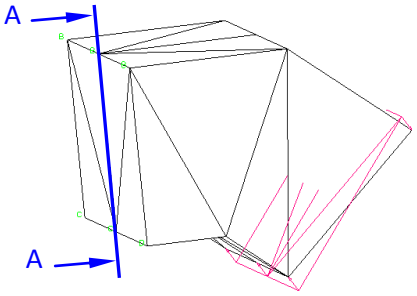

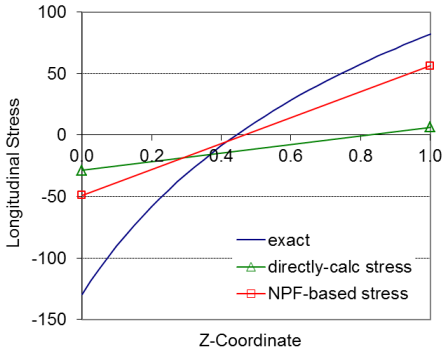

Mesh 2

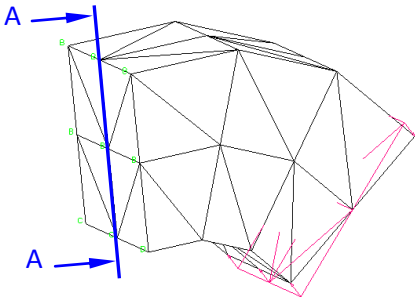

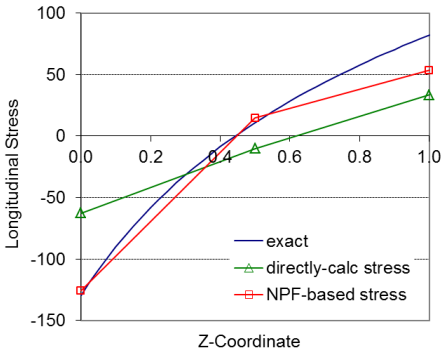

Mesh 3

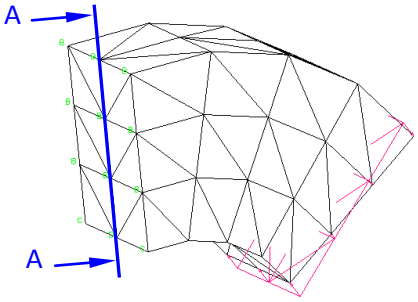

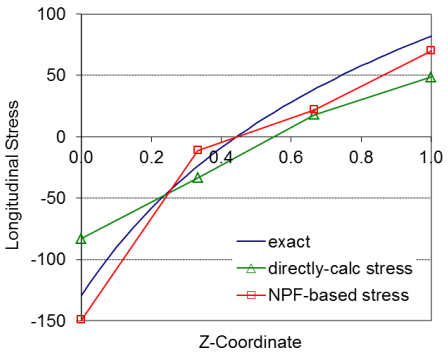

Fig. A.20: *Longitudinal stress results for the curved structure problem across section A*

Considering these results, the values given in the band plots are un-averaged, while the given numerical stress values are the averaged nodal point values with the solution error shown in parentheses. This error is measured with respect to the solution (called "exact" in figures) obtained using a very fine mesh of 27-node hexahedral elements.

Note that a given numerical stress value may be outside the scale of the band plot because we selected the scale to reasonably indicate the stress variation over the complete domain.

As expected, we see a significant improvement in the accuracy of the predicted stresses for all problems solved. However, the improvement in stresses is somewhat less than what we have seen for the 3-node constant strain triangle in section A.2.2, which is partly due to the fact that, for the three-dimensional analyses, we are using linear, and not bilinear, stress interpolations, see Eq. (A.15).

It is interesting to note that, for the problems considered in *Fig. A.18* and *Fig. A.14*, the percentage improvement in stresses increases as the mesh is refined. Naturally, the improvement is most important in the regions of high stress gradients, which, of course, is due to the fact that the stresses $\underline{\tau}_h^{(m)}$ are constant for the 4-node tetrahedral finite element.

In these problems, we have set the Poisson ratio to zero, to ensure consistency with section A.2; however, the same level of improvement is also observed for non-zero values of Poisson ratio, for example, when $\upsilon = 0.3$, as long as the material is not almost or fully incompressible. When the medium is incompressible, as well-known, the four-node displacement-based tetrahedral

element is not effective because it does not satisfy the inf-sup condition [2], [43], [44] and is better not used.

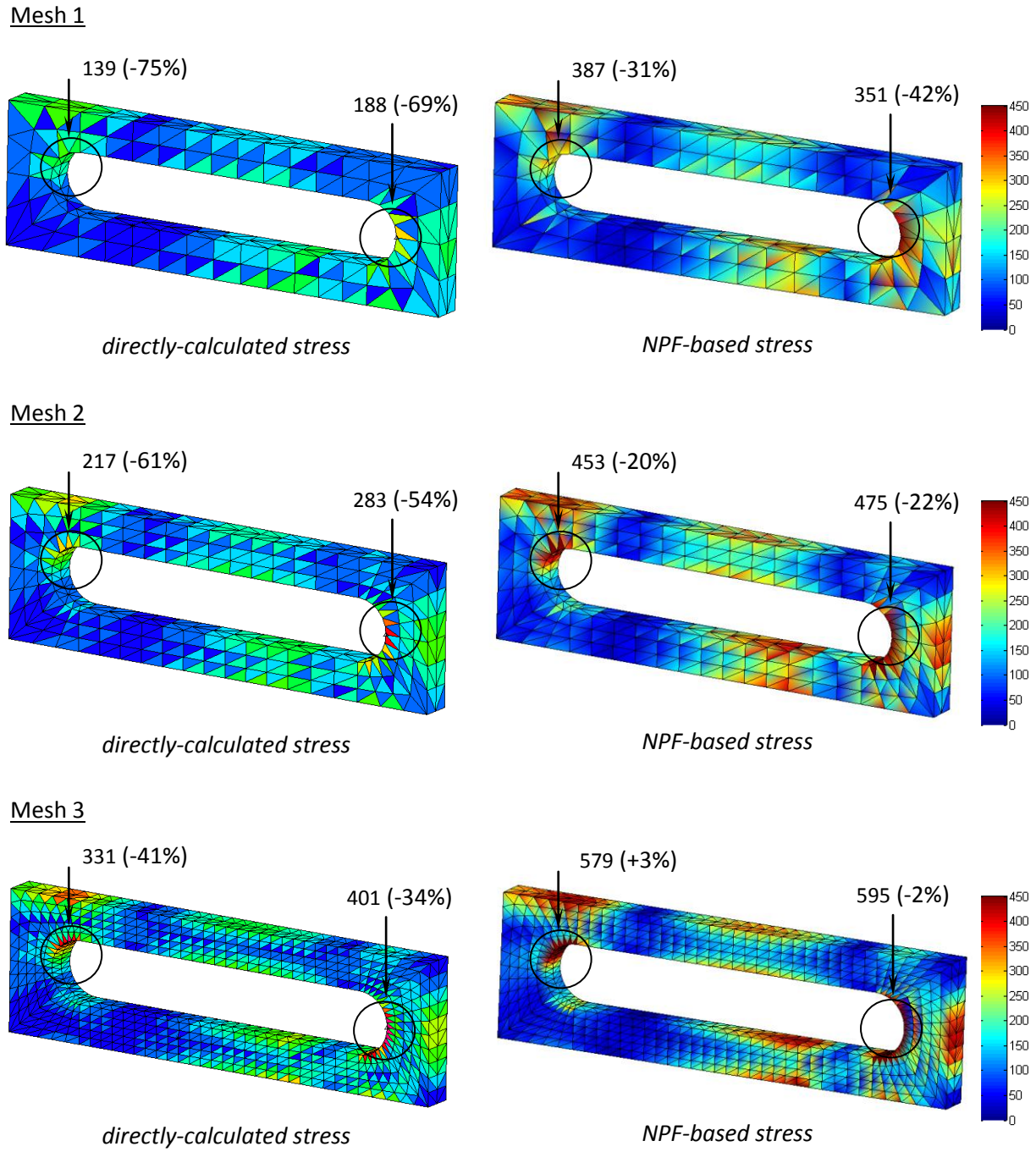

Fig. A.21: *von Mises stress results for the tool jig problem. The solution error is given in the parentheses*

Mesh 1

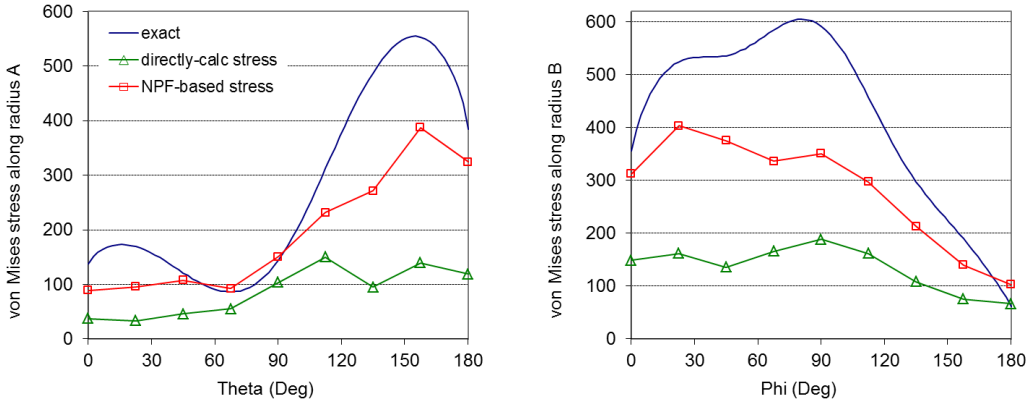

Mesh 2

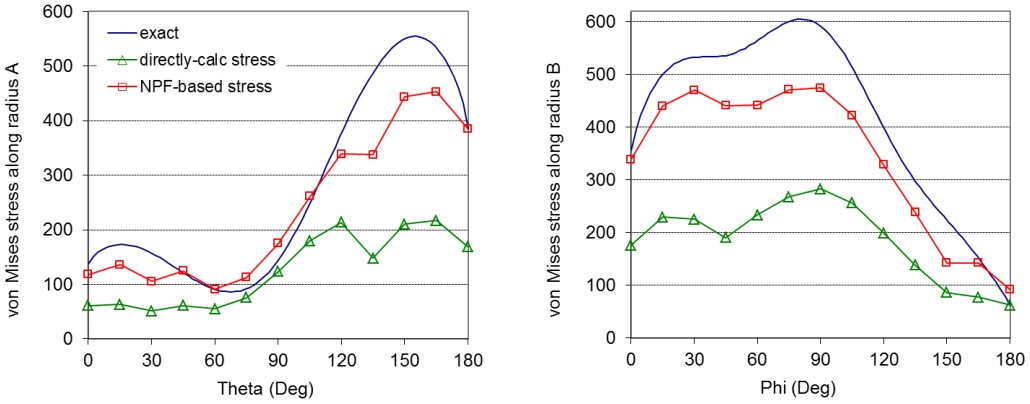

Mesh 3

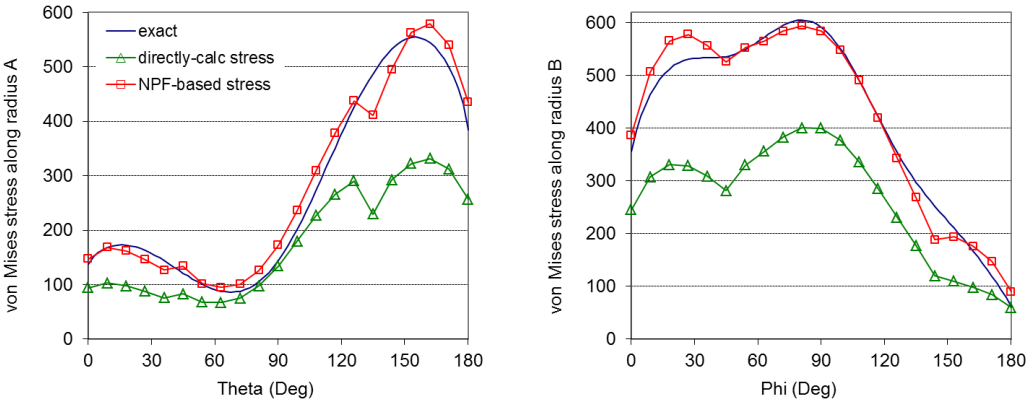

Fig. A.22: *von Mises stress results for the tool jig problem. Radius A and radius B are defined in Fig. A.9, and the mesh densities corresponding to Mesh 1, Mesh 2 and Mesh 3 are shown in Fig. A.14. The figures on the left show the von Mises stress along radius A, whereas the figures on the right show the von Mises stress along radius B*

A.4 Concluding remarks

In this appendix we developed a simple procedure of using the element nodal point forces to obtain finite element stresses that we can expect to be more accurate than the stresses given by the stress assumption implicitly used in the stiffness calculation. We expect more accurate stresses because the assumption for the stresses is of higher order and the nodal point forces are used which always satisfy important equilibrium requirements irrespective of how coarse a mesh is used.

We have applied the procedure to the 3- and 4-node two-dimensional elements, and to the 4-node three-dimensional element, in linear static analysis conditions. As expected, when we applied the procedure, we have indeed seen a significant improvement in the stress predictions for all problems solved.

While the numerical results are encouraging, the method still requires to consider specific element stress domains. Indeed, a drawback of the NPF-based method is that the number of equations available -- and hence the dimension of the interpolation functions assumed in ν^r -- is dependent on the number (and type) of elements in the stress calculation domain. Therefore, to get close to $O\left(h^2\right)$ convergence for the stresses, a large stress domain is needed, and a domain stress averaging procedure has been employed.

After developing the NPF-based method, it was realised a more comprehensive procedure can be devised to improve the stress predictions in static, dynamic and nonlinear solutions. This method is presented in the main body of the thesis.

Bibliography

[1] K. J. Bathe, "*Finite Element Procedures"*, Cambridge, MA: Klaus-Jürgen Bathe, 2006

[2] D. Chapelle and K. J. Bathe, "*The Finite Element Analysis of Shells – Fundamentals"*, Springer, Second Edition, 2010

[3] T. Sussman and K. J. Bathe, "*Studies of finite element procedures -- on mesh selection*", Computers & Structures, 21, 257-264, 1985

[4] T. Sussman and K. J. Bathe, "*Studies of finite element procedures -- stress band plots and the evaluation of finite element meshes*", Engineering Computations, 3, 178-191, 1986

[5] S. H. Lo and C. K. Lee, "*On using different recovery procedures for the construction of smoothed stress in finite element method*", Int. J. Numer. Meth. Engng., 43, 1223-1252, 1998

[6] J. H. Argyris, "*Recent advances in matrix methods of structural analysis*", Progress in Aeronautical Sciences, Vol. 4, Pergamon Press, Oxford, 1964

[7] M. Ainsworth and J. T. Oden, *"A Posteriori Error Estimation in Finite Element Analysis"*, J. Wiley, 2000

[8] T. Grätsch and K. J. Bathe, *"A posteriori error estimation techniques in practical finite element analysis"*, Computers & Structures, 83, 235-265, 2005

[9] T. Grätsch and K. J. Bathe, "*Influence functions and goal-oriented error estimation for finite element analysis of shell structures*", Int. J. Numer. Meth. Engng., 63, 709-736, 2005

[10] N. S. Lee and K. J. Bathe, "*Error indicators and adaptive remeshing in large deformation finite element analysis*", Finite Elements in Analysis and Design, 16, 99-139, 1994

[11] E. Hinton and J. S. Campbell "*Local and global smoothing of discontinuous finite element functions using a least squares method*", Int. J. Numer. Meth. Engng., 8, 461-480, 1974

[12] J. H. Bramble and A. H. Schatz, "*Higher order local accuracy by averaging in the finite element method*", Mathematics of Computation, 31, 94-111, 1977

[13] J. T. Oden and H. J. Brauchli, "*On the calculation of consistent stress distributions in finite element approximations*", Int. J. Numer. Meth. Engng., 3, 317-325, 1971

[14] M. L. Bucalem and K. J. Bathe, "*The Mechanics of Solids and Structures – Hierarchical Modeling and the Finite Element Solution*", Springer, 2011

[15] O. C. Zienkiewicz and J. Z. Zhu, "*The superconvergent patch recovery and a posteriori error estimates Part 1: The recovery technique, Part 2: Error Estimates and Adaptivity*", Int. J. Numer. Meth. Engng., 33, 1331-1382, 1992

[16] J. Barlow, "*Optimal stress locations in finite element models*", Int. J. Numer. Meth. Engng., 10, 243-251, 1976

[17] T. Blacker and T. Belytschko, "*Superconvergent patch recovery with equilibrium and conjoint interpolant enhancements*", Int. J. Numer. Meth. Engng., 36, 2703-2724, 1993

[18] N. E. Wiberg and F. Abdulwahab, "*Patch recovery based on superconvergent derivatives and equilibrium*", Int. J. Numer. Meth. Engng., 36, 2703-2724, 1993

[19] N. E. Wiberg, F. Abdulwahab, and S. Ziukas, "*Enhanced superconvergent patch recovery incorporating equilibrium and boundary conditions*", Int. J. Numer. Meth. Engng., 37, 3417-3440, 1994

[20] O.C. Zienkiewicz and J. Z. Zhu, "*Superconvergence and the superconvergent patch recovery*", Finite Elements Anal. Des., 19, 11-23, 1995

[21] T. Lee, H. C. Park, and S. W. Lee, "*A superconvergent stress recovery technique with equilibrium constraint*", Int. J. Numer. Meth. Engng., 40, 1139-1160, 1997

[22] J. F. Hiller and K. J. Bathe, "*Higher-order-accuracy points in isoparametric finite element analysis and application to error assessment*", Computers & Structures, 79, 1275-1285, 2001

[23] E. Stein and S. Ohnimus, "*Equilibrium method for postprocessing and error estimation in the finite element method*", Computer Assisted Mechanics and Engineering Sciences, 4, 645-666, 1997

[24] E. Stein and R. Ahmad, "*On the stress computation in finite element models based upon displacement approximations*", Comput. Methods Appl. Mech. Engng., 4, 81-96, 1974

[25] E. Stein and R. Ahmad, "*An equilibrium method for stress calculation using finite element displacement models*", Comp. Meth. in Appl. Mech. and Engng., 10, 175-198, 1977

[26] S. Ohnimus, E. Stein, and E. Walhorn, "*Local error estimates of FEM for displacements and stresses in linear elasticity by solving local Neumann problems*", Int. J. Numer. Meth. Engng., 52, 727-746, 2001

[27] B. Boroomand and O. C. Zienkiewicz, "*Recovery by equilibrium in patches (REP)*", Int. J. Numer. Meth. Engng., 40, 137-164, 1997

[28] B. Boroomand and O. C. Zienkiewicz, "*An improved REP recovery and the effectivity robustness test*", Int. J. Numer. Meth. Engng., 40, 3247-3277, 1997

[29] F. Ubertini, *"Patch recovery based on complementary energy"*, Int. J. Numer. Meth. Engng., 59, 1501-1538, 2004

[30] A. Benedetti, S. de Miranda, and F. Ubertini, *"A posteriori error estimation based on the superconvergent recovery by compatibility in patches"*, Int. J. Numer. Meth. Engng., 67, 108-131, 2006

[31] G. Castellazzi, S. de Miranda, F. Ubertini, "*Adaptivity based on the recovery by compatibility in patches*", Finite Elements in Analysis and Design, 46, 379-390, 2010

[32] H. R. Riggs, A. Tessler, and H. Chu, "*C^1-Continuous stress recovery in finite element analysis*", Comput. Methods Appl. Mech. Engrg., 143, 299-316, 1997

[33] A. Tessler, H. R. Riggs, C. E. Freese, and G. M. Cook, "*An improved variational method for finite element stress recovery and a posteriori error estimation*", Comput. Methods Appl. Mech. Engng., 155, 15-30, 1998

[34] M. Vaz, P. A. Munoz-Rojas, and G. Filippini, "*On the accuracy of nodal stress computation in plane elasticity using finite volumes and finite elements*", Computers & Structures, 87, 1044-1057, 2009

[35] D. J. Payen and K. J. Bathe, "*The use of nodal point forces to improve element stresses"*, Computers & Structures, 89, 485-495, 2011

[36] D. J. Payen and K. J. Bathe, "*Improved stresses for the 4-node tetrahedral element"*, Computers & Structures, 89, 1265-1273, 2011

[37] D. J. Payen and K. J. Bathe, "*A stress improvement procedure"*, Computers & Structures, Computers & Structures, submitted

[38] F. Brezzi and M. Fortin, "*Mixed and Hybrid Finite Element Methods*", Springer, 1991

[39] H. Kardestuncer, and D. H. Norrie, "*Finite Element Handbook*", McGraw-Hill, 1987

[40] F. Brezzi and K. J. Bathe, "*A discourse on the stability conditions for mixed finite element formulations*", J. Computer Methods in Applied Mechanics and Engineering, 82, 27-57, 1990

[41] P. Wriggers and S Reese, "*A note on enhanced strain methods for large deformations*", Computer Methods in Applied Mech and Eng, 135, 201-209, 1996

[42] D. Pantuso and K. J. Bathe, "*On the stability of mixed finite elements in large strain analysis of incompressible solids*", Finite Elements in Analysis and Design, 28, 83-104, 1997

[43] K. J. Bathe, "*The inf-sup condition and its evaluation for mixed finite element methods*", Computers & Structures, 79, 243-252, 2001

[44] D. Chapelle and K. J. Bathe, "*On the ellipticity condition for model-parameter dependent mixed formulations*", Computers & Structures, 88, 581-587, 2010

[45] K. J. Bathe and E. N. Dvorkin, "*A formulation of general shell elements – the use of mixed interpolation of tensorial components*", Int. J. for Numerical Methods in Engineering, Vol. 22, 697–722, 1986

[46] K. J. Bathe, A. Iosilevich, and D. Chapelle, "*An evaluation of the MITC shell elements*", Computers & Structures, 75, 1-30, 2000

[47] K. J. Bathe and P. S. Lee, "*Measuring the convergence behavior of shell analysis schemes*", Computers & Structures, 89, 285-301, 2011

[48] A. Mota and J. F. Abel, "*On mixed finite element formulations and stress recovery techniques*", Int. J. Numer. Meth. Engng., 47, 191-204, 2000

[49] A. Benjeddou, *"Advances in piezoelectric finite element modeling of adaptive structural elements: a survey"*, Computers & Structures, 76, 347-363, 2000

[50] K. J. Bathe and M. M. I. Baig, *"On a composite implicit time integration procedure for nonlinear dynamics"*, Computers & Structures, 83, 2513–2534, 2005

[51] K. J. Bathe, *"Conserving energy and momentum in nonlinear dynamics: a simple implicit time integration scheme"*, Computers & Structures, 85, 437-445, 2007

[52] Z. Kazancı and K. J. Bathe, "*Crushing and crashing of tubes with implicit time integration*", Int. J. of Impact Engineering, 42, 80-88, 2012

[53] K. J. Bathe and G. Noh, "*Insight into an implicit time integration scheme for structural dynamics*", Computers & Structures, 98-99, 1-6, 2012

[54] K. J. Bathe, "*Advances in the multiphysics analysis of structures*", Proceedings Eleventh International Conference on Computational Structures Technology, Dubrovnik, Croatia, Sept. 2012